DDC RECEIVED FEB 15 1980 E

LEVEL II

MSC TFR 1105/1008

NADC-77278-30

AD A080893

DDC FILE COPY

DEFINITION AND MODELING OF CRITICAL FLAWS IN GRAPHITE FIBER REINFORCED RESIN MATRIX COMPOSITE MATERIALS

S.N. Chatterjee, Z. Hashin, and R.B. Pipes
Materials Sciences Corporation
Blue Bell Office Campus
Merion-Towle House
Blue Bell, PA 19422

August 1979

Final Report, July 28, 1978 - August 28, 1979

Contract N62269-78-C-0111

Approved for Public Release; Distribution is Unlimited.

Prepared for:
NAVAL AIR DEVELOPMENT CENTER
Warminster, PA 18974

80 2 15 022

NADC-77278-30

DEFINITION AND MODELING OF CRITICAL FLAWS IN GRAPHITE FIBER REINFORCED RESIN MATRIX COMPOSITE MATERIALS

MSC TFR 1105/1008

August, 1979

Prepared for:

Naval Air Development Center
Warminster, PA 18974

Prepared by:

Materials Sciences Corporation
Blue Bell Office Campus
Merion-Towle House
Blue Bell, PA 19422

SECURITY CLASSIFICATION OF THIS PAGE (When Data Entered)

18 17

NADC-77278-30

REPORT DOCUMENTATION PAGE		READ INSTRUCTIONS BEFORE COMPLETING FORM
1. REPORT NUMBER	2. GOVT ACCESSION NO.	3. RECIPIENT'S CATALOG NUMBER
9 Final rept. 28 Jul 78-28 Aug 79		
4. TITLE (and Subtitle) 6 DEFINITION AND MODELING OF CRITICAL FLAWS IN GRAPHITE FIBER REINFORCED RESIN MATRIX COMPOSITE MATERIALS		5. TYPE OF REPORT & PERIOD COVERED Draft Final - July 28, 1978 to Aug. 28, 1979
		6. PERFORMING ORG. REPORT NUMBER 14 MSC/TFR/1105/1008
7. AUTHOR(s) 10 S.N. Chatterjee, Z. Hashin and R. B. Pipes		8. CONTRACT OR GRANT NUMBER(s) 15 N62269-78-C-0111
9. PERFORMING ORGANIZATION NAME AND ADDRESS Materials Sciences Corporation Blue Bell Office Campus Merion-Towle House Blue Bell, PA 19422		10. PROGRAM ELEMENT, PROJECT, TASK AREA & WORK UNIT NUMBERS
11. CONTROLLING OFFICE NAME AND ADDRESS Naval Air Development Center Warminster, PA 19422		12. REPORT DATE 11 28 ~~August 28,~~ 1979
		13. NUMBER OF PAGES 116
14. MONITORING AGENCY NAME & ADDRESS (if different from Controlling Office) 12 120		15. SECURITY CLASS. (of this report) Unclassified
		15a. DECLASSIFICATION/DOWNGRADING SCHEDULE

16. DISTRIBUTION STATEMENT (of this Report)

Approved for Public Release; Distribution is Unlimited

17. DISTRIBUTION STATEMENT (of the abstract entered in Block 20, if different from Report)

18. SUPPLEMENTARY NOTES

19. KEY WORDS (Continue on reverse side if necessary and identify by block number)

Composite Materials, Nondestructive Testing, Graphite Epoxy, Defect Characterization, Fracture Mechanics, Delamination, Buckling, Fatigue, Ultrasonic Wave Propagation, Complex Moduli

20. ABSTRACT (Continue on reverse side if necessary and identify by block number)

An analytical and experimental study was conducted to determine criticality of interlaminar disbonds by NDE methods. Criticality of such flaws in a shear environment (action of shear near support was defined in terms of crack propagation and was analyzed by principles and methods of fracture mechanics. Growth of disbonds under cylic loading was also studied. Failure under compressive loading in presence of a disbond was defined in terms of buckling and an elastic stability analysis was utilized for assessing criticality.

DD FORM 1 JAN 73 1473 EDITION OF 1 NOV 65 IS OBSOLETE

Unclassified

SECURITY CLASSIFICATION OF THIS PAGE (When Data Entered)

390991

lB

20.

Analytical predictions were compared with experimental results in both cases. Ultrasonic "C" scans were used for detection and tracking of the flaws. Preliminary wave propagation studies were conducted for estimating changes in storage and loss moduli induced by moisture conditioning to examine the possibility of using such measurements as NDT techniques for damage assessment.

SUMMARY

An analytical and experimental study was conducted to determine criticality of interlaminar disbonds by NDE methods. Criticality of such flaws in a shear environment (action of shear near support) was defined in terms of crack propagation and was analyzed by principles and methods of fracture mechanics. Growth of disbonds under cyclic loading was also studied. Failure under compressive loading in presence of a disbond was defined in terms of buckling and an elastic stability analysis was utilized for assessing criticality. Analytical predictions were compared with experimental results in both cases. Ultrasonic "C" scans were used for detection and tracking of the flaws. Preliminary wave propagation studies were conducted for estimating changes in storage and loss moduli induced by moisture conditioning to examine the possibility of using such measurements as NDT techniques for damage assessment.

FORWARD

This report summarizes the work done for Naval Air Development Center, Warminster, PA 18974 under contract N62269-78-C-0111 During the period July 28, 1978 to August 28, 1979.

The authors wish to express their sincere appreciation to Dr. B. Walter Rosen and Dr. W. R. Scott for helpful discussions and suggestions during various stages of this program. Thanks are also due to: Mr. Robert Blake for his extensive work in the experimental investigation; Mr. Vince DiMondi and Miss Alitia Makowski for their contribution in the fatigue test program; and Mr. Jerry Rubinsky for help in developing the computer programs for analytical studies.

Approved: B. Walter Rosen

B. Walter Rosen

TABLE OF CONTENTS

LIST OF TABLES

LIST OF FIGURES

LIST OF FIGURES (cont'd)

INTRODUCTION

The NDE analyst faces problems and challenges in evaluating flaws in composite structures because of the complexity of fiber composites. At the present time only limited use is made of NDT techniques in quantitative evaluation of life-limiting composite material flaws. This is due to limitations both the state of the art in assessing flaw criticality in composite structures and of contemporary NDE techniques. However, as the understanding of flaw criticality in composites and new NDE techniques are evolved, more reliable serviceability criteria may be adopted. This will enable definition of regular inspection intervals for a structural element during its service to determine the criticality of existing flaws.

Development of the required nondestructive evaluation methodology includes consideration of the following successive phases of interest:

1. Definition of measurable quantities. This defines what can be measured at the lamina and/or laminate level through available techniques.
2. Definition and demonstration of the correspondence between the NDE measured quantities and the associated defects. In general, the defects may be birth defects or service defects, and the effect of each type on the measurable quantities should be determined, both analytically and experimentally.
3. Evaluation of the criticality of the defects. This requires: evaluation of the appropriate residual property (stiffness, strength, etc.) in the presence of known defects; an experiment-analysis correlation study for the same; and formulation of a quantitative relationship between the NDE measurements and these residual properties.

In the present program, development of this evaluation methodology was undertaken for defects in the form of interlaminar disbonds. This defect was selected after consideration of a range of possible defects. Various kinds of defects can cause relevant

strength and stiffness degradation in composite laminates; namely: interlaminar disbonds; cracks or other through-the-thickness defects; defects in bolted and bonded joints; damage resulting from impact; and fatigue damage. Different NDI techniques (active and passive) which are usually used, or being developed for studying effects of such defects, are listed below:

1. Ultrasonics (modulus degradation measurement and damage detection).
2. Acoustic emission (sequential recording of the damage growth process).
3. X-ray and thermography (visual and real-time detection of defect growth).
4. Structural vibrations (stiffness degradation measurement).
5. Penetrants.
6. Holography.

For the present work, the decision was made to use ultrasonic "C" scans for detecting and following the growth of interlaminar disbond. This defect is a realistic one which is well-defined and can have an important effect upon structural performance. The NDE technique is widely used and provides a reliable measure of the size of the interlaminar disbond.

Analytical studies were conducted to model the physically realistic interlaminar damage modes and to assess the resulting property degradation and criticality of disbonds in both shear and compression environments. Mechanical tests were conducted to relate the observed states of magnitude and geometry of damage to the residual performance capability.

In addition, preliminary wave propagation studies were performed for quantifying changes in storage and loss moduli induced by fatigue damage and/or moisture conditioning and to examine the usefulness of such measurements as NDT techniques for assessing quantitatively the magnitude of such damage.

Correlations of data from NDI, mechanical tests, and analyses were carried out to demonstrate the feasibility of using this approach for the development of quantitative NDE of flaw severity in composites.

SCOPE

Initiation and growth of flaws in a composite structural member depend on imposed loads and various material and geometric parameters. Applied loads can be classified in various categories, namely:

1. Inplane loads (tensile, compressive, shear or multiaxial);
2. Transverse loads (and shear);
3. Stresses induced by environmental factors like temperature and moisture.

Some of the important material and geometric parameters are:

1. Anisotropic material properties and orientation of individual laminae;
2. Laminate layup;
3. Geometry of the laminated components; and
4. Location, shape and size of the flaw.

Also, different types of flaws may result in a large number of potential failure modes. Therefore, the factors which influence the phenomena of flaw growth identify a problem of enormous complexity. The objective of the present program was to choose some representative flaws which are of crucial importance in composite structural members and to develop a methodology for quantifying damage tolerance characteristics of such flawed members subjected to the type of loads which are likely to cause damage growth and final failure. Damage tolerance can be quantified in terms of residual stiffness, strength or lifetime.

The procedure employed was to combine analytical methods for assessing criticality of flaws and residual properties with an experimental program which supplemented the analytical investigation. The other alternative was an extensive experimental investigation which could become cost prohibitive even for a single type of flaw. It was also noted that it would be impossible to use a single analytical model to encompass the whole spectrum of fatigue, fracture, or other kinds of failure for various types of flaws. A logical first step was to begin with a simple but commonly encountered

flaw geometry like an interlaminar disbond in a laminated beam and to carry out analytical and experimental correlation studies, so that confidence could be developed for similar studies on other types of flaws. Interlaminar disbonds are quite common in laminated members because they can exist as "birth" defects and can be created during service by foreign object damage or various other reasons. Laminated members are used for carrying inplane loads as well as transverse shear stresses. Presence of a disbond does not affect the primary function of a member under inplane loads except when such loads are compressive in nature which might result in local buckling type failure of a part of the laminate adjacent to the disbond. Under transverse shear catastrophic and slow growth of disbonds may occur due to static and cycling loading, respectively. Therefore, in this study attention was restricted to growth of disbonds and failure under compression and shear environments.

Development of new NDT techniques and modification or improvement of existing ones are necessary for successful application of NDE methodologies to composite structures. Measurements of storage and loss moduli (dynamic) and their use in quantifying damages accumulated due to fatigue and other environmental factors appear to have a good potential in that direction. For this reason some exploratory studies were directed in understanding the phenomenon of ultrasonic wave propagation in neat resin and laminates. Experimental investigations were aimed at developing methods of measurement and analysis of data to obtain physically meaningful quantities. Since matrix material properties are usually susceptible to accumulated damages, analytical studies were aimed at developing methods for assessing damages from measured composite response.

NDE METHODOLOGY TO ASSESS FLAW CRITICALITY

Nondestructive inspection focuses upon detection of flaws and quantifying them in terms of their size and magnitude, while nondestructive evaluation techniques are needed to assess their criticality. Allowable limits of flaw size or magnitude must be determined to establish inspection intervals for in-service flawed structural components and criteria for judging the necessity of mandatory repair.

For the interlaminar disbonds nondestructive evaluation is based on a static/fatigue failure analysis. Criticality of disbonds under static transverse shear is defined in terms of crack propagation and is analyzed by principles and methods of fracture mechanics. For cyclic transverse shear, use of a well known empirical methodology is suggested for quantifying damage growth. Failure of a disbonded laminate under compressive loading is defined in terms of buckling and an elastic stability analysis is utilized for assessing criticality. Residual strength or lifetime can therefore be predicted by combining results obtained by the use of techniques described herein.

Analytical methods for assessing the relationships connecting speed and attenuation of ultrasonic waves traveling through the thickness of a laminate with the properties of its viscoelastic constituents is presented. These relationships will be useful in assessing the magnitudes of residual moduli of the matrix material from nondestructive wave propagation studies and hence effects of accumulated damages, if any. Experimental NDT methods and descriptions of mechanical tests conducted for verifying the adequacy and accuracy of analytical evaluation methods and other tools are described. Results of correlation studies are presented and discussed which demonstrate the usefulness of the NDE methodology.

ANALYTICAL METHODS

PROPAGATION OF DISBOND IN STATIC SHEAR

Individual layers in laminated composites commonly used in practice are unidirectionally reinforced materials containing fibers arranged in a random array. For the purpose of useful stress analysis such unidirectional composites can be considered as anisotropic materials which behave elastically until failure. Principles and mathematical methods employed in linear elastic fracture mechanics are utilized here for analysis of stresses near a delamination in an arbitrarily laminated structure under a state of plane deformations. In practice delamination or disbond type defects in aircraft components are usually birth defects with two-dimensional planar form. Such defects may also originate from foreign object damage or various other reasons. Three-dimensional elasticity solutions employing complex mathematical tools or finite element methods must be obtained for analyzing stress states near such defects. However, 2-D defects cannot propagate in a self similar fashion and methods for studying their growth are yet to be developed, even for isotropic materials. For design purposes criteria for one-dimensional flaw growth are usually employed under such circumstances which usually yield conservative estimates of critical loads. For a laminated composite the state of the art is less advanced because very few attempts have been made to perform rigorous stress analysis even under the framework of two-dimensional anisotropic elasticity. An approximate strength of materials approach has been used in a previous study (ref. 1). Although finite element methods have been employed for studying stress states near defects in laminated structures (refs. 2,3), it is known that such numerical solutions are sensitive to various parameters employed in the solution (see ref. 4).

In this study an exact solution of the two-dimensional elasticity problem of a simply supported laminated beam or plate (fig. 1) with defects is obtained. Solutions to the governing differential equations for each layer are chosen in the form of infinite

series, as outlined in Appendix A-1. Two unknown functions are introduced which characterize the displacement discontinuities at the delaminations. By employing a suitable stiffness formulation, displacements and stresses corresponding to each term of the series (harmonic m) are expressed in terms of applied load and the unknown functions. By the use of an asymptotic solution as $m \to \infty$ and other algebraic manipulation the problem is reduced to the solution of a coupled pair of singular integral equations. The stress singularities at the tips of a delamination are characterized. Numerical solutions are obtained for thick laminated beams used in the test program. The parts of the beam which contain the delaminations are under a state of transverse shear. Such a shear environment alone is crucial for aircraft components since membrane states of stress are not affected by the presence of delaminations.

Strain energy release rates for growth of interlaminar defects in beam, plate or shell type structures have been obtained in various studies (refs. 5-8) by the use of beam, plate or shell theories. Employing similar techniques the delaminated beam was considered in reference 1. Results of the present solution are compared later with analytical solutions and experimental results reported in reference 1 and with test data obtained in this program.

As indicated in Appendix A-1, the coupled pair of integral equations are solved by a collocation method to determine the unknown functions ϕ_1 and ϕ_2 at a discrete number of points over the interval $[-1,1]$ and stress intensity factors at x=c and d corresponding to mode I and mode II are evaluated as:

$$\begin{aligned}
K_{Id} &= -H_{11}^{0}\sqrt{d-c}\;\phi_1(1)/4\sqrt{2} \\
K_{Ic} &= H_{11}^{0}\sqrt{d-c}\;\phi_1(-1)/4\sqrt{2} \\
K_{IId} &= H_{22}^{0}\sqrt{d-c}\;\phi_2(1)/4\sqrt{2} \\
K_{IIc} &= -H_{22}^{0}\sqrt{d-c}\;\phi_2(-1)/4\sqrt{2}
\end{aligned} \tag{1}$$

where H^0_{ii} depend on the properties of the layers adjacent to the disbond. In the test program the disbonds are located between two similar layers and in such cases $H^0_{12}=0$ and the stress singularities at the tips of the disbond are of inverse square root type. Equation (1) given above has been derived based on this assumption. When the disbond is located between two dissimilar layers the singularity is no longer of inverse square root type, but modified expressions characterizing the stress distribution near the tips of a delamination can be derived without much complication based on the methodology described in Appendix A-1. However, a different numerical procedure must be utilized under such circumstances for solving the integral equation. For inverse square root type singularity the strain energy release rate is given by:

$$G = \frac{\pi}{2}\left[\frac{K_I^2}{H^0_{11}} + \frac{K_{II}^2}{H^0_{22}}\right] \tag{2}$$

Catastrophic propagation of the disbond will occur when G reaches the critical value G_c, which can be considered as a material constant. The results of the experimental program are utilized to evaluate G_c. In a shear environment K_I is extremely small compared to K_{II} and catastrophic failure may also be characterized by a fracture toughness.

GROWTH OF DISBOND IN CYCLIC SHEAR ENVIRONMENT

Fatigue crack propagation is a complex phenomenon which depends on the nature of applied loads, fatigue and mechanical properties of the material, microstructural process zones in the immediate vicinity of the crack tip and various other factors. Other phenomena which may have significant influence on growth of a flaw are crack blunting, crack closure, residual stresses, etc. A realistic analytical model for crack propagation has yet to be developed. Some studies in this direction (refs. 9-12) have been attempted for ductile metals with limited success. Since microstructural processes near a disbond in composites are not yet as

clear as those in metals and not much is known about fatigue properties of complex, anisotropic composite laminae and laminates, a practical approach to study propagation of disbonds in laminated composites appears to be the use of the well known semi-empirical crack growth law, i.e.:

$$\frac{da}{dN} = C(\Delta K)^n \qquad (3)$$

where

a = disbond or crack length

N = number of cycles

ΔK = the stress intensity factor range = $\eta \sqrt{a}\,(S_{max}-S_{min})$

S_{max}, S_{min} = the maximum and minimum value of applied load or stress

η = a factor depending on geometry and other variables influencing stress intensity factor

C, n = empirical constant and exponent obtained from curve fit to experimental data.

In this study, K_{II}, the mode II stress intensity factor is utilized as K and α is calculated based procedures outlined in the preceding subsection and Appendix A-1, which yield stress intensity factors based on the exact solution of the two-dimensional anisotropic elasticity problem of the laminated beam considering the stacking sequence of the laminate.

BUCKLING FAILURE OF COMPRESSION SKIN CONTAINING A DELAMINATION

When a laminate containing a disbond is subjected to compressive loading, buckling type failure may result in a significant reduction in strength. Such failures are likely to be most critical in the compression skin of a sandwich beam or plate. In this study attention is restricted to the one-dimensional beam type structure containing a single disbond. For the purpose of analysis the compression skin is considered to be supported on an elastic foundation providing constraints in shear as well as extensional

loadings. The skin is modeled as an assemblage of four beam elements (see fig. 2), namely:

1. Two beams (1,2) of finite length equal to the length of the disbond, one above and the other below it; and
2. Two semi-infinite beams (3,4) connected to the finite beams at the tips of the disbond.

Differential equations governing the deformations of the compressed laminated beam elements resting on elastic foundation include the effects of shear deformation. These equations are solved and stiffness matrices for the elements are derived for symmetric deformation patterns, since the lowest value of critical load is desired. Determinants of the global stiffness matrix are calculated for a set of prescribed compressive loads and the critical load is determined from the condition that the determinant is equal to zero. A trial and error procedure is utilized to determine the eigenvalue up to the desired accuracy. Details of the formulation are given in Appendix A-2. Sandwich beam specimens (fig. 3) with varying disbond lengths were designed to test the validity of the flaw criticality criterion determined from analysis. Details of the test specimens can be found in the following section. Maximum disbond length was ℓ=38.1 mm in a beam of span L=508 mm. Therefore, the assumption that beams 3 and 4 are semi-infinite in length appears to be reasonable. The thickness of the 12 ply compression skin $(0/\pm 45/\mp 45/0)_s$ with the disbonds located in the mid-plane was small (of the order of 1.5 mm) as compared to the depth of the aluminum honeycomb core (H_C=38.1 mm). Therefore, the skin can be considered to be under a state of uniform compressive strain. Compressive forces on the four beam elements, however, differ in magnitude. Axial and bending stiffnesses of the beam elements are computed using laminate analysis. Shear stiffnesses are calculated on the assumption of constant shear stress in the layers, i.e., $1/C^*_{55}=\sum_i V^i/C^i_{55}$, V^i being the volume fraction of layer i. In addition, a shear correction factor k_{55} equal to 5/6 is used to obtain the effective shear stiffness. For the purpose of computation of foundation modulus the core is assumed to be fixed at the tension flange.

TRANSVERSE WAVE PROPAGATION AND COMPLEX MODULI

An important nondestructive evaluation test consists of sending a pulse transversely through the laminate. Comparison of transmission/reflection data for unflawed and flawed laminates may then serve to uncover characteristic flaws in this manner. The following discussion will be concerned with simple transverse wave propagation through a laminate and of the complex moduli associated with matrix damping and the waves considered. Propagation of elastic waves in a laminate is duscussed in Appendix A-3.

A polymer fiber composite will exhibit viscoelastic effects if the polymeric matrix viscoelasticity is significant. If sinusoidal waves are transmitted transversely to the laminate then it follows from (A-3.10) and standard viscoelastic wave theory (see ref. 13) that the wave speed is:

$$c' = \mathrm{Re}\left\{\sqrt{\frac{\tilde{k} + \tilde{G}_T}{\rho}}\right\} \qquad (4$$

and the amplitude attenuation is:

$$\alpha = \frac{1}{c'^2}\,\mathrm{Im}\sqrt{\frac{\tilde{k}+\tilde{G}_T}{\rho}} \qquad (5)$$

where $\tilde{k}$ and $\tilde{G}_T$ are the complex counterparts of the elastic constants k and G_T.

$$\tilde{k}\ (i\omega) = k'(\omega) + ik''\ (\omega) \qquad (6)$$

$$\tilde{G}\ (i\omega) = G'(\omega) + iG''\ (\omega)$$

Here ω is the frequency, prime and double prime denote real and imaginary part, respectively, and $i = \sqrt{-1}$.

The experimental determination of the complex moduli $\tilde{k}$ and $\tilde{G}_T$ entering into (4,5) is a matter of considerable difficulty. Fortunately, however, these complex moduli can be computed on the basis of matrix viscoelastic and fiber elastic properties by methods given in reference 14. Accordingly the complex effective moduli $\tilde{k}$ and $\tilde{G}_T$ are given by the expressions:

$$\tilde{k} = \frac{\tilde{k}_m(k_f+\tilde{G}_m)v_m + k_f(\tilde{k}_m+\tilde{G}_m)v_f}{(k_f+\tilde{G}_m)v_m + (\tilde{k}_m+\tilde{G}_m)v_f} \tag{7}$$

$$\tilde{G}_T = \tilde{G}_m + \frac{v_f}{\dfrac{1}{G_{Tf}-\tilde{G}_m} + \dfrac{\tilde{k}_m + 2\tilde{G}_m}{2\tilde{G}_m(\tilde{k}_m+\tilde{G}_m)}\, v_m} \tag{8}$$

Here:

- m - Index indicating matrix
- f - Index indicating fiber
- v - Volume fraction.

The isotropic matrix complex plane strain bulk modulus can be written:

$$\tilde{k}_m = K_m + \frac{1}{3}\tilde{G}_m \qquad \text{(a)}$$

$$k_m' = K_m + \frac{1}{3}G_m' \qquad \text{(b)} \tag{9}$$

$$k_m'' = \frac{1}{3}G_m'' \qquad \text{(c)}$$

where K_m is the three-dimensional elastic bulk modulus and the usual assumption has been made that matrix dilatational viscoelasticity can be neglected.

The matrix complex shear modulus is written in the form (6):

$$\tilde{G}_m(i\omega) = G_m'(\omega) + iG_m''(\omega) \qquad \text{(a)}$$
$$(10)$$
$$\tan \delta_m = G''/G' \qquad \text{(b)}$$

where the last expression is the loss tangent.

It is now necessary to find the real and imaginary parts of (8). This tedious undertaking is greatly facilitated by exploitation of the fact that (10) is generally a small number (of order .05). It can be shown (ref. 15) that in that case:

$$k' = \tilde{k}(k_m', G_m')$$
$$(11)$$
$$k'' = k_m'' \frac{\partial k'}{\partial G_m'}$$

$$G' = \tilde{G}(k_m', G_m')$$
$$(12)$$
$$G'' = G_m'' \frac{\partial G'}{\partial G_m'}$$

It follows that:

$$k'(\omega) = \frac{k_m'(k_f+G_m')v_m + k_f(k_m'+G_m')v_f}{(k_f+G_m')v_m + (k_m'+G_m')v_f} \qquad \text{(a)}$$

$$G_T'(\omega) = G_m' + \cfrac{v_f}{\cfrac{1}{G_{Tf}'-G_m'} + \cfrac{k_m' + 2G_m'}{2G_m'(k_m'+G_m')} \, v_m} \qquad \text{(b)} \quad (13)$$

$$k''(\omega) = \tfrac{1}{3}G_m'' \left\{ 1 - \frac{(k_m'+G_m')^2 - 4v_m(k_f-k_m')^2}{[k_m'+G_m' + v_m(k_f-k_m')]^2} \, v_f \right\} \qquad \text{(a)}$$

$$(14)$$

$$G_T''(\omega) = G_m'' \left\{ 1 - \frac{\left(\dfrac{G_m'}{G_{Tf}'-G_m'}\right)^2 - \tfrac{1}{2}\left[1 + \left(\dfrac{G_m'}{k_m'+G_m'}\right)^2\right] v_m}{\left\{\dfrac{G_m'}{G_{Tf}'-G_m'} + \tfrac{1}{2}\left(1 + \dfrac{G_m'}{k_m'+G_m'}\right) v_m\right\}^2} \, v_f \right\} \qquad \text{(b)}$$

Then the wave speed (4) is given to excellent approximation by:

$$c'(\omega) \cong \sqrt{\frac{k'(\omega) + G_T'(\omega)}{\rho}} \qquad (15)$$

and the attenuation (5) by:

$$\alpha = \frac{2\sqrt{\rho}\, G_T''(\omega)}{3[k'(\omega) + G_T'(\omega)]^{3/2}} \qquad (16)$$

This implies that a longitudinal wave propagating transversely through the laminate has velocity given by (15) and its amplitude after propagating distance d is attenuated by the amount $\exp(-\omega\alpha d)$.

The wave speed (15) and the attenuation (16) can be determined experimentally by propagating a longitudinal wave normal to the laminate. Examination of (13), (14) which enter into (15), (16) shows that the real and imaginary parts G_m' and G_m'' of the matrix shear modulus can be determined from (15), (16) if all other quantities entering are known. These are fiber elastic properties G_{Tf} and k_f, fiber and matrix volume fractions v_f and v_m and the real part k_m'. Recalling (9b), it is seen that for the last quantity it is merely necessary to know the frequency independent three-dimensional matrix bulk modulus K_m. It is thus seen that normal wave propagation can serve to determine in situ values of G_m' and G_m''.

EXPERIMENTAL PROGRAM

SHEAR TESTS ON THICK DISBONDED LAMINATES

The thick beam laminates were tested in three point bending with a fixture specially manufactured for these tests. The specimen dimensions were 254 mm x 25.4 mm x 8.9 mm (10 in. x 1 in. x .35 in.). The support span was 152.4 mm (6 in.). The center support consisted of two 11.13 mm (0.438 in.) diameter cylinders which were clamped to each side of the specimen. This support was attached to wedge action friction grips which were connected to the load cell. The end supports were also 11.13 mm (0.438 in.) cylinders which only contacted one side of the specimen (fig. 4).

The static tests were performed on an Instron (Model TTC) static testing machine. The specimens were loaded at a cross head rate of .05 cm/min. The failure load was recorded from the chart recorder as the maximum load experienced prior to failure. The fatigue tests were performed in an Instron Servo-hydraulic fatigue testing machine. The load was varied in a sinusoid at a frequency of 10 HZ with the minimum load equal to ten percent of the maximum load. Several maximum load levels were tested.

Two different graphite-epoxy laminates were tested. The $[(0/90)_6 0_{12}]_s$ laminate had two types of implanted defects (fig. 5). The 25.4 mm (1.0 in.) square defect was oriented such that the delamination was perpendicular to the longitudinal axis of the specimen. The 25.4 mm (1.0 in.) diamond defect was oriented at 45° to the specimen axis so that the delamination came to a point. Each specimen contained two implanted defects located midway between the center and end supports. These specimens were precracked by clamping the specimens through the thickness to arrest crack growth and then loaded until cracking was detected by acoustic emissions. The specimens were then ultrasonically C-scanned to determine the precrack length. These lengths are given in Table 1. The specimens were then statically tested

without clamps. The failure loads for these tests are also given in Table 1.

The $[(0_4/\pm45_2/\pm45_2/0_4)_s]_s$ laminate was implanted with diamond defects only. The defect lengths were 19.05 mm (0.75 in.), 25.4 mm (1.0 in.), and 31.75 mm (1.25 in.). These samples were tested statically with no precracking. The static test results are given in Table 2. The fatigue tests were conducted at several different S-levels. Samples with 0.75 in. and 1.0 in. defects were fatigued at S-levels of 0.4, 0.5 and 0.6. The samples with 1.25 in. defects were fatigued at S-levels of 0.3, 0.4, 0.5 and 0.75. The number of cycles to failure are given in Table 3. Typical flaw propagation results are presented in fig. 6-17.

COMPRESSIVE BUCKLING OF DISBONDED LAMINATES

The compressive buckling properties of an AS-3501-6 graphite-epoxy laminate were determined by four point bending of a sandwich beam specimen. The specimens were constructed from 24 lb. Hexel aluminum honeycomb adhesively bonded to two 12 ply graphite-epoxy faces. The honeycomb thickness was 38.1 mm (1.5 in.) and the sample width was 25.4 mm (1 in.). The overall specimen length was 559 mm (22 in.). Figure 18 gives the specimen and loading geometry.

The laminate which was tested was the $[0/\pm45_2/0]_s$. Two layers of 1 mil teflon were embedded in the laminate to simulate a delamination. The near surface defect was implanted between the third and fourth plies while the center disbond was implanted between the two middle plies. The length of these rectangular disbonds was varied from 12.7 mm (0.5 in.) to 38.1 mm (1.5 in.). Specimens with no implanted defects were also tested.

For each tests the longitudinal strain on the compressive face (ε_C) was plotted versus the strain on the tensile face (ε_T) on an X-Y recorder. Since the strain gages were located directly over the implanted defect, it can be seen that when the specimen buckled at the defect, the compressive strain was reduced. As

the load is increased, the buckled region "bows out" and the compressive strain is reduced accordingly. For the samples with 19.05 mm (0.75 in.) debonds and the samples with no defects, the compressive strain was also plotted against the load which was applied to the beam. The shape of these curves is identical to the strain versus strain curves. The buckling load was taken to be the load at which the maximum compressive strain was attained. This load was taken from the Instron chart for the samples where load versus compressive strain was not plotted. The stress at buckling was calculated from beam theory to be:

$$\sigma = \frac{4P}{(1.5+t)(tw)} \qquad (17)$$

where P is the applied load at buckling, t is the laminate thickness (1.524 mm = .06 in.), and w is the specimen width (25.4 mm = 1.0 in.). The experimental results are summarized in Table 4.

The results for the specimens with no defects show that both the ε_C versus ε_T and ε_C versus load curves are linear to failure (fig. 19).

The behavior of the samples with defects in the center of the laminate was highly dependent upon the length of the implanted defect. For the smaller size defects (0.5 in. and some of the 0.75 in. samples), the curves were linear to failure (fig. 20,21). The failure stress of these samples was considerably less than that for the samples with no defects. This means that the presence of the smaller defects does affect strength but this behavior can not be detected from the recorded strains. For the samples with larger defects (some of the 0.75 in. and all 1.0 in. samples), the ε_C versus ε_T and ε_C versus load curves were linear until the samples began to buckle at the debond (figs. 22,23). When this occurred, the compressive strain was reduced as the area over the debond "bows out." For the samples with the 1.5 in. defects in the center of the laminate, the behavior was the same as the 1.0 in. defects except for an initial non-linearity (fig. 24). This is due to the fact that for these samples, the tension side of the beam was prebuckled due to residual thermal stresses in the 1.5 in. near surface defects. Thus there is an initial reduction in tensile strain until this prebuckle "flattens out."

The samples with the near surface defects were prebuckled due to thermal residual stresses from the curing or bonding operations. As a result, the application of a compressive load to these samples causes the buckle to "bow out" immediately. Thus the compressive strain becomes negative (or becomes a tensile strain). The 1.0 in. near surface defect samples showed a small increase in compressive strain before buckling occurred (fig. 25). The stress at buckling was very small. The 1.5 in. defect samples were buckled prior to testing and as a result the comprssive strain decreased linearly with the tensile strain of the tensile side of the beam (fig. 26). Therefore, no buckling stress was measured for these samples.

In summary, it can be seen for the center defects, the compressive stress at failure decreases with defect length (fig. 27). The stress-strain response for smaller defects is linear until failure. For the larger defects, the material over the defect buckles, causing a reduction in compressive strain. The prebuckling phenomenon of the near surface defect samples caused the samples to buckle immediately after the application of load. For all samples with implanted defects, failure was due to buckling of the material above the defect which resulted in a delamination extending from the implanted defects (figs. 28, 29, 30).

MECHANICAL CHARACTERIZATION FOR MOISTURE CONDITIONING EFFECTS

In an effort to develop environmental degradation in composite laminates for subsequent nondestructive evaluation, test sample laminates of $[\pm 45]_{2s}$ configuration were exposed to 100 percent relative humidity conditions (vapors of boiling water) for a period of four months. The samples were removed and tested in a dry condition in order to establish mechanical property degradation. Table 5 lists the results of these tests.

Samples of the neat resin, 3501-6 were also subjected to the environmental exposure discussed above. No mechanical characterization of the neat resin was undertaken.

ULTRASONIC WAVE PROPAGATION STUDIES

Variable Incidence Ultrasonic Test Facility

To evaluate the ultrasonic material elastic constraints other than C_{33}, it is necessary to measure both the longitudinal and shear velocities of sound in the material. Shear waves are produced in a sample when it is inclined at an angle not normal to the incoming sound. The mode conversion resulting from non-normal incidence produces waves with both shear and longitudinal polarization as shown in fig. 31. Due to the translation of the shear and longitudinal velocity components, it is necessary to be capable of translating either the transmitting or receiving transducer 90° to the transmitted sound as well as being capable of rotating both the specimen and the receiving transducer.

In order to perform through transmission ultrasonic measurements in both the normal incidence and non-normal incidence mode, a test tank was constructed. The tank consists of two concentric turntables with a motor drive and position encoder for each. The center turntable has a vise for holding the sample and the outer turntable has a mount for the receiving transducer. The transmitting transducer is mounted on the tank base. The tank is constructed of anodized aluminum and plexiglas. The motor drive units are made of steel and are attached to the turntables via a worm drive system. The encoders are attached to the turntables through a cable mechanism which drives a screw attached to two 15 turn precission potentiometers. The turntable position is given by a voltage output which ranges from 0.00 to 3.60 volts.

The transmitting and receiving transducers are connected to a panametrics ultrasonic analyzer and the output is monitored with a Nicolet digital oscilloscope set for a sampling rate of 20 MHz. The 20 MHz sampling rate implies that only signals up to 10 MHz may be observed without aliasing, therefore, in order to satisfy the Nyguist criteria, a low pass filter with a 10 MHz cut-off frequency is inserted between the output of the ultrasonic analyzer and the oscilloscope input. The oscilloscope is

capable of outputting information in digital form; however, before this information could be analyzed, an interface had to be built to connect the digital oscilloscope to an LSI 11 Digital computer. The interface uses standard TTL components to form a multiplexed seven channel input output port. Each channel has sixteen input and sixteen output bits. The output channels have both latching and tristate capability. The data from the oscilloscope is transmitted through the LSI 11 computer to a Burrows B7700 computer over a telephone line for analysis and storage. After the data is stored, it can be analyzed using FFT techniques and a frequency spectrum of the ultrasonic waveform can be produced. In addition to analyzing the total waveform, any part of the data may be analyzed at any time without the need of performing the test again.

Software Development

LSI 11 machine language programs had to be developed in order to control the interface between the digital oscillascope and the computer. This software has the capability of initializing the interface and transmitting any portion of the ultrasonic waveform through a modem connected to a telephone line. The program fills a file with data after the file is initially created by the operator. The operator can communicate with the computer through a Digital LA36 line printing terminal or through a Tektronix 4006-1 graphics terminal. The graphics terminal is used to plot results of the FFT routines. This data transmission program is called NICDATA.

In order to determine the frequency spectrum of the waveform, a program called NICTRUM was written in fortran which runs on the Burrows B7700 computer. The program takes the FFT of the entire data string and displays both the ultrasonic waveform and the spectrum on either a Tektronix terminal or flatbed plotter.

In order to analyze selected portions of the total waveform, a program called PARTITION was written. This program allows the data string to be plotted and then portions of the waveform can be partitioned for analysis separate from the total waveform.

A program which takes the FFT of the first partition was written and is called SELECTRUM (fig. 32). Another program was written to compare spectrums of different parts of the waveform. COMPARETRUM (fig. 33) takes the FFT of the first, second and third partitions as well as the total waveform and plots them on one graph as either dotted solid or dashed line.

PHASE is a program which evaluates the phase of the first and second partitioned portions of the waveform. These partitioned sections are normally the first and second echos. Such phase measurements are necessary for evaluating velocity of sound measurements (fig. 34).

VELOCITY is a program which uses the phase information to determine the velocity of sound as a function of frequency by the equation (fig. 35)

$$v(\omega) = \frac{2\,d\omega}{\phi_2(\omega)-\phi_1(\omega)} \tag{18}$$

where: d is the sample thickness

ω is the angular velocity

$\phi_2(\omega)$ is the phase of the second echo

$\phi_1(\omega)$ is the phase of the first echo

ATTENUATION (fig. 36) is a program which uses information from the FFT of three partitioned portions of the waveform. The partitioned portions are the front and back surface echos and the second multiple echo. Using this information the acoustic attenuation α can be evaluated as a function of frequency by the equation

$$\alpha(\omega) = \frac{-1}{2d} \ln\left[\left|\frac{R_3(\omega)}{R_2(\omega)}\right| + \left|\frac{R_2(\omega)}{R_1(\omega)}\right|\right] \tag{19}$$

$R_1(\omega)$, $R_2(\omega)$ and $R_3(\omega)$ are the magnitudes of the Fourier transforms of the three partitioned waveforms.

A program was also written to list the data stored from the oscilloscope in a tabular form along with thickness and partition information. This program was called NICTABLE.

Normal Incidence Ultrasonic Pulse-Echo Measurements

Normal incidence pulse-echo measurements were made on $\pm 45°$ graphite samples, fifty percent of which had been moisture conditioned in a 90° C steam bath until they were saturated with moisture. Normal incidence pulse-echo measurements were also made on non-moisture conditioned neat resin samples. The resin type was that used in the AS3501-6 graphite/epoxy system. The acoustic attenuation coefficient α was evaluated by measuring a single sample thickness and the amplitudes of the front surface, back surface and second multiple echos. The acoustic attenuation is found by using the equation

$$\alpha = - \frac{1}{2d} \ln \left(\frac{R_3}{R_2} - \frac{R_2}{R_1}\right) \qquad (20)$$

where: α is the linear amplitude attenuation coefficient in mm^{-1}

d is the sample thickness in mm

R_1 is the amplitude of the front surface echo

R_2 is the amplitude of the back surface echo

R_3 is the amplitude of the second multiple echo

The results of the pulse echo attenuation measurements are summarized in Table 6. The high degree of scatter in the dry $\pm 45°$ graphite samples is due to the thin sample thickness and the difficulties associated with separating echos in thin laminates. Additional measurements were made on thick beam laminates and the resulting average attenuation for dry graphite epoxy was evaluated to be .0125 mm^{-1}. The average attenuation in the moisture saturated graphite epoxy was evaluated as .0543 and the neat resin had an average acoustic attenuation of .113 mm^{-1}. Average velocities of sound were also measured for normal incidence sound on graphite epoxy and neat resin. The values are 3190 m/sec for graphite and 2750 m/sec for the resin used in the AS3501-6 graphite epoxy system.

ANALYTICAL/EXPERIMENTAL DATA CORRELATION

STATIC SHEAR OF THICK LAMINATED BEAMS

Numerical results for a $[(0_4/\pm 45_2/\mp 45_2/0_4)_s]_s$ laminate with 64 plies and H/ℓ ratio of .05872 considered in reference 1 were obtained by the use of the methods presented. Two solutions obtained are discussed below.

1. Laminate stacking sequence is retained but $(\pm 45_2/\mp 45_2)$ layers are chosen as one material with average properties. Therefore the beam has nine layers of appropriate thicknesses with delamination at the mid-plane of the 0° layer at the center.
2. Since average properties (or equivalent elastic moduli) are often used in mechanics of composite materials a second solution was obtained by using average properties for the whole structure, i.e. a single layer with disbond at the mid-plane.

All elastic properties are listed below and are nondimensionalized by a factor E_0=6.895 GPa

Layers	C_{11}/E_0	C_{33}/E_0	C_{13}/E_0	C_{55}/E_0
1) 0	18.24	1.46	.409	.841
2) $(\pm 45_2/\mp 45_2)$	2.88	1.50	.134	.687
3) Average	10.92	1.48	.2	.756

These values are representative of those measured from experiments (reference 1). For averaging the properties, constant strain and constant stress hypotheses were used for computing stiffnesses parallel and perpendicular to laminations. 39 terms of the series and 20 collocation points were found to yield convergent solutions for all practical purposes.

Nondimensionalized stress intensity factors and strain energy release rates from the two elasticity solutions are shown in Table 7 for various values of a/ℓ. It is noted that if the

beam is considered as homogeneous, then the problem is equivalent to that with delaminations with applied shear stress equal to 1.5 P/2H on the surfaces, provided the delaminations are away from the load and the supports. For a/ℓ and a/h approaching zero, the limiting value of K_{II} should be $1.0607\ P\sqrt{a}/2H$. Although K_{II} is higher than this value for large a/ℓ, it is smaller for $a/\ell = .004$. Therefore, as a/ℓ is reduced further, K_{II} should approach the limit from below. This trend is similar to the trends reported in Reference 16. Values of K_{II} at both tips differ only in the third significant figure (given here to two decimal places). Mode I intensity factors are extremely small and will not have any influence on propagation of the disbonds. This is expected since H/ℓ is only .05872. Therefore, the conjecture made in Reference 1 regarding effects of concentrated loading on retarding crack growth possibility is incorrect. For larger disbond lengths such effects may have some influence.

One interesting fact is that the nondimensionalized value of K_{II} from both theories are closer for smaller crack lengths but the strain energy release rates are far apart. It is clear that stresses will have similar distributions near the tips of the disbonds for small a/ℓ. The difference in G occurs due to the difference of H^0_{22} in the two theories. Percentage difference in G, however, decreases as a/ℓ is increased. Therefore averaged properties may be used with proper caution and correction to obtain reasonably accurate results. Critical loads and strain energy rates are compared with beam theory solutions and experimental data in Table 8 and fig. 37. Fig. 37 shows that beam theory yields critical loads, which are larger than elasticity solutions. The difference is large for small a/ℓ ratios but is gradually reduced as a/ℓ increases. To some extent this reduces the discrepancy in measured G_c values for two disbond lengths. The difference in G_c computed from experimental data by the use of beam theory solution is 44%, whereas if elasticity solution

is utilized, the difference is reduced to 20%, which is less than the experimental scatter for each disbond length.

Critical values of strain energy release rates obtained by the use of results from tests on precracked $[(0/90)_6 0_{12}]_s$ laminates and exact elasticity solutions considering stacking sequence are given in Table 9. After comparing these results with those in Table 8 (exact elasticity) it appears that values of G_c obtained from (i) precracked $[(0/90)_6 0_{12}]_s$ specimens and (ii) $[(0_4/\pm 45_2/\mp 45_2/0_4)_s]_s$ laminated beams without any pre-cracking of the disbonds, are of the same order and show same amount of scatter. Precracking, therefore, does not have any significant influence on catastropic disbond growth under static shear.

PROPAGATION DISBOND IN FATIGUE

The fatigue test samples with diamond shaped defects could not be precracked to obtain a straight line crack front. Fatigue tests were therefore conducted with the implanted shapes. Lengths of extended disbonds were measured from "C" scans with an accuracy of $\pm$.6 mm after specified number of cycles, N, at six locations, three in each implanted disbond in the thick beam specimens as shown in figure 38. It is clear from figures 6-17 that at locations 3 and 6, both at mid-width of the beams, little or no extension occurred. The reason for this phenomenon is not quite clear but may be attributed to the fact that the stress distribution near these corners are different in nature as compared to that near the edges (see reference 17). Extension of disbonds at locations 1, 2, 4 and 5 were also not uniform, i.e. significantly more extensions occurred at some locations as compared to others. This behavior is expected because of local non-uniformities in materials and shapes of the disbond tips.

Disbond lengths at locations 1, 2, 4 and 5 were plotted against N and reasonably smooth curves were obtained. Some

sample plots are shown in figures 39-42. Figures 40-42 show that in some locations a plateau exists in a vs. N plots. This type of behavior is usually observed in metals when sudden overloads occur at a certain point in a loading cycle. No apparent reason was found for this behavior from the testing program. It is possible that material nonhomogeneities encountered during crack growth (existence of weak locations) may also result in such behavior. Nonhomogeneities in composites are usually much more severe than those in metals. It should be pointed out, however, that this type plateau were observed in one or two locations a limited number of samples, namely .75-5, 1.00-4, 1.00-6 and 1.25-7.

Slopes $\Delta a/\Delta N$ of a-N curves were then calculated at various points along the a-N curve. Values of a at these points were used to calculate ΔK, the stress intensity factor range by using methods described earlier in pages 6-8. Values of $\frac{da}{dN}$ are plotted against ΔK in figures 43,44 & 45 for initial disbond sizes of 19.05 mm (0.75"), 25.4 mm (1") and 31.75 mm (1.25 in) respectively. These dimensions are those of the diagonals of the diamonu shaped disbonds i.e. approximate measure of disbonds at locations 3 and 6. A least square fit to the data points in figures 43, 44 and 45 yield the following values of the parameters C and n for the power law relationship $\frac{da}{dN} = C(\Delta K)^n$

$$C = 2.044 \times 10^{-23} \text{ in SI units (N,m)}$$

$$= 2.222 \times 10^{-13} \text{ in lb. and inch units}$$

$$n = 2.776$$

It is noted that the disbonds did not propagate in a self similar fashion and pointwise measurements were used to obtain the empirical crack propagation law. However, the relationship is obtained from measurements made near the free edges, which are purely in a state of plane stress and therefore, it is expected that this relationship will be useful for predicting

growth of flaws under such a state of stress. Care must be taken in using the data presented here for studying propagation of disbonds under states of plane strain or other general conditions of loading in the case of disbonds having two dimensional planar form.

BUCKLING OF DISBONDED COMPRESSION SKIN

Properties of beam elements and the honeycomb core used for correlations with experimental results are shown in Table 10. Results of failure stress versus disbond length are shown in figure 46. The analytical prediction is similar to the Euler stress versus column slenderness ratio curves. The cut-off is set at the test data for the compressive strength without defects, which is equal to 689.5 MPa. It is clear that the analytical predictions correlate extremely well with experimental data when the disbond length is 19.05 mm or more.

Experimental results for 12.7 mm long disbonds (about 414 MPa), however, fall well below the compressive strength of 689.5 MPa and the buckling stress of 793 MPa. This discrepancy appears to be due to inelastic behavior. Test data for 0° layers show that the axial stress-strain response is linear up to the strain level under consideration. $\pm 45°$ laminates show a slight deviation from linearity, but it is likely to have no influence on the axial and bending stiffnesses of the beam elements, which are dominated by the 0° layers. It is known, however, that shear stress-strain responses of fiber reinforced composites are highly nonlinear and therefore, in the presence of axial compressive stress, the value of tangent modulus in shear (ratio of shear stress increment or strain increment) could be significantly less than the initial modulus (especially in $\pm 45°$ layers). Estimation of the correct value of tangent modulus will involve the formulation of an appropriate yield criterion and a trial and error procedure for determining the value of critical stress. Such estimation is beyond the scope of this work. To study the effect of reduced

shear modulus, calculations were repeated (for 12.7 mm disbond length) with a shear modulus 1/4th of the initial modulus. The results show that the buckling stress is reduced to 541 MPa from 793 MPa. Lower values of tangent modulus will yield critical stress comparable to 414 MPa observed experimentally. It appears, therefore, that the analytical flaw criticality criterion is in good agreement with experimental results for elastic material behavior.

DISCUSSIONS AND CONCLUSIONS

In the analytical/experimental data correlation studies presented herein, usefulness of the proposed NDE methodology has been demonstrated. The following important conclusions and comments can be made based on the results of the present study.

1. Use of ultrasonic "C" scans is an effective technique for detection and growth of the types of interlaminar disbonds considered in this study.

2. Linear elastic fracture mechanics approach in conjunction with the methods of stress analysis presented here is useful for assessing criticality of flaws in presence disbonds which are in a state of shear. The analysis method can be extended to the case of multiple number of flaws at different locations as in the case of impact damage.

3. A semi-empirical crack growth law can be used for predicting growth of flaws due to cyclic shear. It appears that by the use of this law and the failure models proposed herein an assessment of residual strength and/or residual lifetime can be made. Further study in this direction should help in checking the accuracy of such assessments.

4. Presence of disbonds can significantly lower the load carrying capacity of a laminated compression member and reduced (or residual) strength can be estimated using the model used here.

5. It is noted that all methods, results and criteria developed herein are of limited use, i.e. for the types of disbonds and geometry of the beam type structure considered. Use of these results for other types of disbonds (2D planar form is an example) and different types of structure should be made with due consideration to the difference in such geometric configuration and further studies are needed before standard tools for practical use are developed.

6. Moisture conditioning has a significant influence on attenuation of ultrasonic waves and damages induced by such conditioning may be assessed from the results of wave propagation studies in conjunction with the analytical relationships presented.

REFERENCES

1. Ramkumar, R.L., Kulkarni, S.V., Pipes, R.B. and Chatterjee, S.N., "Analytical Modelling and ND Monitoring of Interlaminar Defects in Fiber Reinforced Composites," ASTM STP 677, 1979.

See also

Ramkumar, R.L., Kulkarni, S.V. and Pipes, R.B., "Definition and Modelling of Critical Flaws in Graphite Fiber Reinforced Composites," NADC-76228-30, January 1978.

2. Wang, S.S., "An Analysis of Edge Delamination Crack in Composite Laminate under Axial Extension," ASTM Technical Specialists Conference on NDE and Flaw Criticality for Composite Materials, Philadelphia, PA, October 10-11, 1978.
3. Rybicki, E.F. and Kanninen, M.F., Eng. Fracture Mechanics, V. 9, p.931, 1977.
4. Guydish, J.J. and Fleming, J.F., Eng. Fracture Mechanics, V. 10, p.31, 1978.
5. Williams, M.L., Journal of Adhesion, V. 4, 1972.
6. Kulkarni, S.V. and Frederick, D., International Journal of Fracture Mechanics, V. 9, 1973.
7. Updike, D.P., International Journal of Fracture, V. 12, pp. 815-827, 1976.
8. Ramkumar, R.L., Ph.D. Dissertation, Virginia Polytechnic Institute and State University, 1976.
9. Majumdar, S. and Morrow, JoDean, "Correlation between Fatigue Crack Propagation and Low Cycle Fatigue Properties," ASTM STP 559, pp. 159-182, 1974.
10. Liu, H.W. and Iino, N. "A Mechanical Model for Fatigue Crack Propagation," Proc 2nd International Conference on Fracture, paper 71, pp. 812-823, Chapman-Hall, 1969.
11. Stouffer, D.C. and Williams, J.F., Engineering Fracture Mechanics, V. 11, pp. 526-536, 1979.
12. Kanninen, M.F., Atkinson, C. and Fedderson, C.E., "A Fatigue Crack Growth Analysis Method Based on a Simple Representation of Crack-Tip Plasticity," ASTM STP 637, pp. 122-140, 1977.

REFERENCES (Cont'd.)

13. Christensen, R.M., Theory of Viscoelasticity, Academic Press, 1969.

14. Hashin, Z., "Complex Moduli of Viscoelastic Composites," I, II, International Journal of Solids Structures, V. 6, pp. 539-552, 797-807, 1970.

15. Hashin, Z., "Analysis of Properties of Fiber Composites with Anisotropic Constiuents," Journal of Applied Mechanics, September, 1979.

16. Fichter, W.B., "Stresses at the Tip of a Longitudinal Crack in a Plate Strip," NASA Tech. Rep., R-265, 1967.

17. Parihar, K.S. and Keer, L.M., Journal of Applied Mechanics, V. 45, pp. 791-796, 1978.

18. Gradshteyn, I.S. and Ryzhik, I.M., Table of Integrals, Series and Products, Academic Press, 1965.

19. Sih, G.C., Ed., Methods of Analysis and Solutions to Crack Problems, Chapter 7, Wolters-Noordhoff, 1972.

20. Muskhelishvili, N.I., Singular Integral Equations, Wolters-Noordhoff, 1972.

Table 1

Static Shear Test Results for Precracked $[(0/90)_6 0_{12}]_s$ Laminates

Sample No.	Defect Type	Precrack Length mm (inch)	Failure Loan N (lb.)
1-1	1" Square	70 (2.75)	1451 (326.4)
1-3	1" Square	30 (1.18)	4272 (961.2)
1-6	1" Square	26 (1.02)	4233 (952.4)
D-2	Diamond	39 (1.54)	2940 (661.4)
D-5	Diamond	46 (1.81)	2332 (524.8)
D-3	Diamond	40 (1.57)	2204 (496.0)

Table 2

Static Shear Test Results for $[(0_4/\pm 45_2/\mp 45_2/0_4)_s]_s$
Laminates with Diamond Shaped Defects

Specimen	Debond Length mm (in.)	Failure Load N (lb.)	Average N(lb.)
0.75-1	19.05(0.75)	9021(2028)	
0.75-2	19.05(0.75)	9314(2094)	9167(2061)
1.00-1	25.4(1.00)	8433(1896)	
1.00-2	25.4(1.00)	8611(1936)	
1.00-7	25.4(1.00)	8184(1840)	
1.00-8	25.4(1.00)	8331(1873)	8389(1886)
1.25-1	31.75(1.25)	7255(1631)	
1.25-2	31.75(1.25	5685(1278)	
1.25-5	31.75(1.25)	7842(1763)	
1.25-6	31.75(1.25)	7450(1675)	7059(1587)

Table 3

Fatigue Test Results for $[0_4/\pm 45_2/\mp 45_2/0_4)_s]_s$

Laminates with Diamond Shaped Defects

Laminate:

Specimen	Debond Length mm (in.)	S Level	Cycles to Failure
0.75-7	19.05(0.75)	0.6	35,045
0.75-8	19.05(0.75)	0.6	12,035
0.75-3	19.05(0.75)	0.5	68,121
0.75-4	19.05(0.75)	0.5	64,433
0.75-5	19.05(0.75)	0.4	------
0.75-6	19.05(0.75)	0.4	725,293
1.00-9	25.4(1.00)	0.6	9,627
1.00-10	25.4(1.00)	0.6	11,199
1.00-4	25.4(1.00)	0.5	46,070
1.00-6	25.4(1.00)	0.5	79,991
1.00-11	25.4(1.00)	0.5	48,751
1.00-12	25.4(1.00)	0.5	48,835
1.00-13	25.4(1.00)	0.4	150,623
1.00-14	25.4(1.00)	0.4	194,019
1.25-3	31.75(1.25)	0.75	5,034
1.25-4	31.75(1.25)	0.75	5,000
1.25-7	31.75(1.25)	0.5	27,572
1.25-8	31.75(1.25)	0.5	29,000
1.25-9	31.75(1.25)	0.5	28,468
1.25-10	31.75(1.25)	0.5	16,095
1.25-11	31.75(1.25)	0.4	47,477
1.25-12	31.75(1.25)	0.4	57,633
1.25-13	31.75(1.25)	0.3	>2,250,000
1.25-14	31.75(1.25)	0.3	412,957

Table 4

Test Results for Buckling Failure

Sample Number	Defect Size (in.) mm	Location Location	Load at Failure, N	Stress at Failure (MPa)
18	None	---	9,709	642
19	None	---	10,101	668
20	None	---	10,983	726
21	None	---	11,670	771
				Avg. 702
1T	(1/2) 12.7	Center	5,982	395
10B	(1/2) 12.7	Center	6,571	415
				Avg. 405
15T	(3/4) 19.05	Center	6,963	460
16T	(3/4) 19.05	Center	4,560	301
16B	(3/4) 19.05	Center	5,492	364
17T	(3/4) 19.05	Center	4,707	311
17B	(3/4) 19.05	Center	7,183	480
				Avg. 383
3T	(1) 25.4	Center	2,324	154
7B	(1) 25.4	Center	2,942	194
12T	(1) 25.4	Center	2,599	172
8B	(1) 25.4	Center	2,942	194
				Avg. 179
6T	(1.5) 38.1	Center	1,314	86.9
5T	(1.5) 38.1	Center	1,373	90.8
11T	(1.5) 38.1	Center	1,304	86.2
9B	(1.5) 38.1	Center	1,618	107
				Avg. 92.7
3B	(1) 25.4	Near Surface	98	6.48
12B	(1) 25.4	Near Surface	98	6.48
7T	(1) 25.4	Near Surface	218	14.3
8T	(1) 25.4	Near Surface	128	8.43
				Avg. 8.92
5B	(1.5) 38.1	Near Surface	---	---
6B	(1.5) 38.1	Near Surface	---	---
11B	(1.5) 38.1	Near Surface	---	---
9T	(1.5) 38.1	Near Surface	---	---

Table 5

Moisture Conditioning Effects on $[\pm 45]_{2s}$ Laminates

Specimen	Conditions		Shear Modulus GPa (msi)		Shear Strength MPa (ksi)
422	Pristine		5.6 (.81)		82.7 (12.0)
421	Pristine		5.4 (.78)		86.2 (12.5)
433	Pristine		5.5 (.8)		81.4 (11.8)
		Avg.	5.5 (.8)	Avg.	83.4 (12.1)
424	120 days @ 100% RH		4.9 (.71)		71.7 (10.4)
411	120 days @ 100% RH		4.6 (.66)		67.6 (9.8)
414	120 days @ 100% RH		4.6 (.67)		71.0 (10.3)
		Avg.	4.7 (.68)	Avg.	70.1 (10.2)

Table 6

Pulse-Echo Attenuation Coefficient α

Sample ID	Thickness mm	α mm^{-1}
Dry Resin No. 1	5.08	.106
Dry Resin No. 2	6.84	.110
Dry Resin No. 3	5.08	.124
Dry Graphite		
±45 Graphite No.1D	1.15	.0190
±45 Graphite No.2D	1.15	.00097
±45 Graphite No.3D	1.15	.0072
Saturated Graphite		
±45 Graphite No.1W	1.15	.058
±45 Graphite No.2W	1.15	.079
±45 Graphite No.3W	1.15	.026
Thick Beam No.1	8.86	.0136
Thick Beam No.2	8.86	.0101

Table 7

Stress Intensity Factors and Strain Energy Release Rates-
$[(0_4/\pm45_2/\mp45_2/0_4)_s]_s$ Laminates

Elasticity Theory	a/ℓ	$\frac{K_{Ic}2H}{P\sqrt{a}}$	$\frac{K_{Id}2H}{P\sqrt{a}}$	$\frac{K_{II}2H}{P\sqrt{a}}$ at c & d	$\frac{G E_0 \ell}{P^2}$ at c & d
	.004	-.0005	.002	-1.06	.206
	.025	-.005	.006	-1.09	1.38
Averaged	.0417	-.004	.005	-1.15	2.55
Properties	.0833	.003	-.004	-1.30	6.53
	.1667	.0004	.0001	-1.60	19.8
	.26	.0001	.004	-1.89	42.9
	.004	-.0004	.002	-1.02	.139
	.025	-.005	.006	-1.08	.976
Considering	.0417	-.004	.005	-1.17	1.89
Stacking	.0833	.003	-.003	-1.37	5.20
Sequence	.1667	.0004	.0003	-1.72	16.5
	.26	.0002	.004	-2.05	36.4

Table 8

Critical Loads and Strain Energy Release Rates from Various Theories-[$(0_4/\pm45_2/\mp45_2/0_4)_s]_s$ Samples

a/ℓ	$P_{cr}/\sqrt{G_c}$, $(N.m)^{1/2}$ Elasticity (average)	Elasticity (exact)	Beam (Ref.1)
1/6	185	203	217
1/12	322	361	434

Specimen	a/ℓ	$P_{cr}/2$, N (exptl.)	G_c, N/m Elasticity (average)	Elasticity (exact)	Beam (Ref.1)
1-1	1/6	3187	1185	986	864
1-2		3383	1335	1111	974
1-3		2304	619	515	452
1-4		2598	787	655	574
Average			982	817	716
1/2-1	1/12	4657	837	666	461
1/2-2		4510	785	624	432
1/2-3		4782	882	702	486
Average			835	664	460

Table 9

Critical Loads and Strain Energy Release Rates from Precracked $[(0/90)_6 0_{12}]_s$ Laminates

Sample	a/ℓ	$P_{cr}/2$,N	$\mathcal{G}_c$, N/m Elasticity (Exact)
1-1	.46	726	765
1-3	.197	2,138	1,144
1-6	.171	2,118	879
D-2	.256	1,471	916
D-5	.302	1,167	725
D-3	.262	1,103	513
		Avg.	824

Table 10

Properties of Beam Elements and Core

of Sandwich Beams

Beam Stiffness	Beams 1 and 2 $(0/\pm45/\mp45/0)$	Beams 3 and 4 $(0/\pm45/\mp45/0)_s$
Axial A	4.22×10^7 N/m	8.44×10^7 N/m
Bending D	3.444 N.m	19.14 N.m
Coupling B	0	0
Shear $k_{55}C^*_{55}$	3.20×10^6 N/m	6.40×10^6 N/m
Thickness	.7601 mm	1.5202 mm

Core (Honeycomb ALC-1/8-5052-.006-22.1 ∿ Aluminum Corrugated) Properties

Young's Modulus; E_c = 5.17 Gpa

Shear Modulus; G_c = 2.55 Gpa

Core Thickness; H_c = 38.1 mm

Subgrade Modulus in Extension = E_c/H_c = 135.7 GN/m^3

Subgrade Modulus in Shear = G_c/H_c = 66.93 GN/m^3

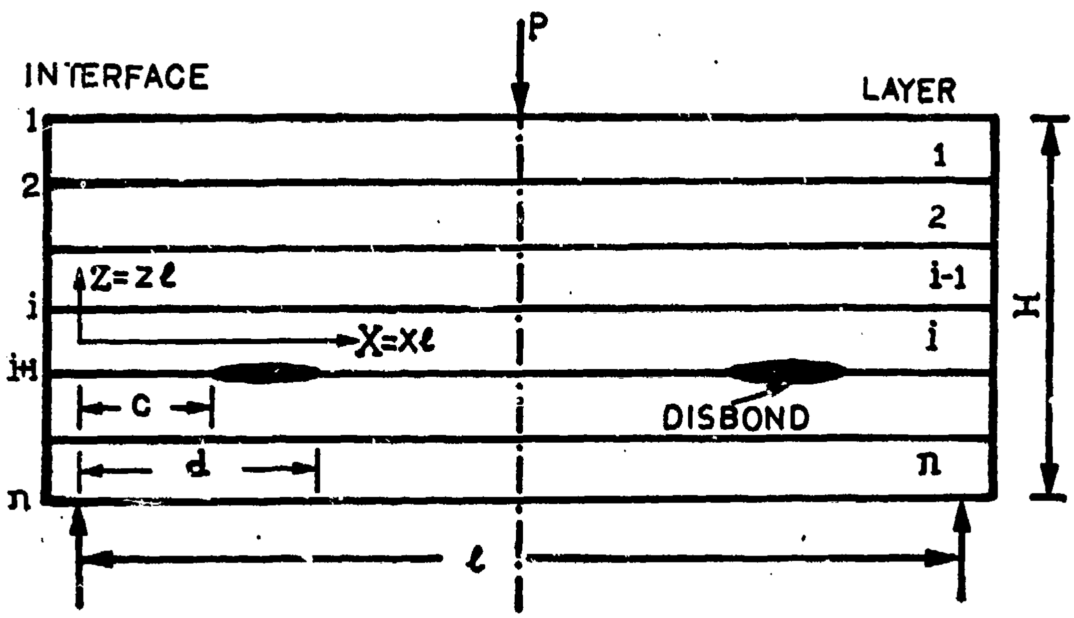

Figure 1. Laminated Beam Containing Disbonds

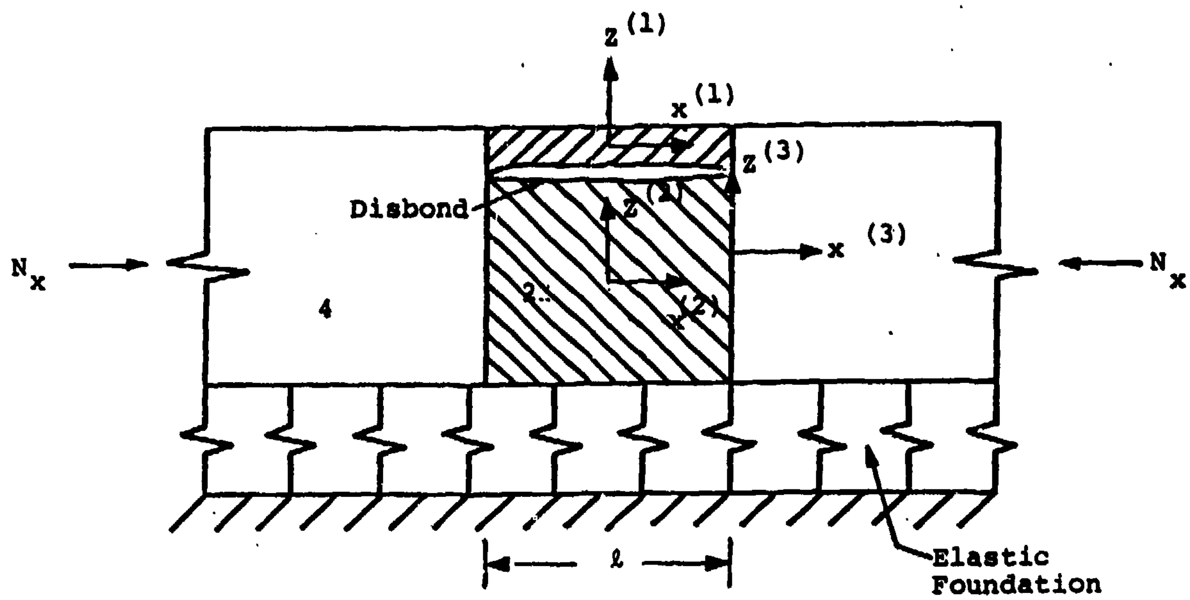

Figure 2. Model of Compression Skin

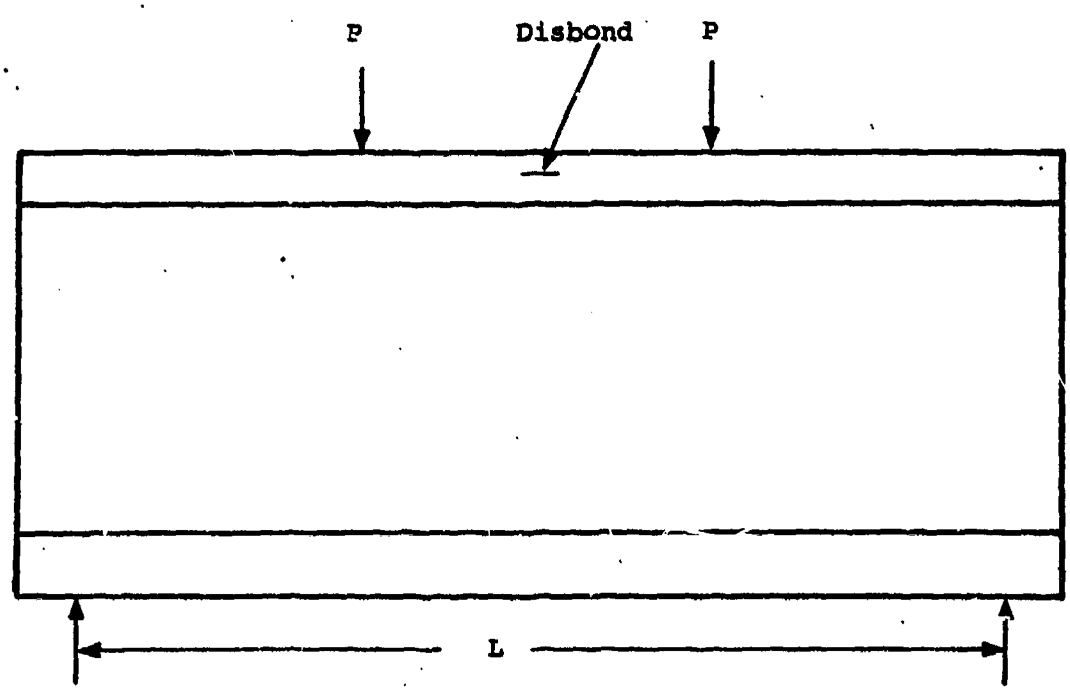

Figure 3. Sandwich Beam Specimen
with Disbonded Compression Skin

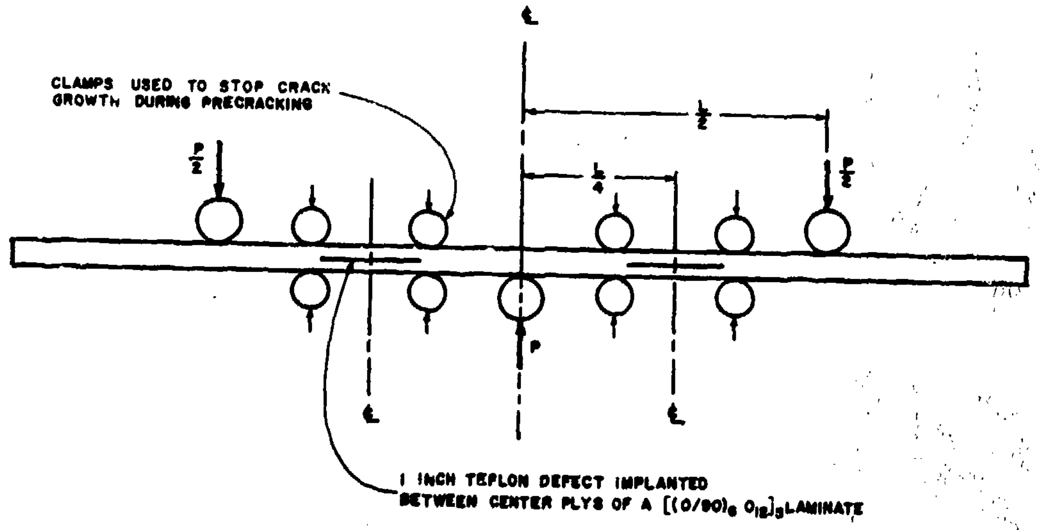

Figure 4. Thick Laminate Shear Beam Configuration

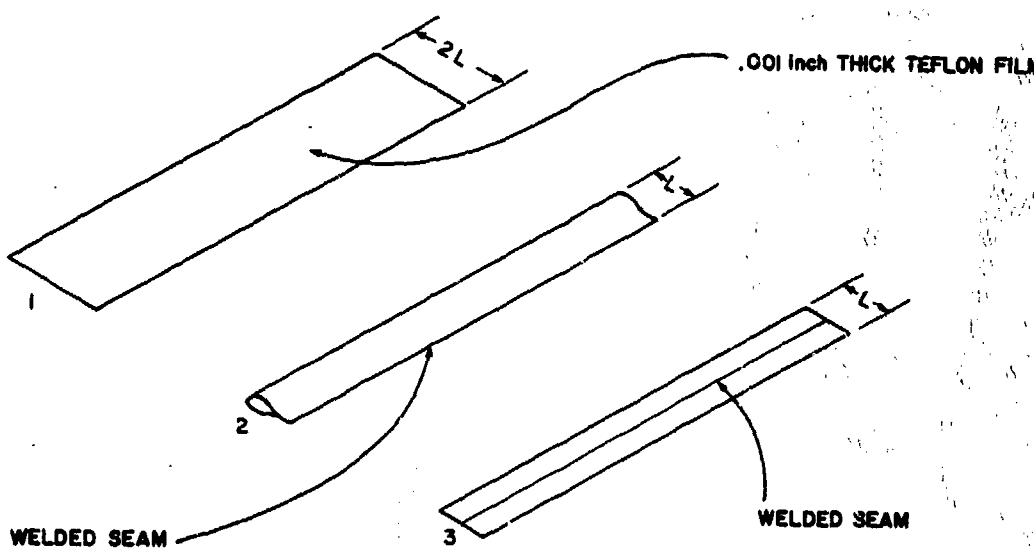

Figure 5. Disbond Fabrication Method

Figure 6. "C" Scan of Specimen 0.75-6, S=0.4

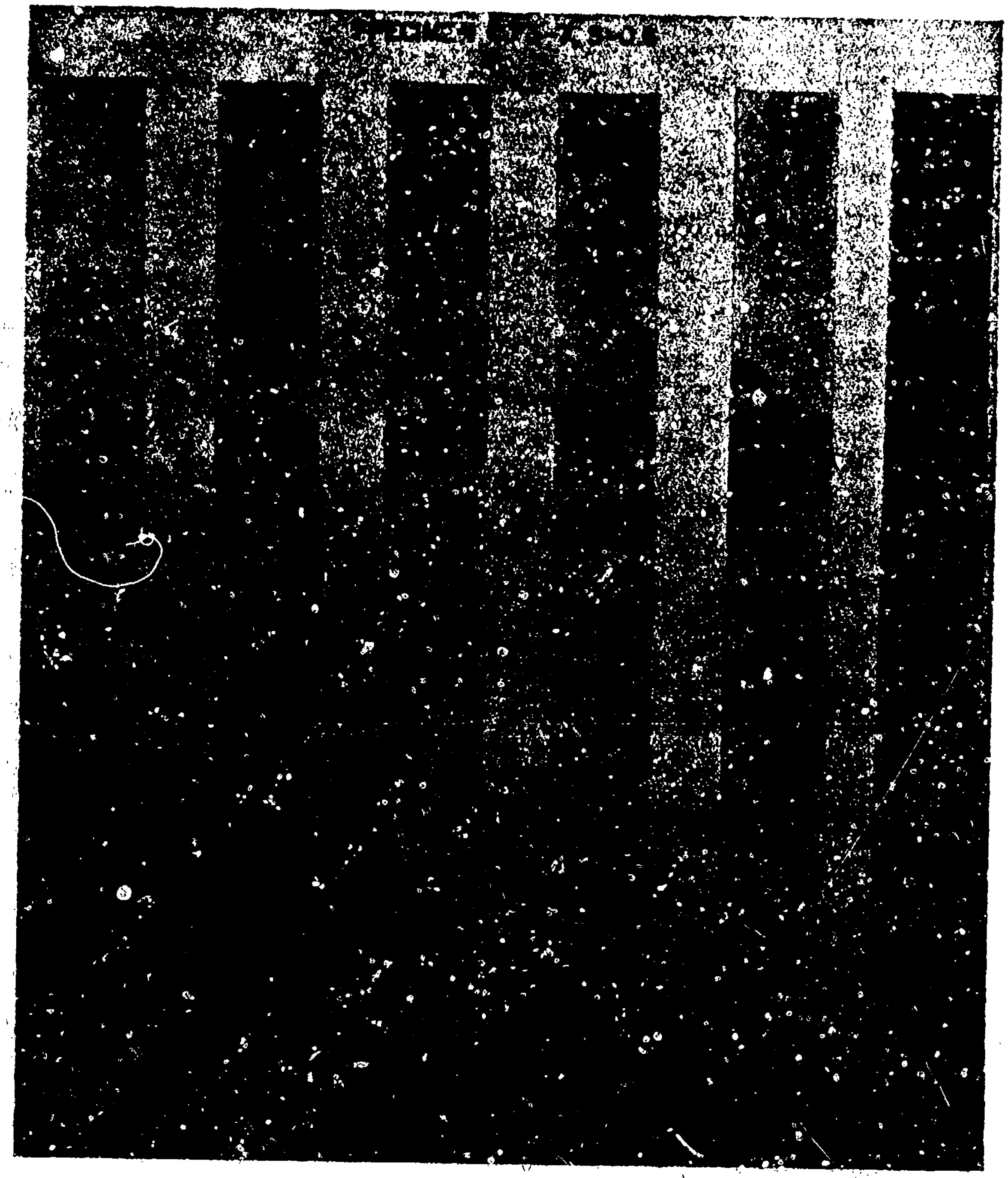

Figure 7. "C" Scan of Specimen 0.75-7, S=0.6

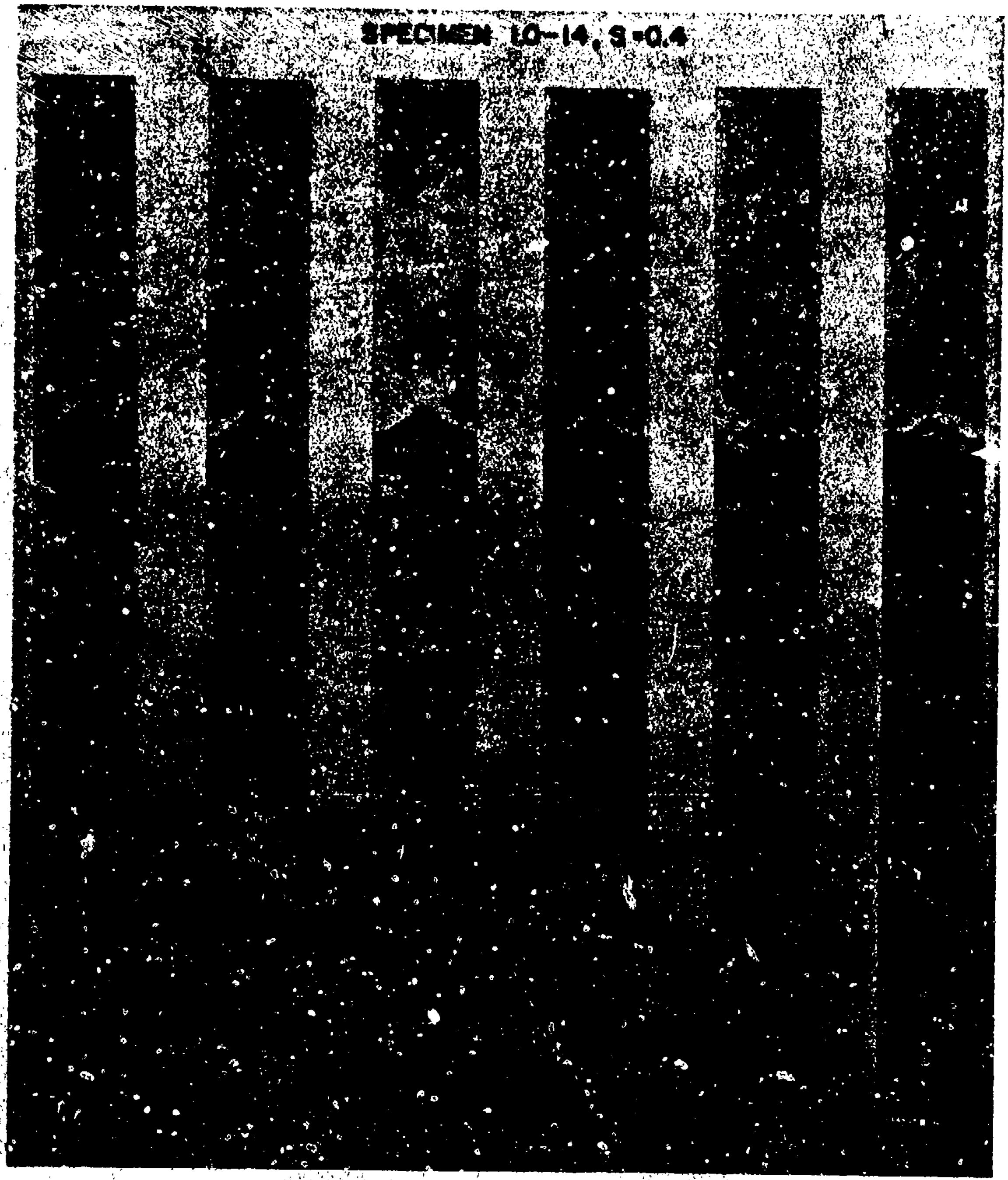

Figure 8. "C" Scan of Specimen 1.0-14, S=0.4

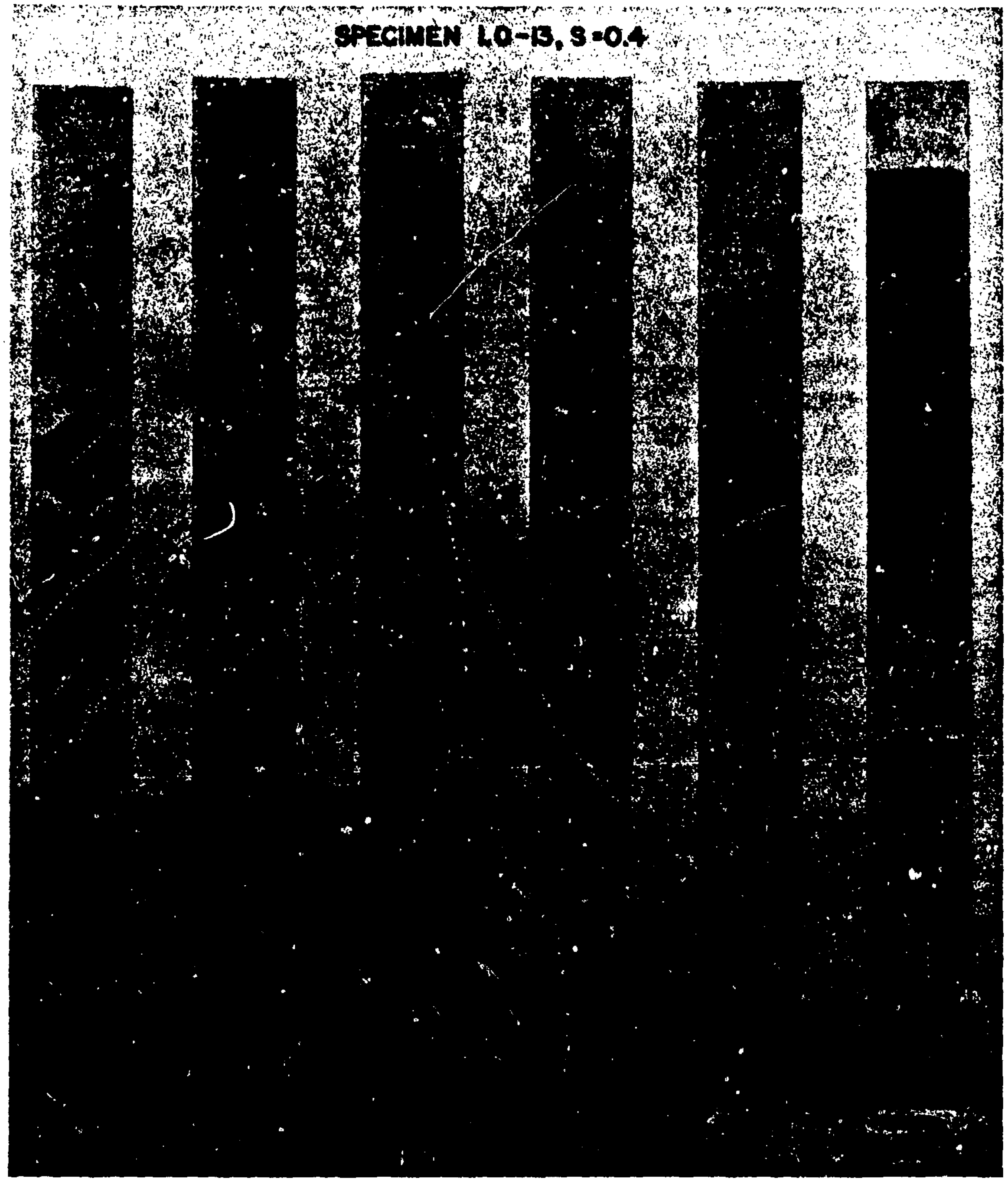

Figure 9. "C" Scan of Specimen 1.0-13, S=0.4

Figure 10. "C" Scan of Specimen 1.0-12, S=0.5

SPECIMEN 1.0-10, S=0.6

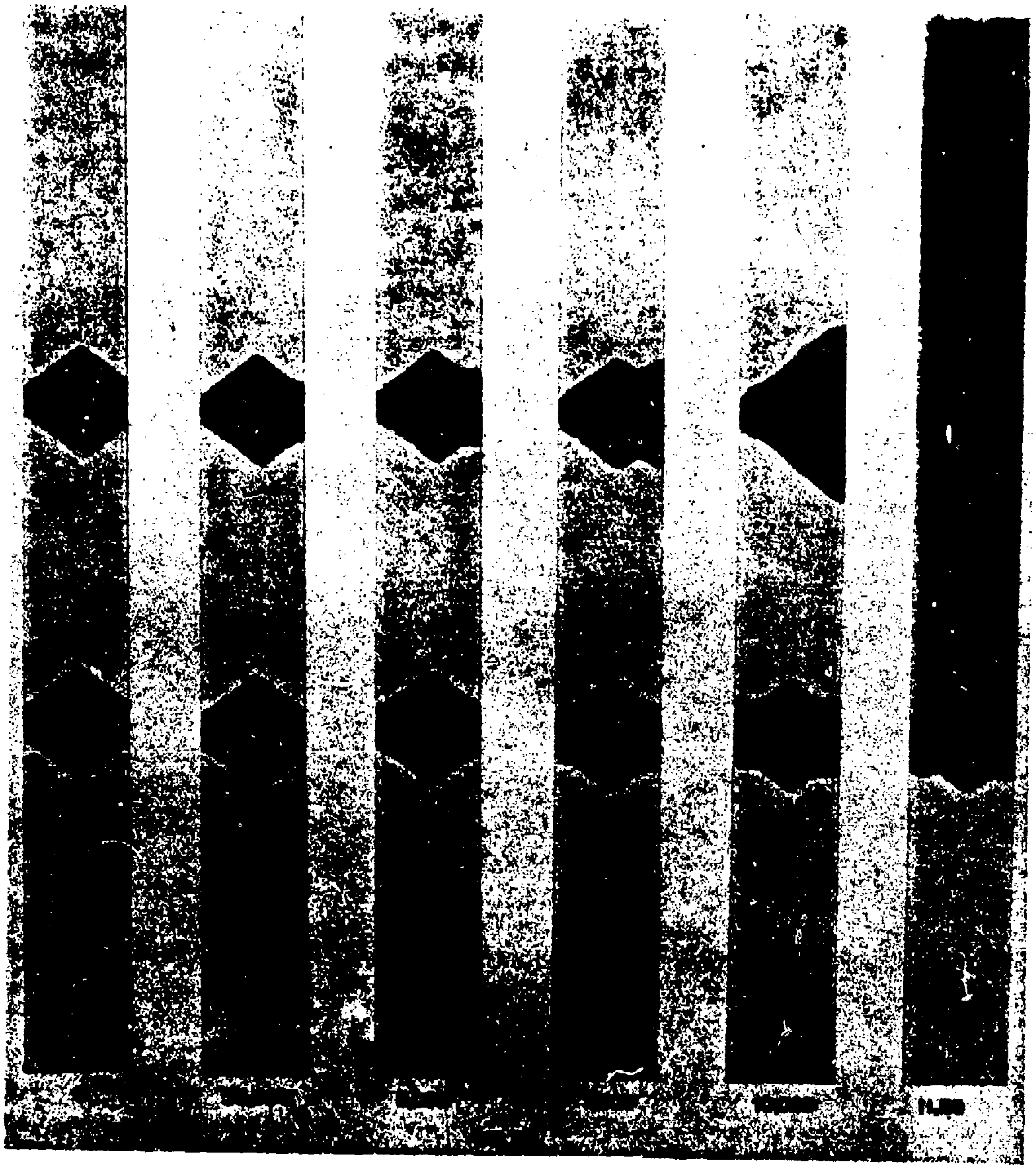

Figure 11. "C" Scan of Specimen 1.0-10, S=0.6

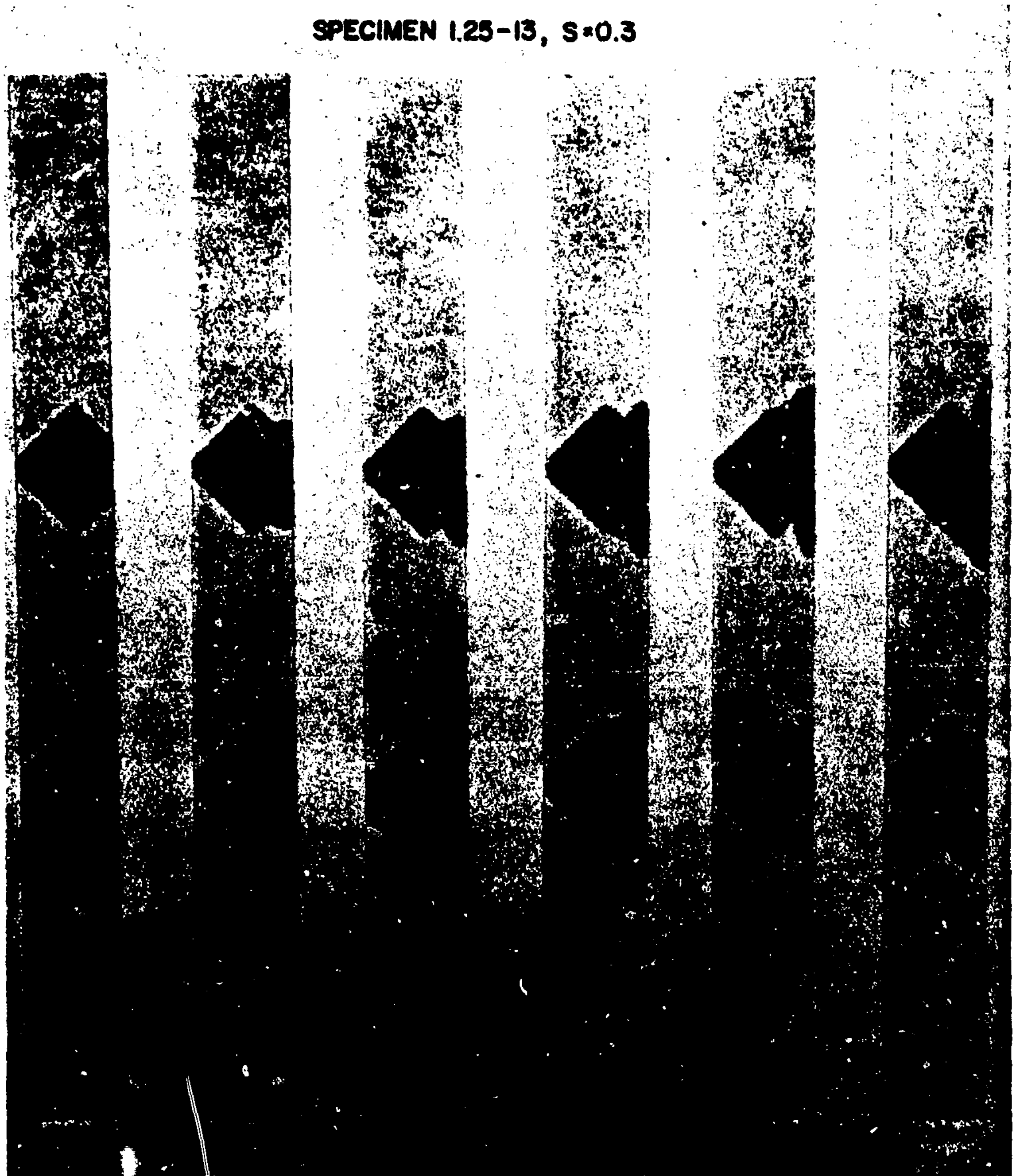

Figure 12. "C" Scan of Specimen 1.25-13, S=0.3

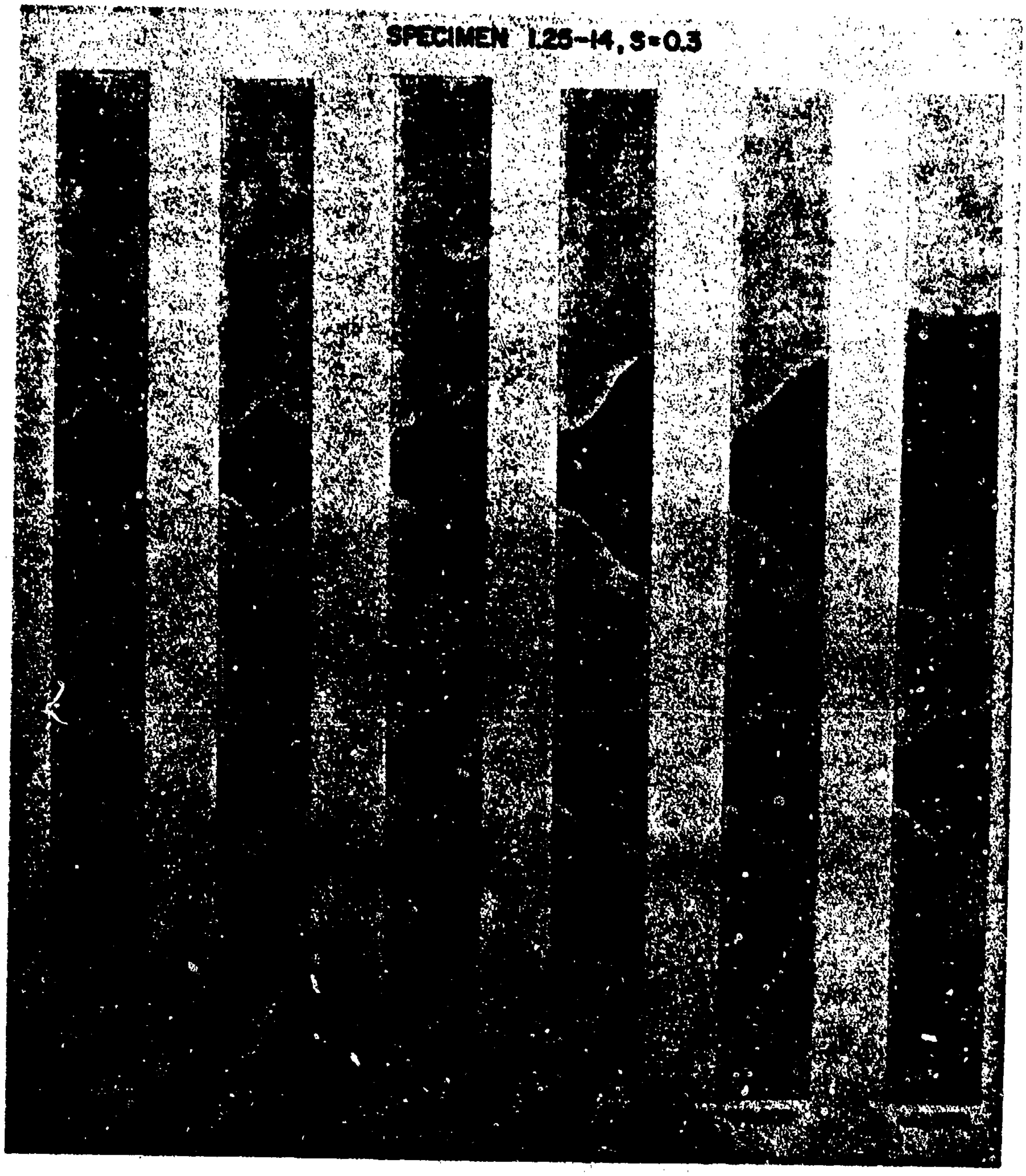

Figure 13. "C" Scan of Specimen 1.25-14, S=0.3

Figure 14. "C" Scan of Specimen 1.25-11, S=0.4

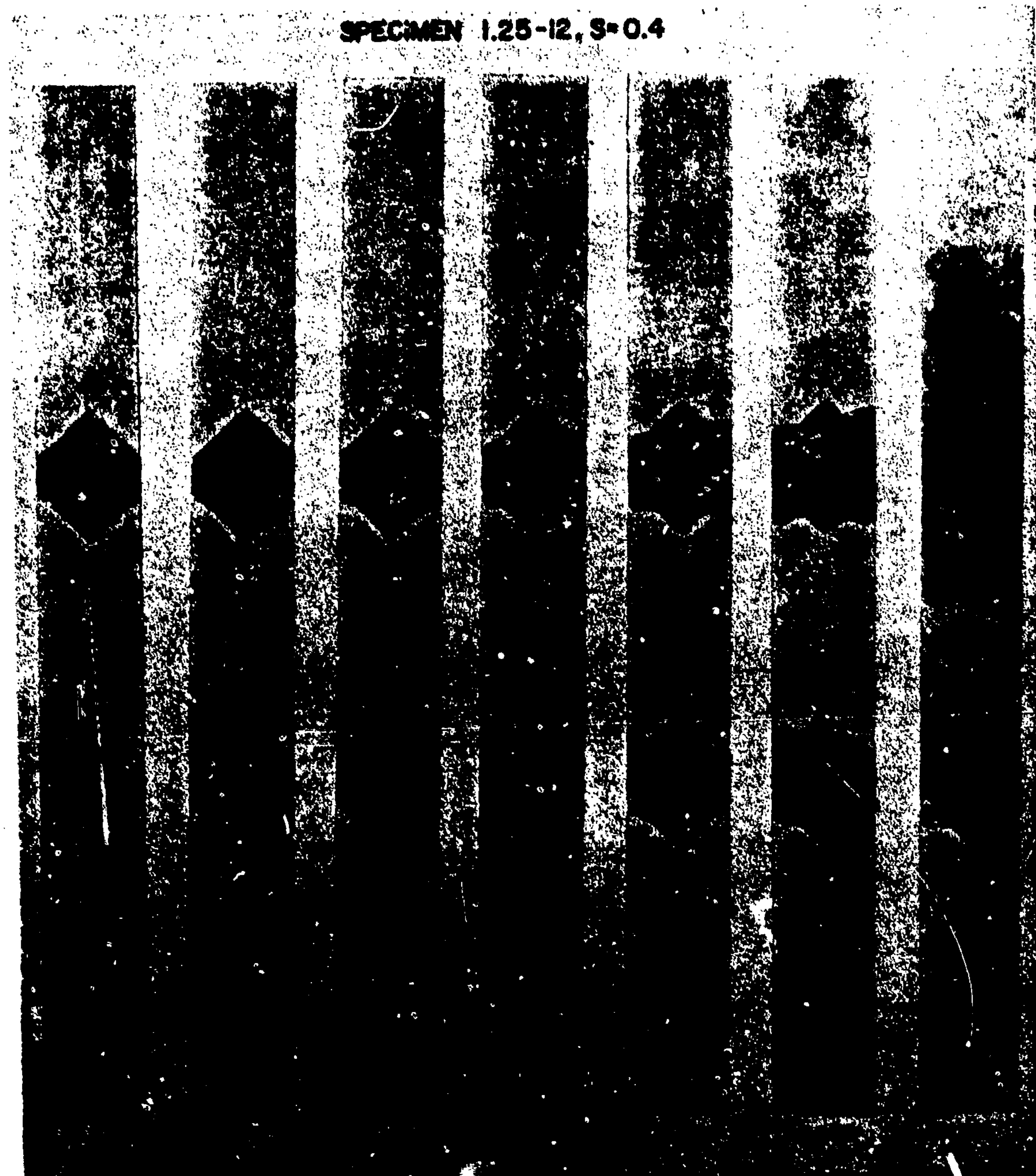

Figure 15. "C" Scan of Specimen 1.25-12, S=0.4

Figure 16. "C" Scan of Specimen 1.25-8, S=0.5

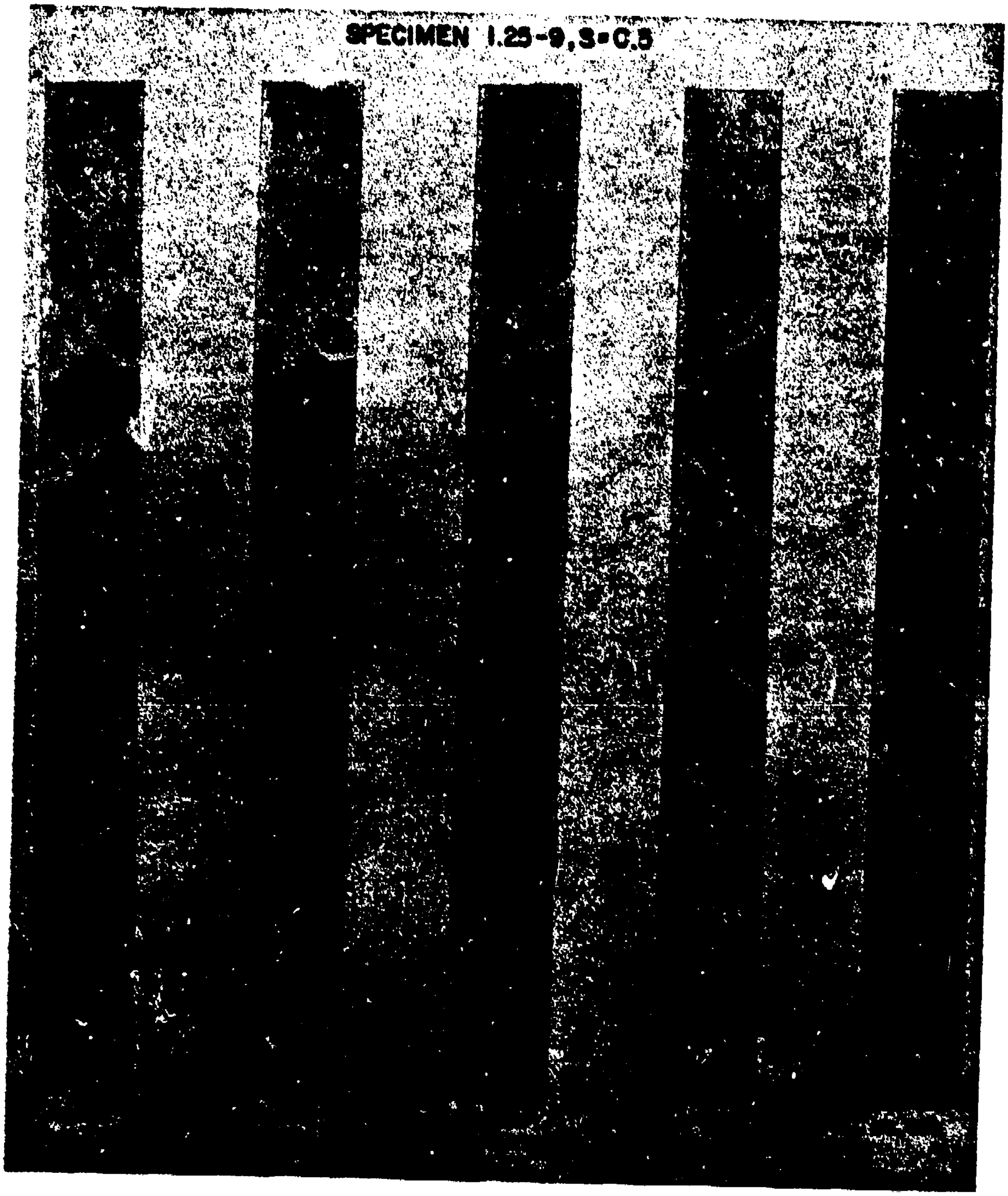

Figure 17. "C" Scan of Specimen 1.25-9, S=0.5

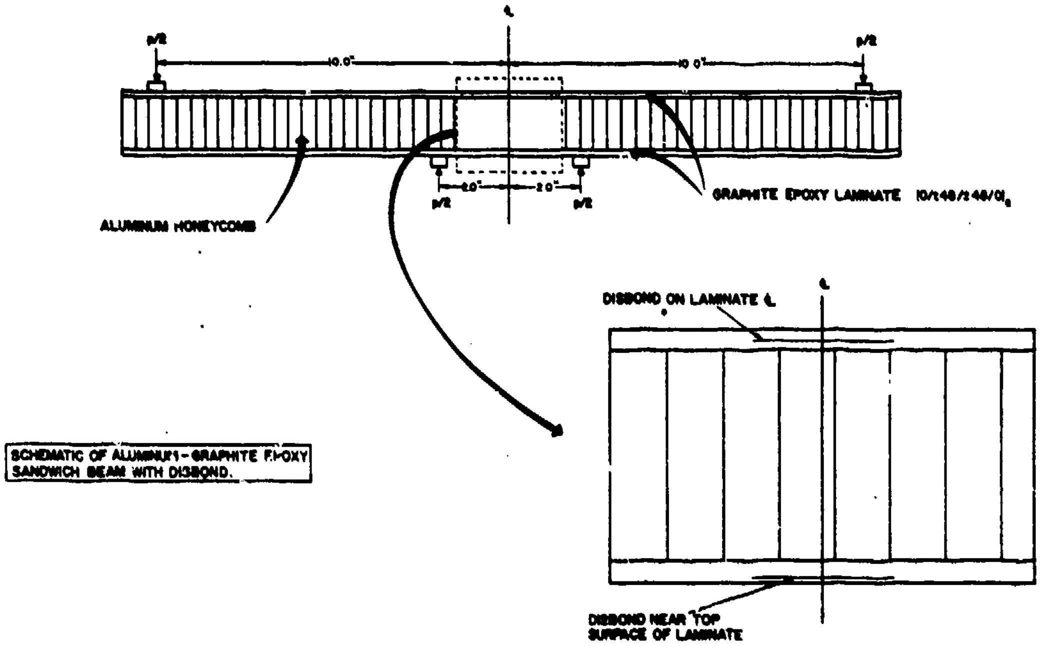

Figure 18. Sandwich Beam Specimen Geometry

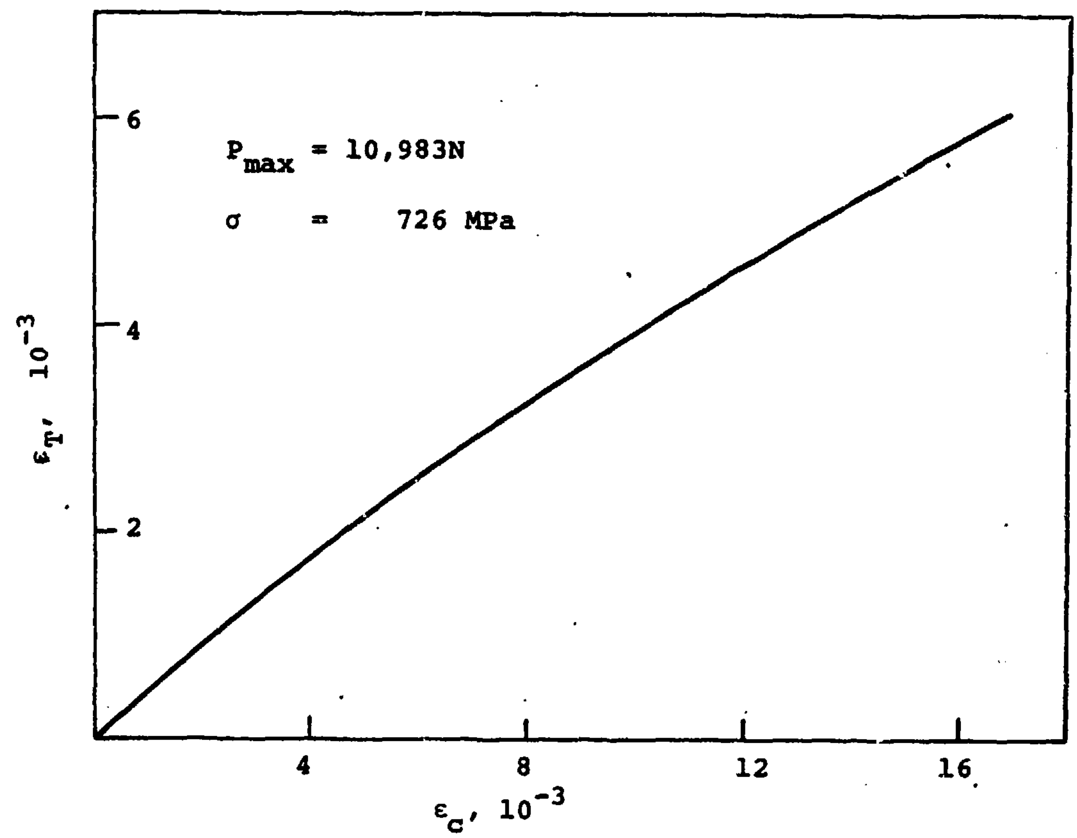

Figure 19. ε_T vs. ε_c for Specimen 20, No Defect

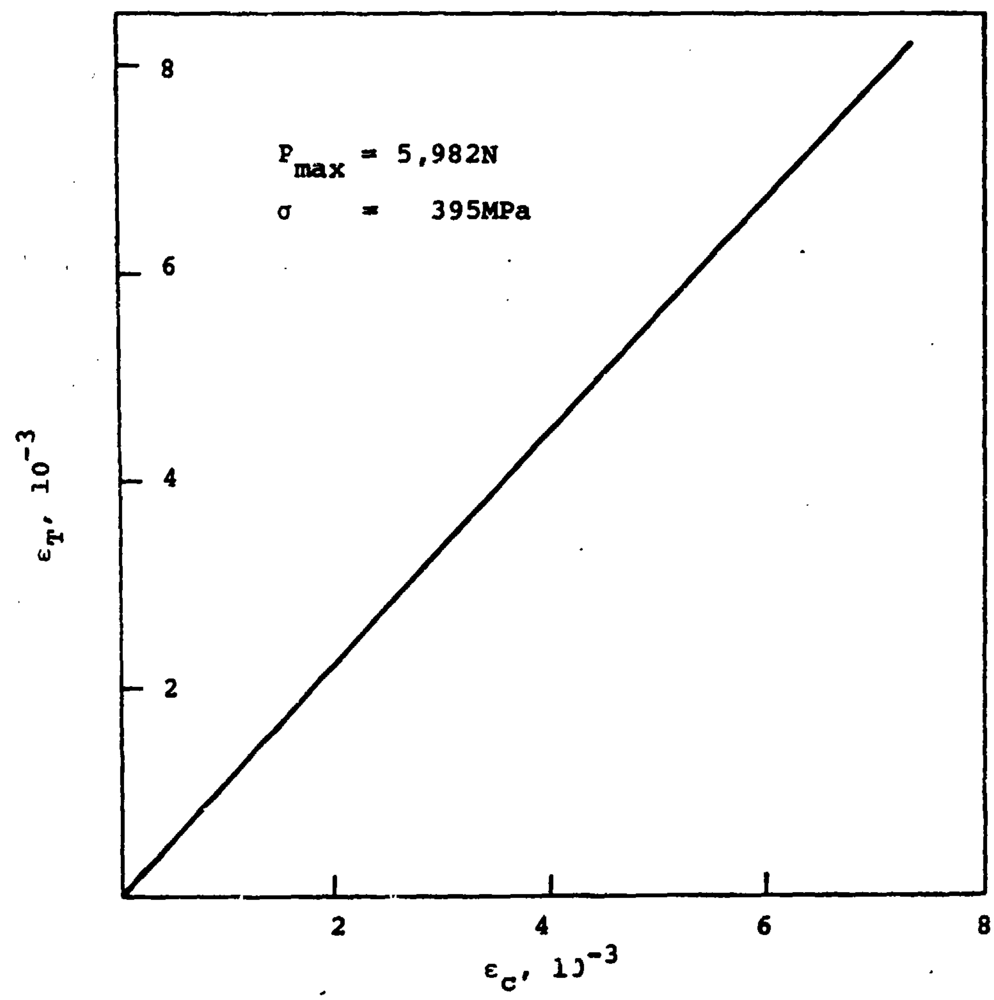

Figure 20. ε_T VS. ε_C for Specimen 1T, 12.7 mm. Center Defect

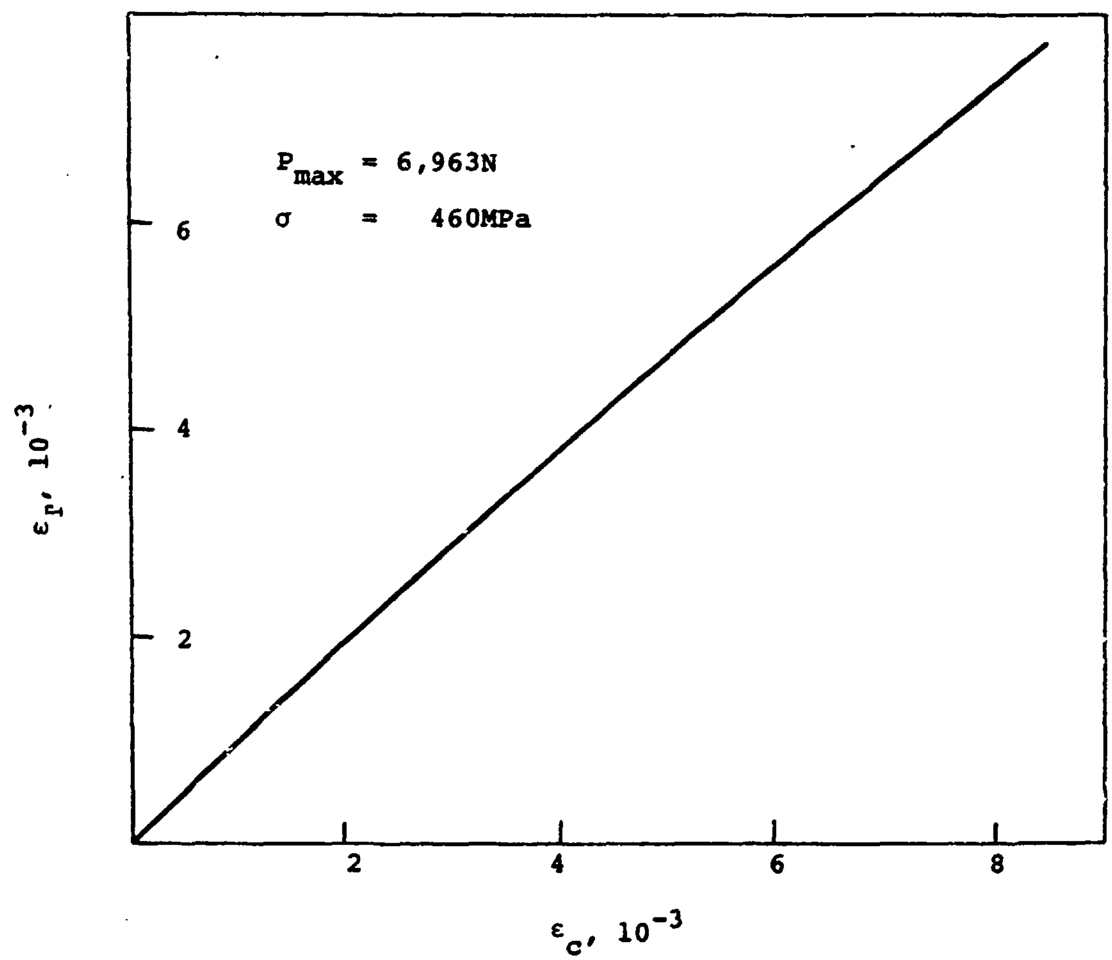

Figure 21. ε_T vs. ε_c for Specimen 15T, 19.05mm. Center Defect

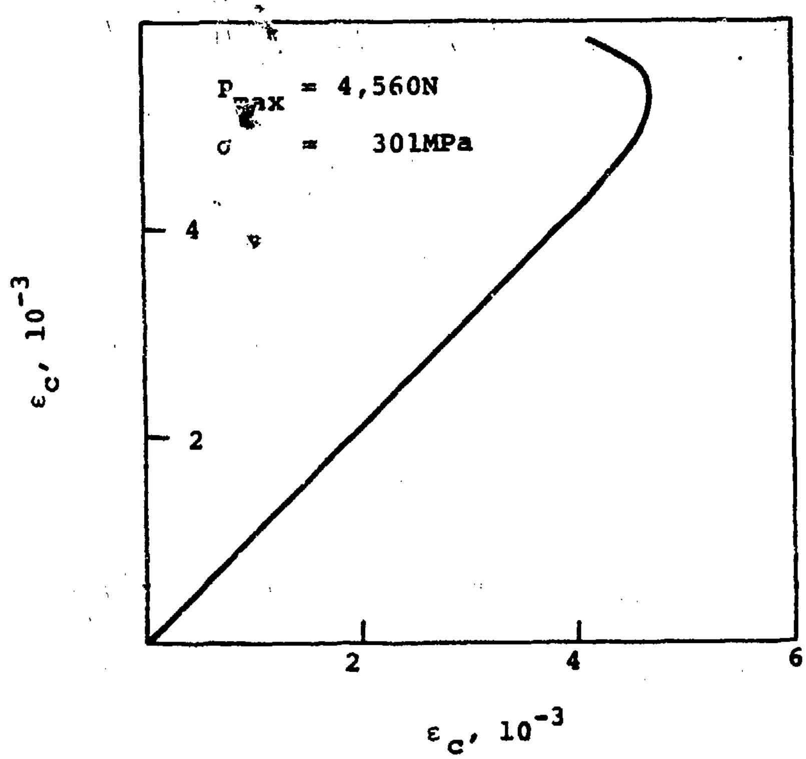

Figure 22. ε_T vs. ε_c for Specimen 16T, 19.05mm. Center Defect

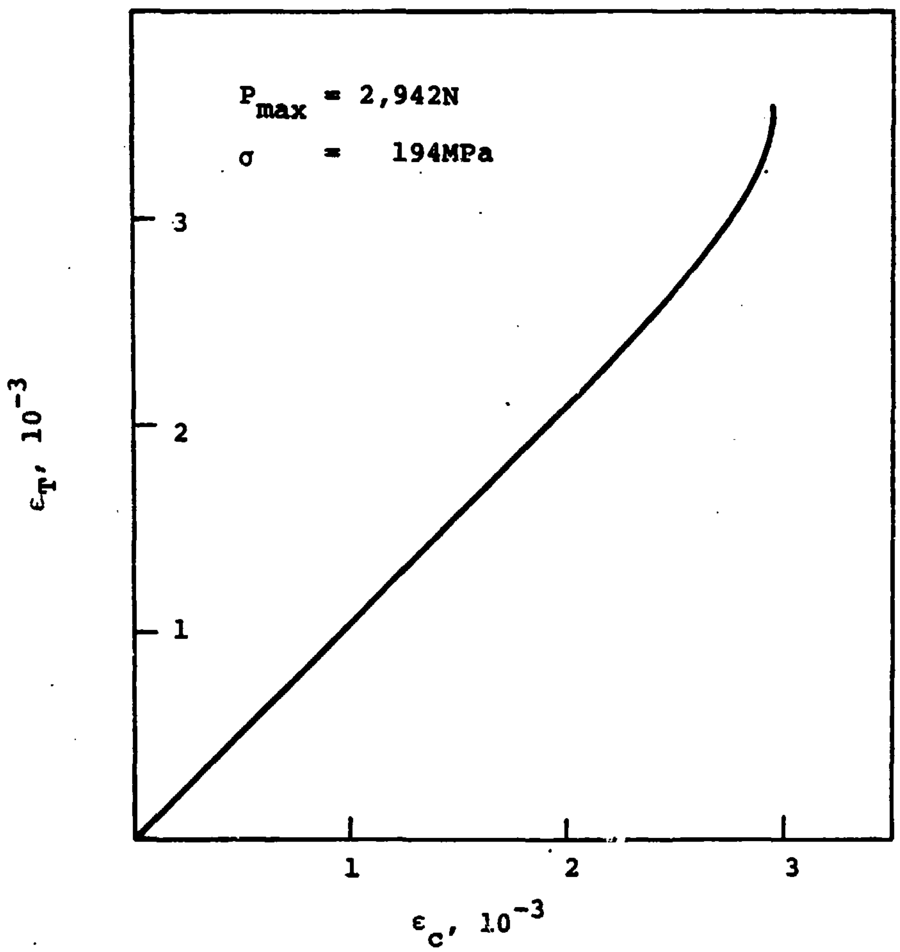

Figure 23. ε_T vs. ε_c for Specimen 7B, 25.4mm. Center Defect

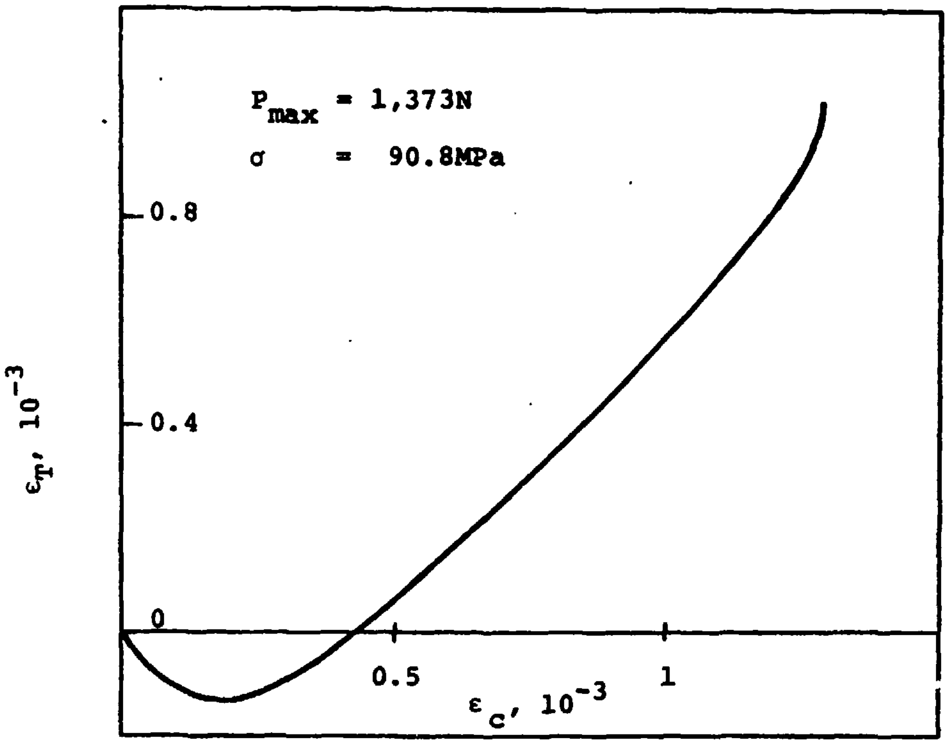

Figure 24. ε_T vs. ε_c for Specimen 5T,

38.1mm. Center Defect

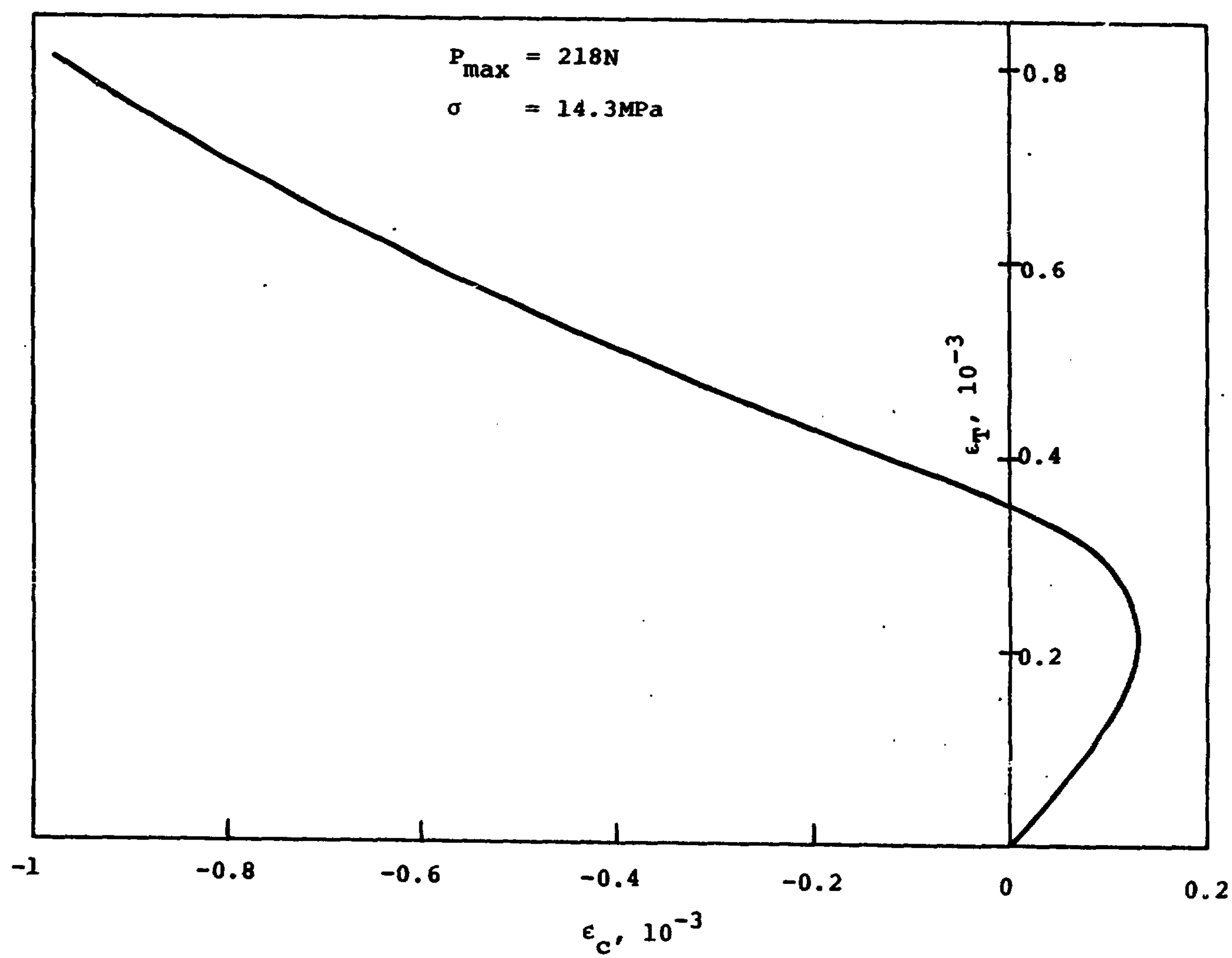

Figure 25. ε_T vs. ε_c for Specimen 7T, 25.4 mm. Near Surface Defect

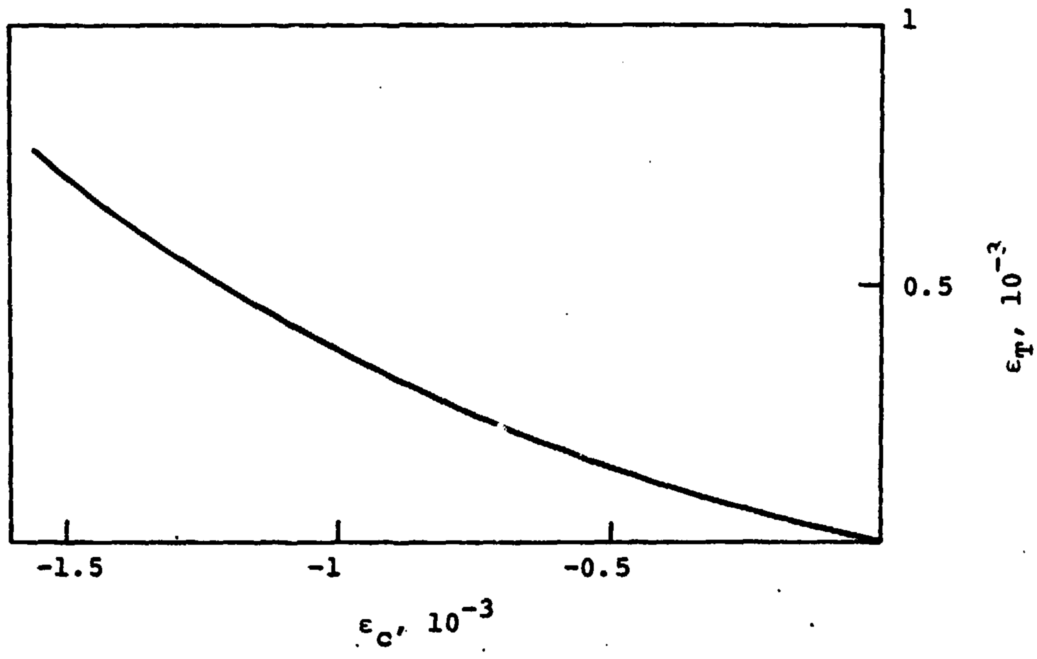

Figure 26. ε_T vs. ε_c for Specimen 9T, 38.1mm. Near Surface Defect

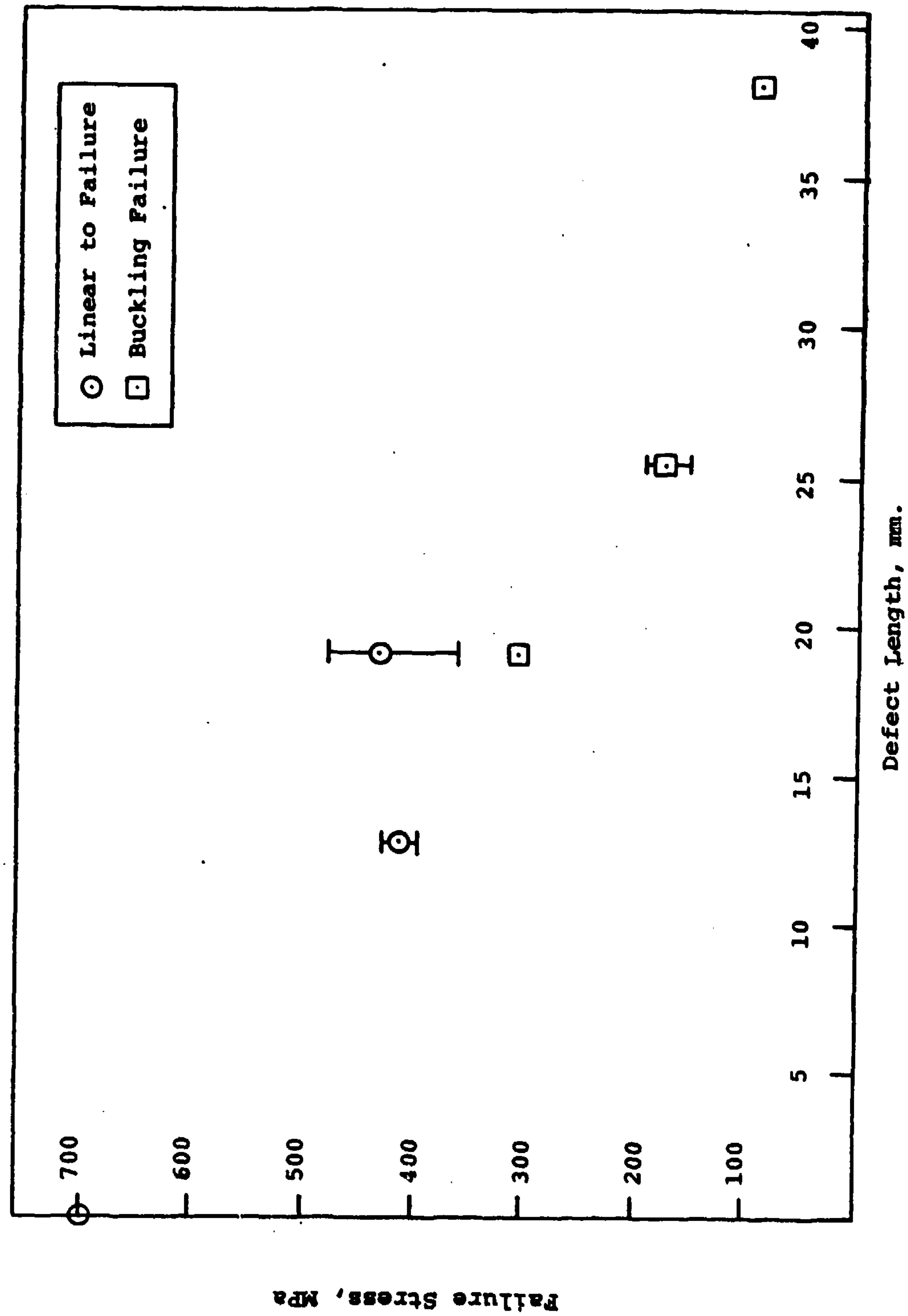

Figure 27. Effect of Center Defect Length on Compressive Buckling Strength

Figure 28. Fractured Specimen 1T-0.5 in Center Defect

Figure 29. Fractured Specimen 17B-0.75 in Center Defect

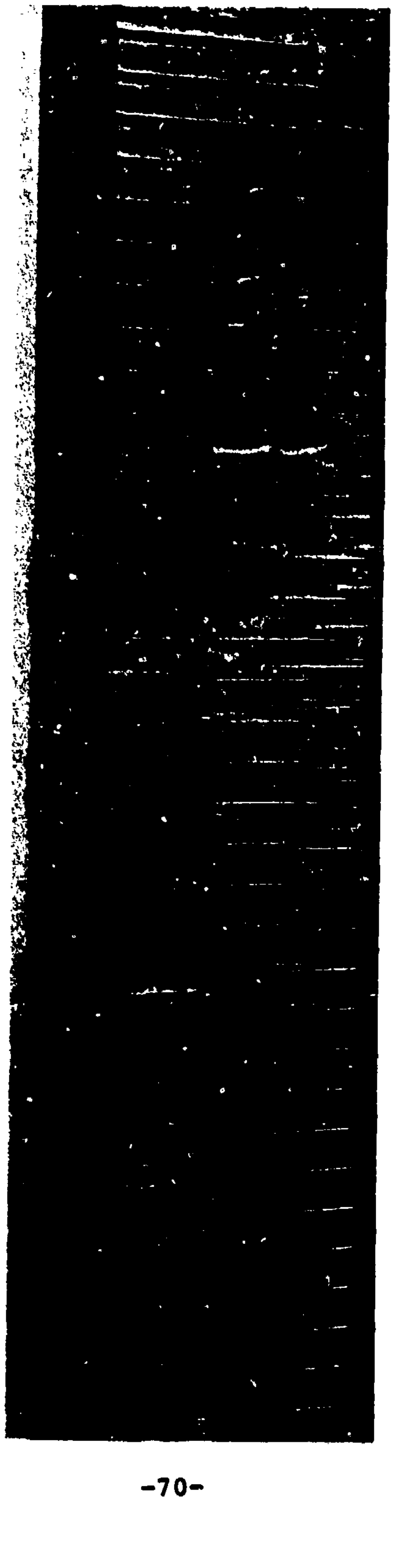

Figure 30. *Fractured Specimen 5B-1.5 in Near Surface Defect*

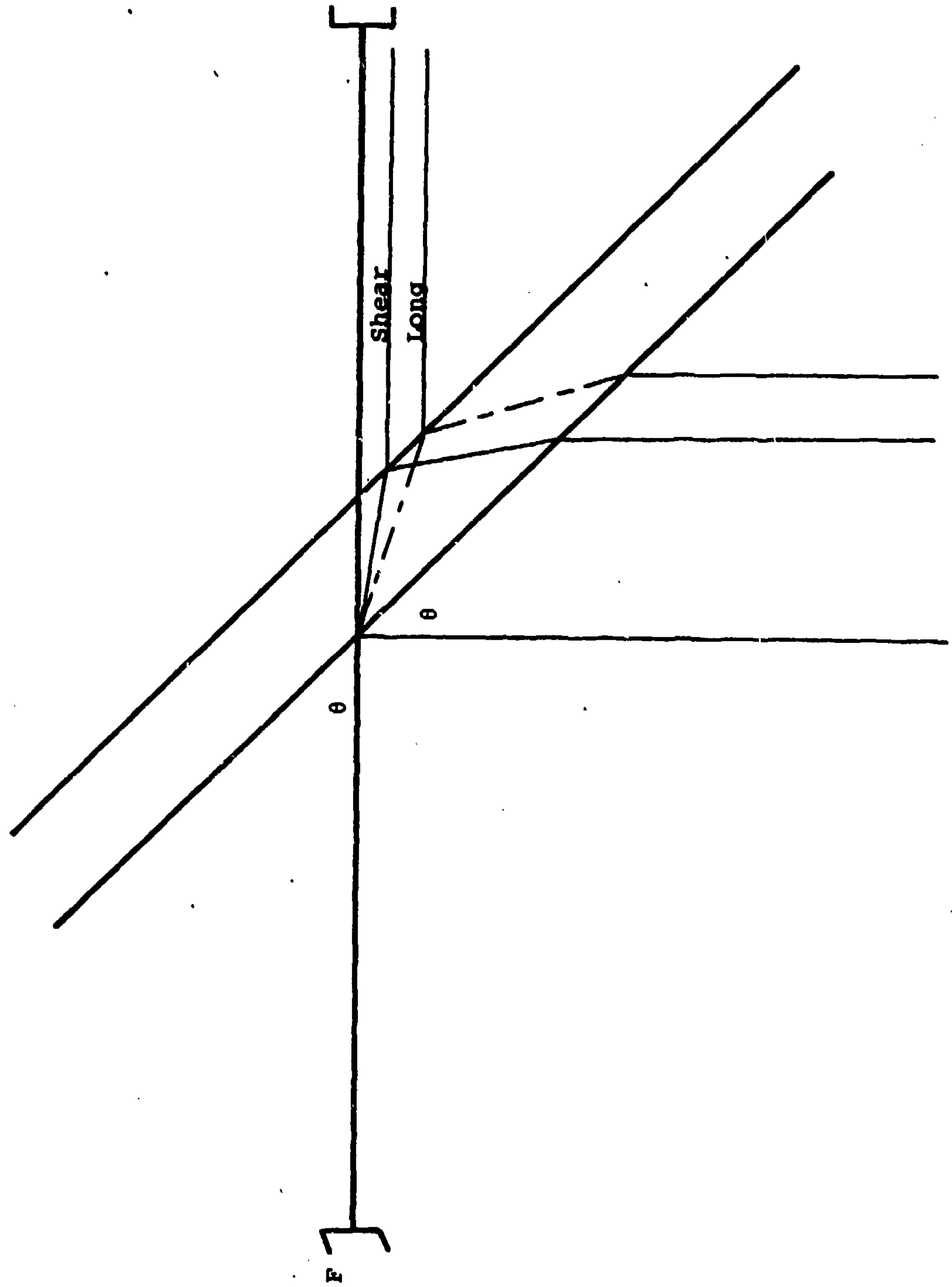

Figure 31. Non-Normal Incidence Mode Conversion

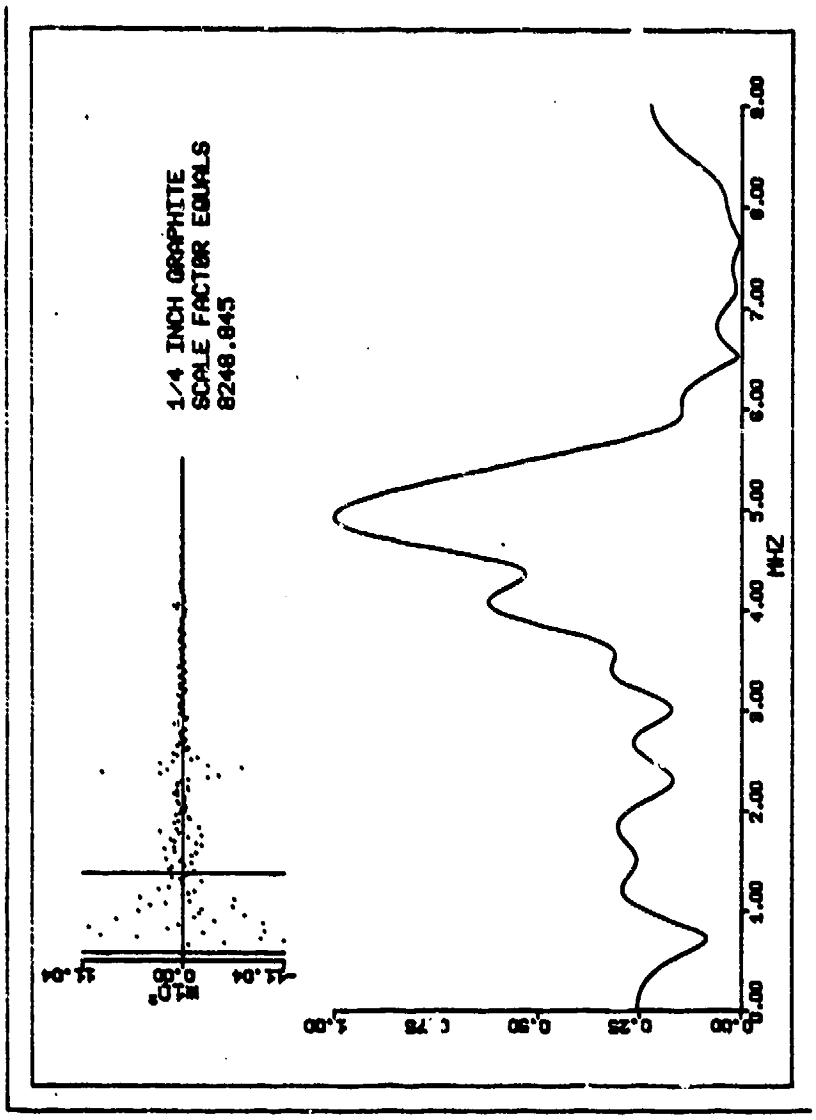

Figure 32. Graphic Output of SELECTRUM Program

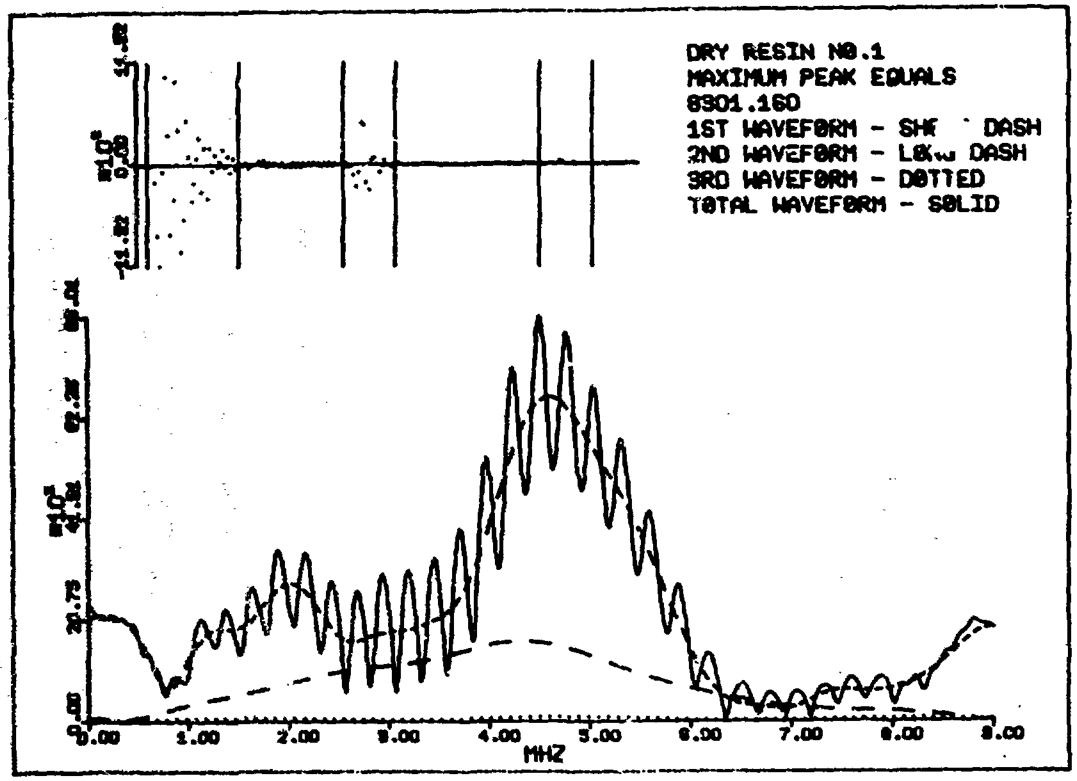

Figure 33. Graphic Output of COMPARETRUM Program

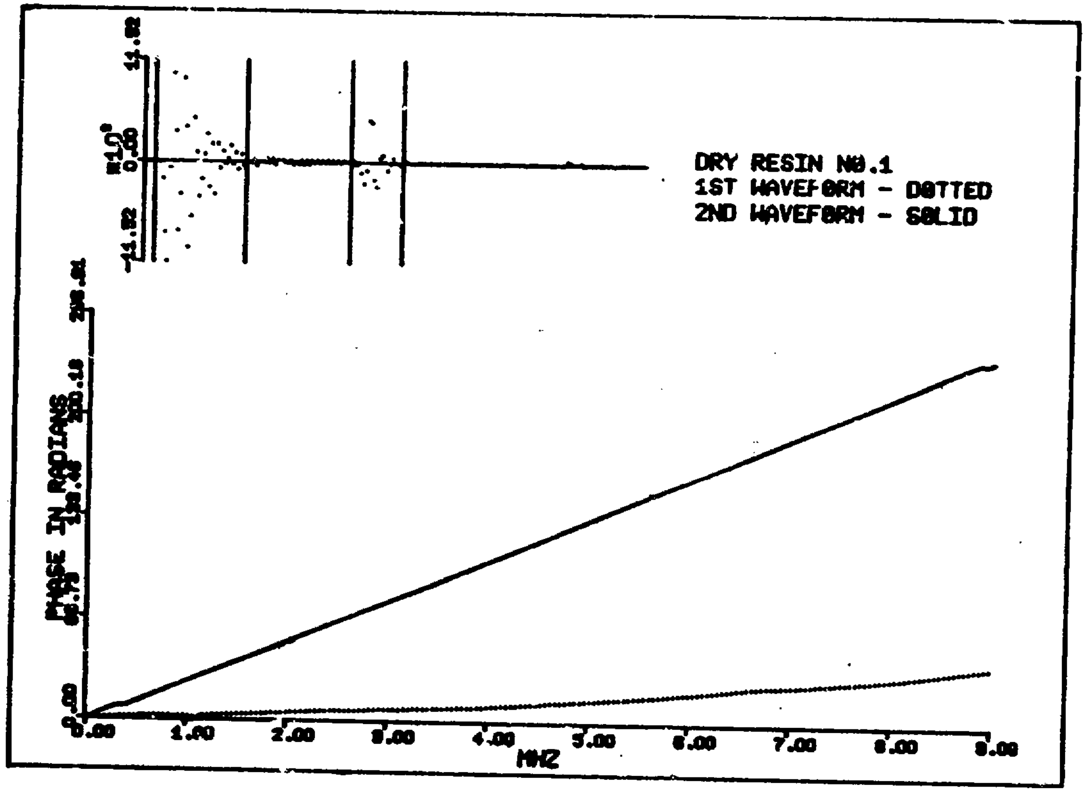

Figure 34. Graphic Output of PHASE Program

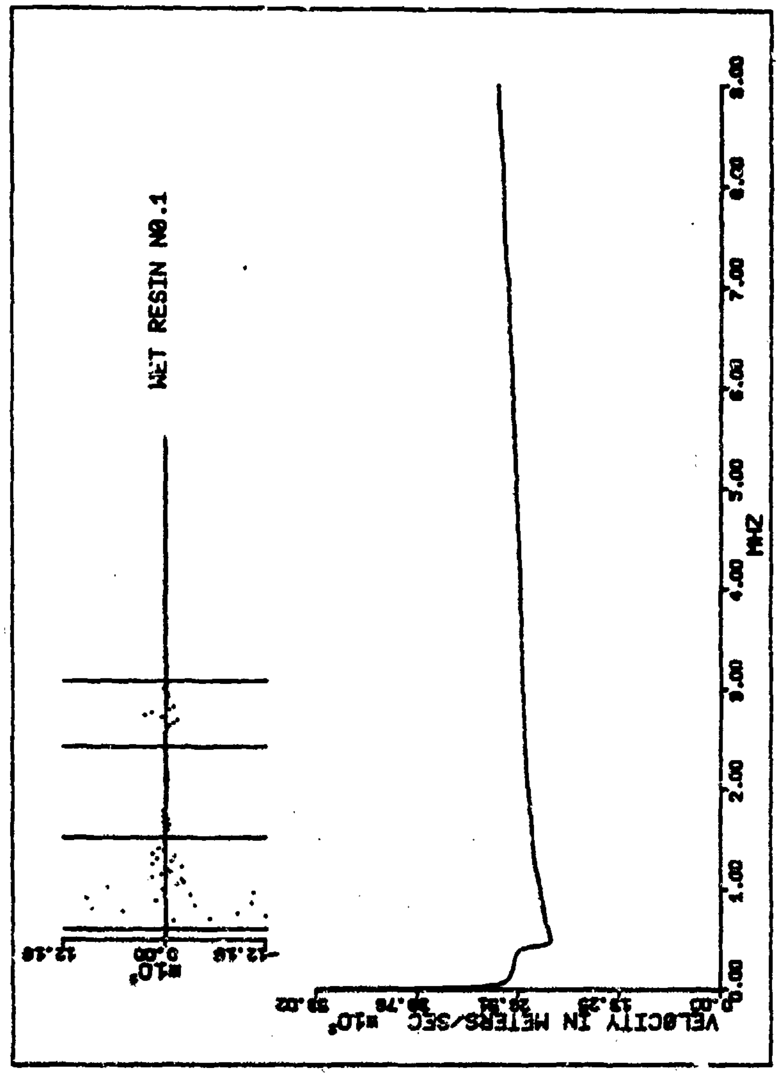

Figure 35. Graphic Output of VELOCITY Program

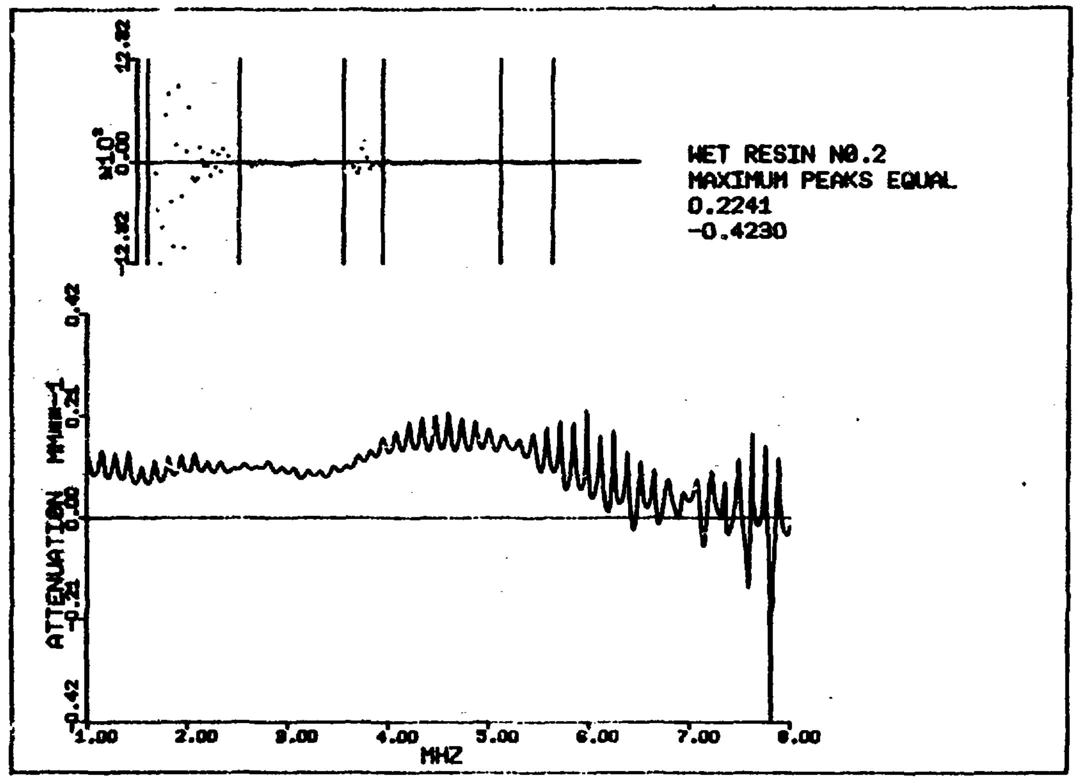

Figure 36. Graphic Output of ATTENUATION Program

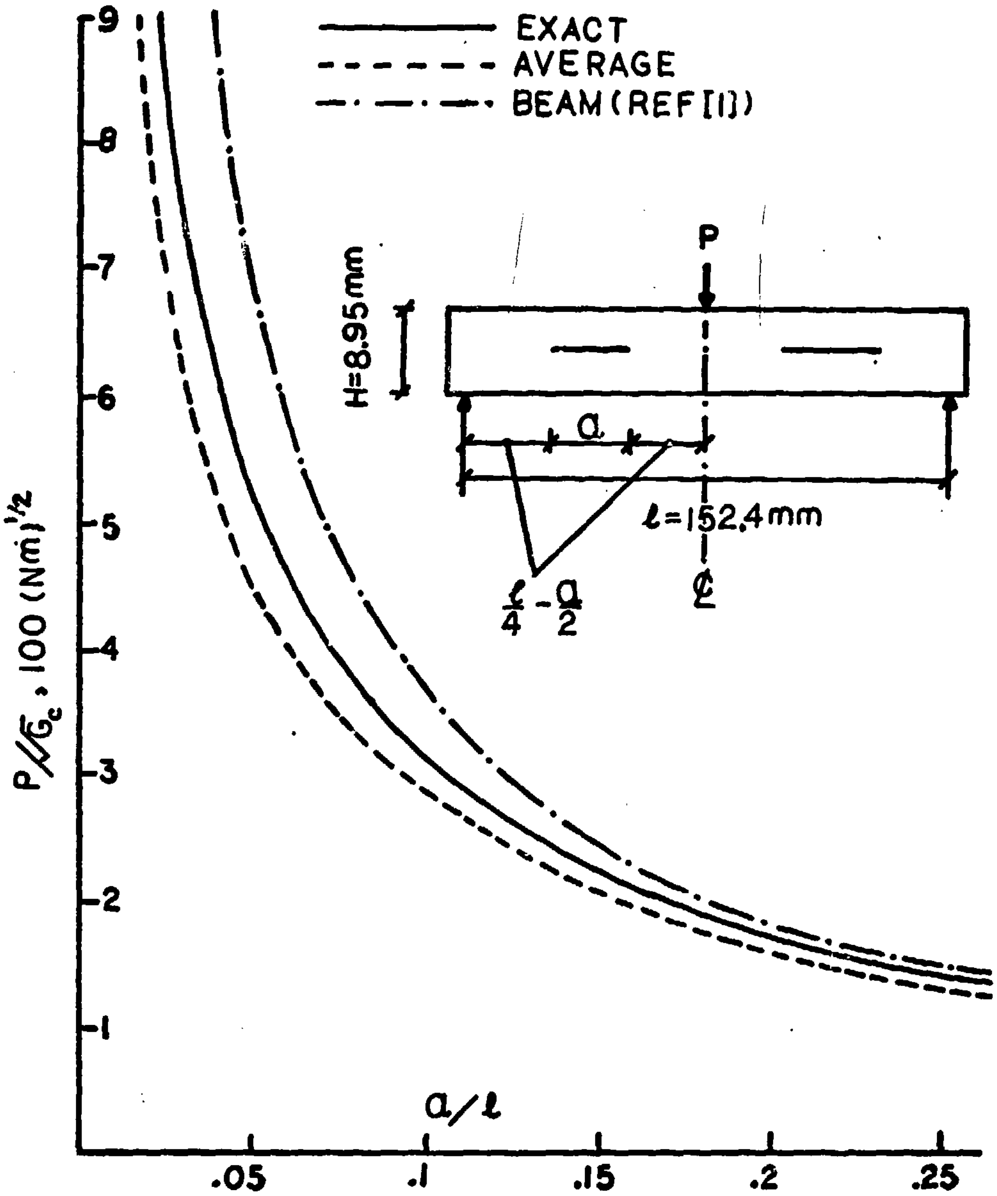

Figure 37. Critical Load for Varying Disbond Length

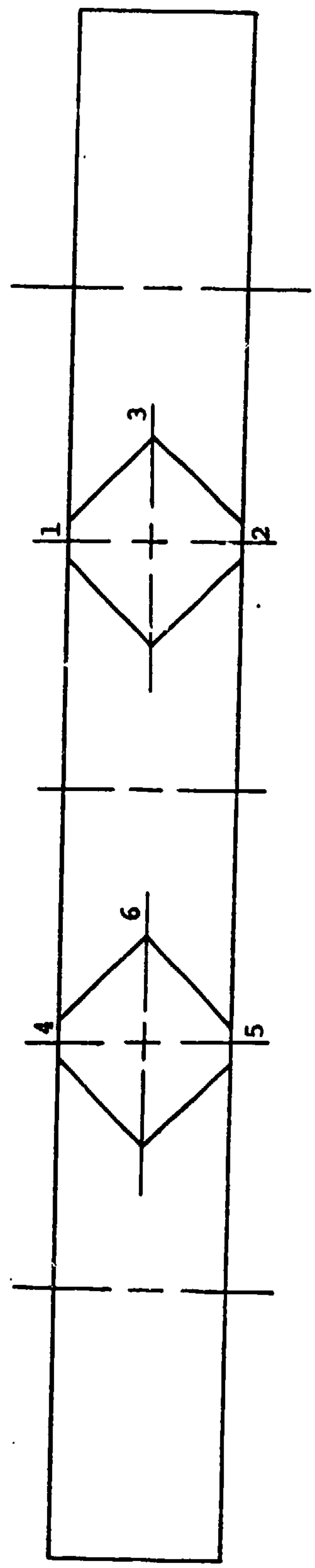

Figure 38. Measuring Locations for Disbond Propagation in Fatigue

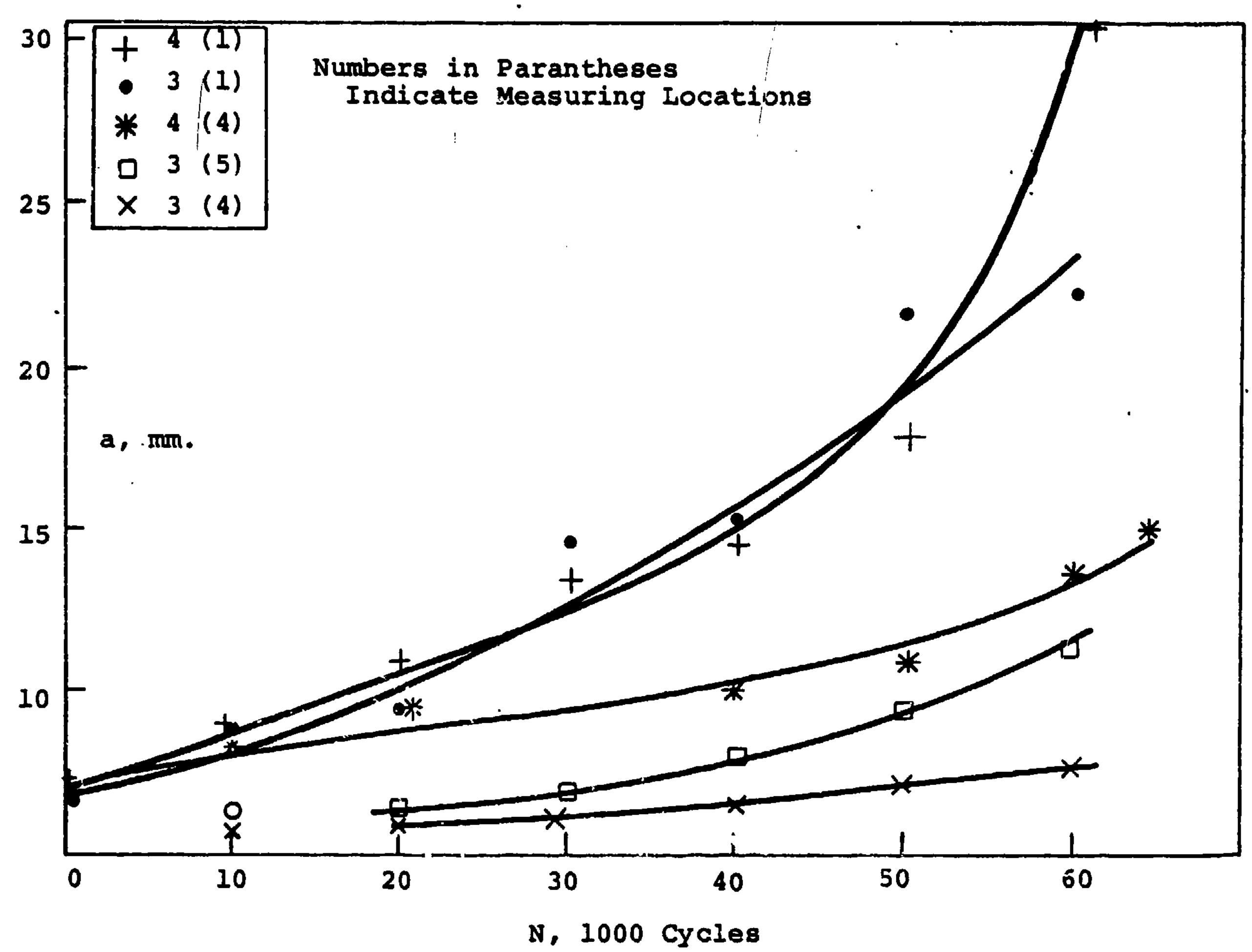

Figure 39. a vs. N for Specimens 0.75-3 and 0.75-4, S=0.5

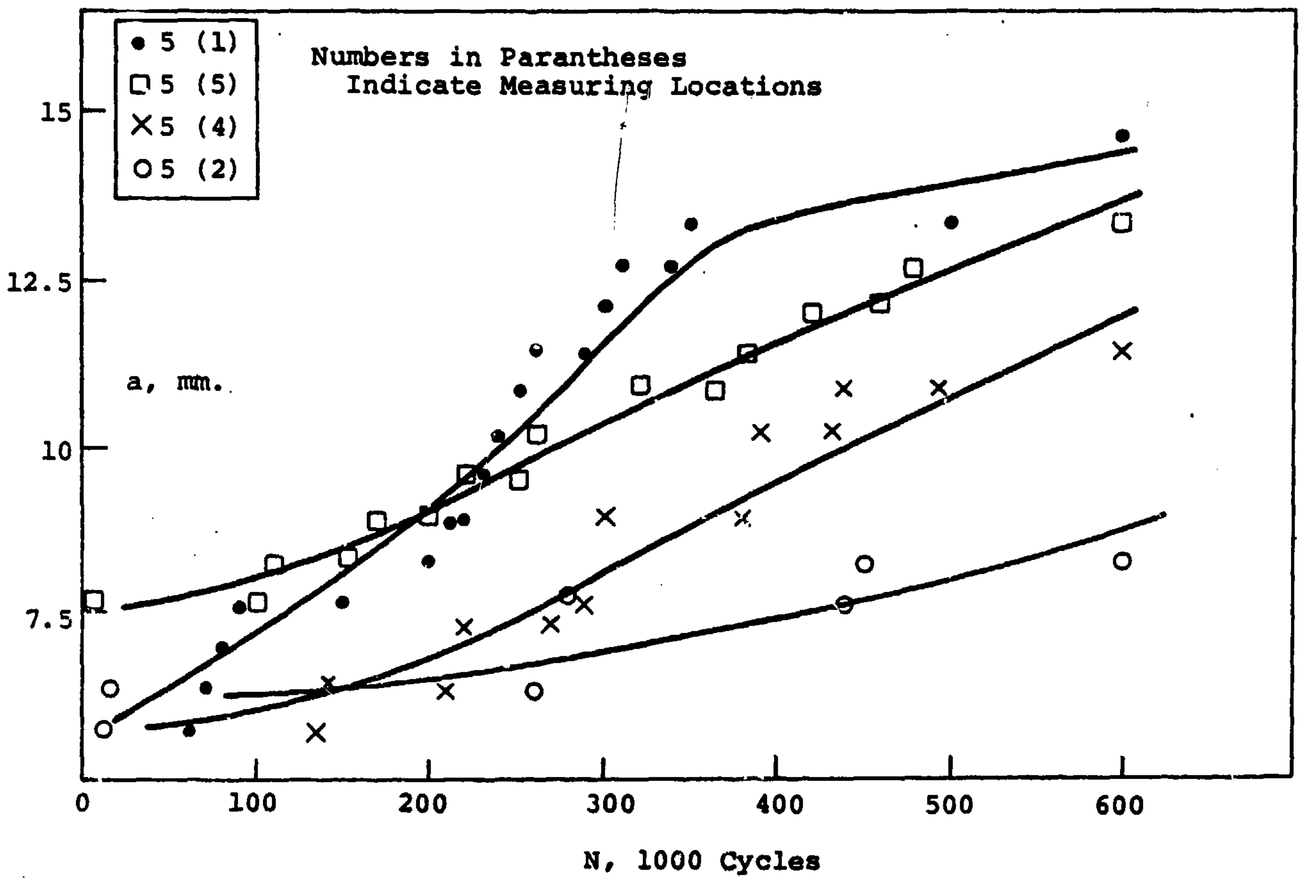

Figure 40. a vs. N for Specimen 0.75-5, S=0.4

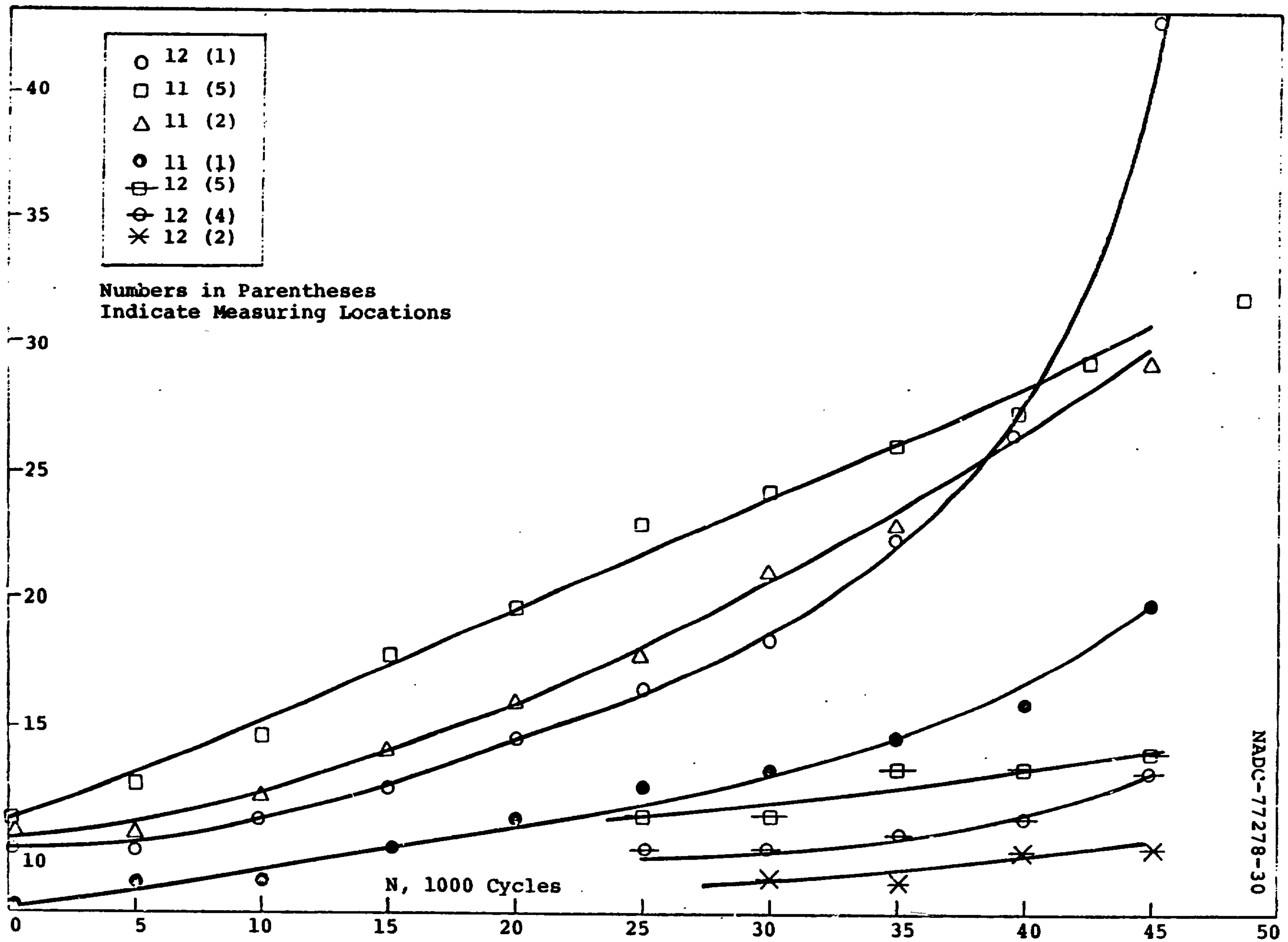

Figure 41. a vs. N for Specimens 1.00-11 and 1.00-12, S=0.5

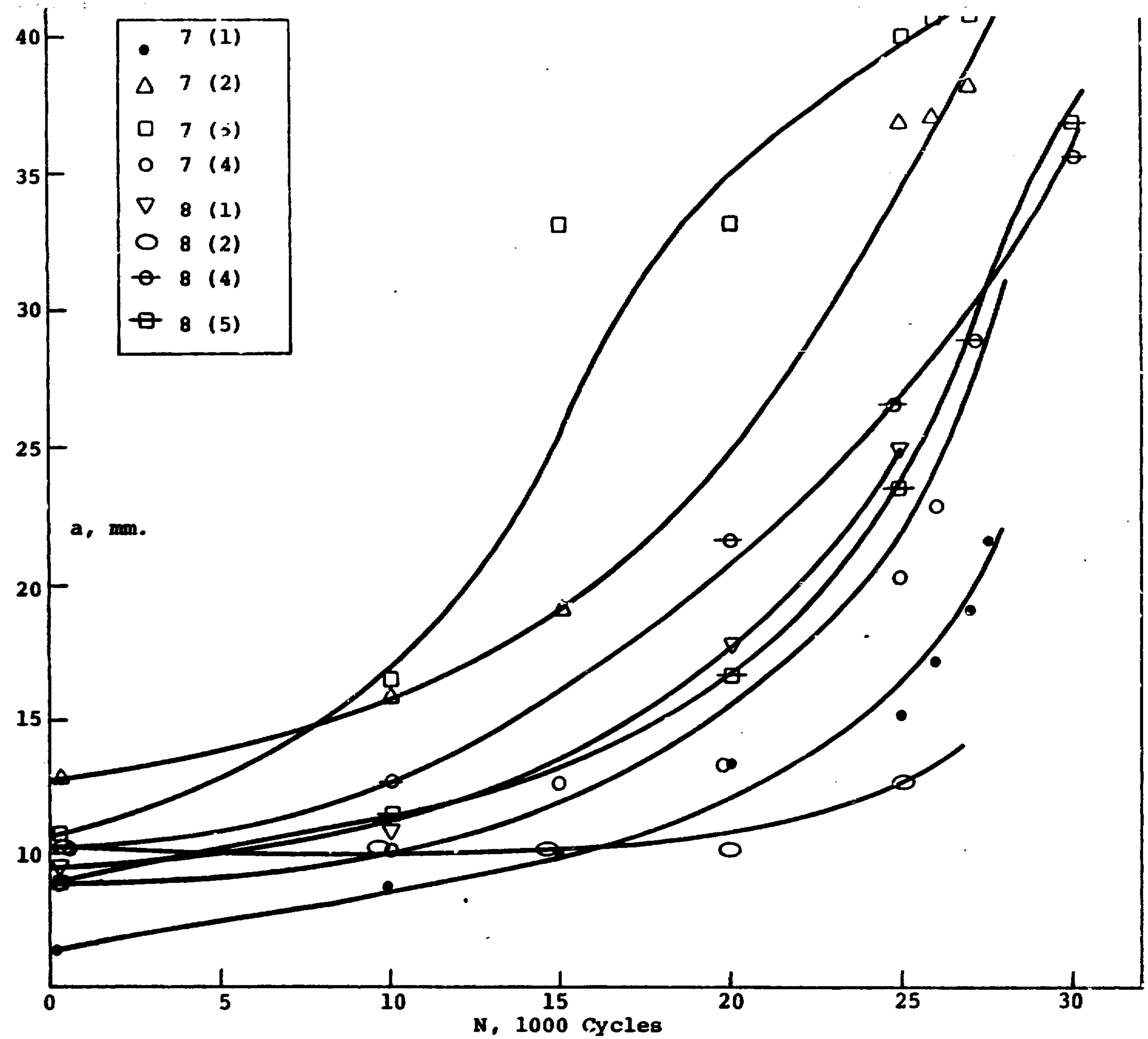

Figure 42. a vs. N for Specimens 1.25-7 and 1.25-8, S=0.5

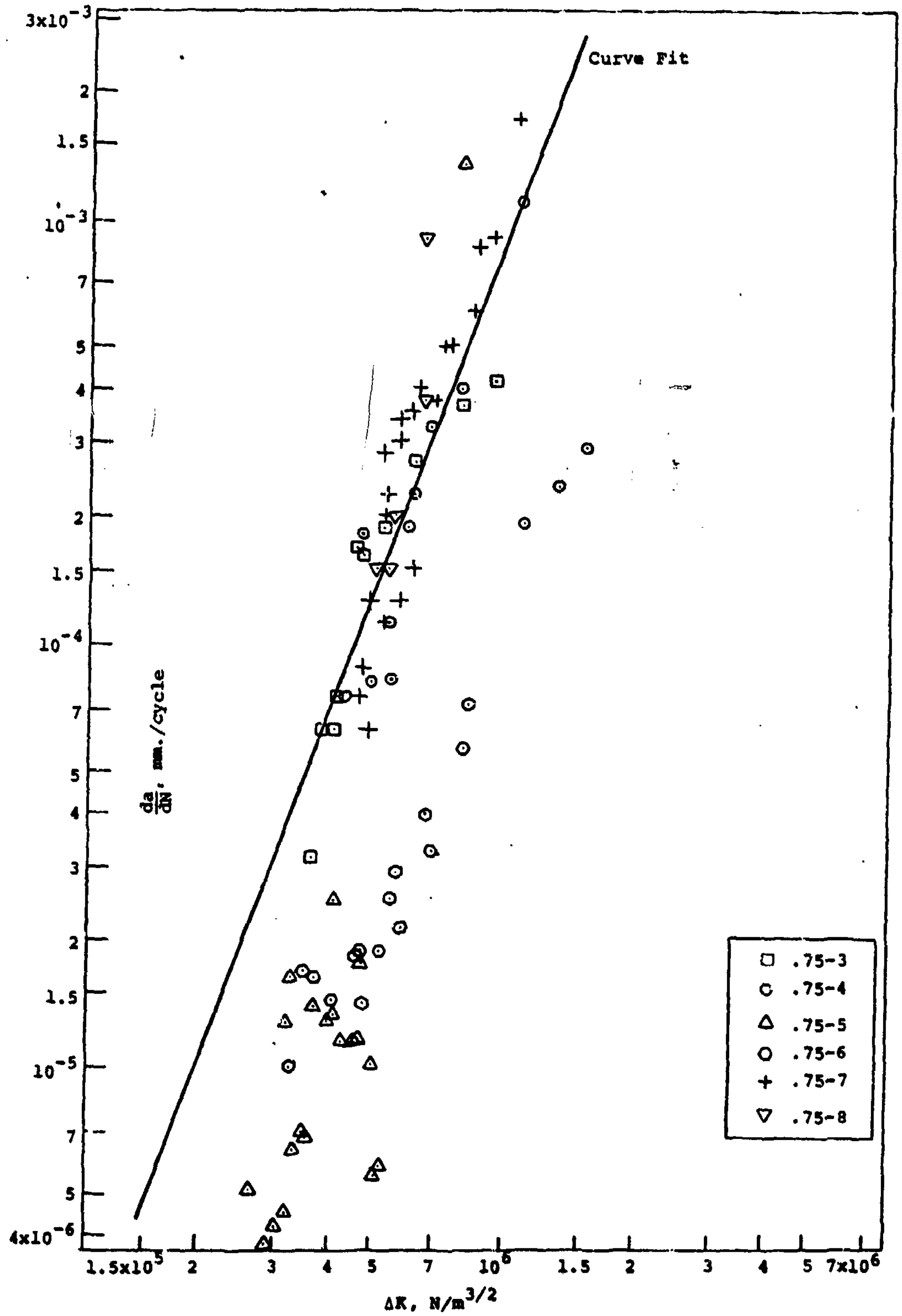

Figure 43. $\frac{da}{dN}$ vs. ΔK for 19.05 mm. (0.75 in.) Defects

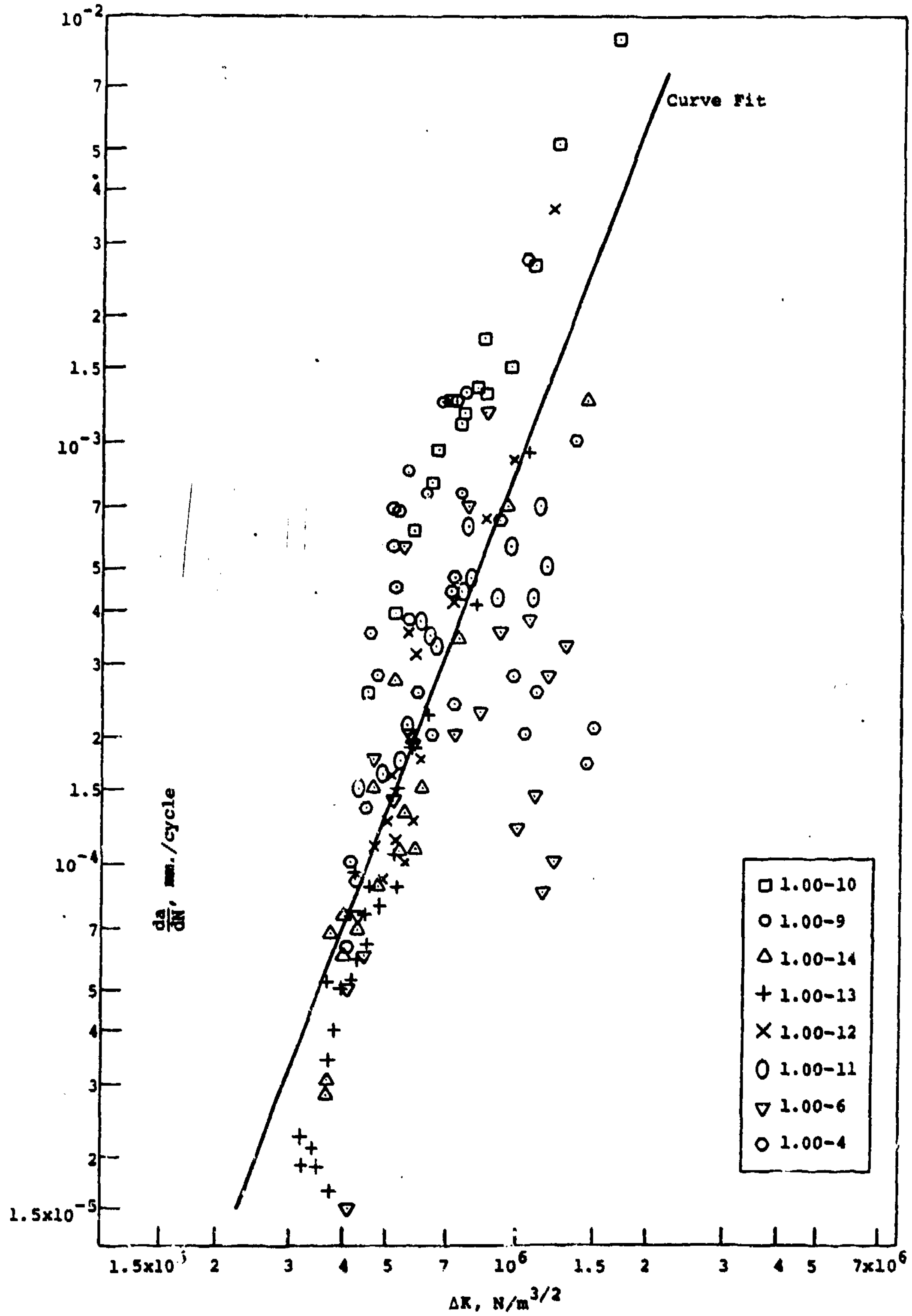

Figure 44. $\frac{da}{dN}$ vs. ΔK for 25.4 mm. (1.00 in.) Defects

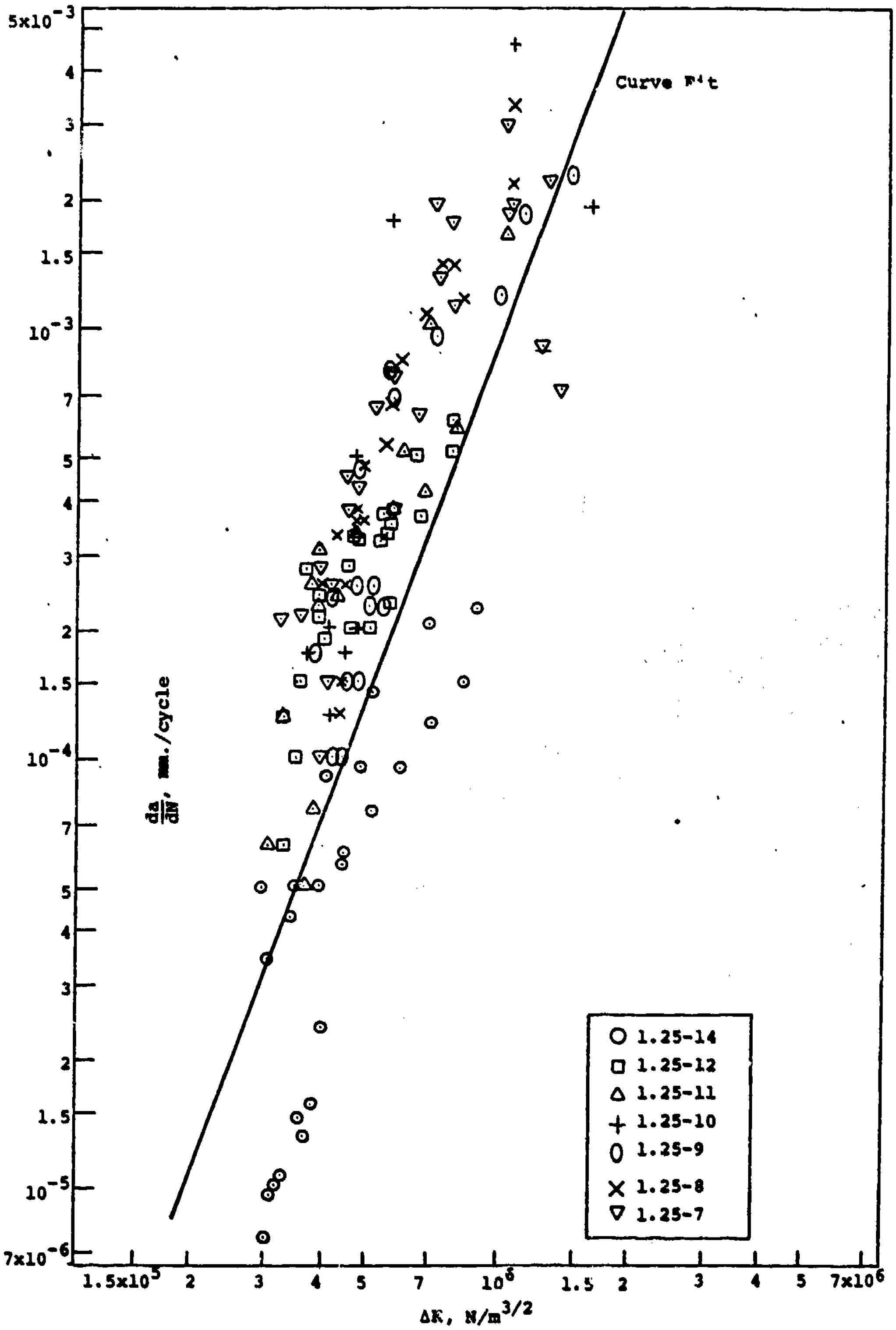

Figure 45. $\frac{da}{dN}$ vs. ΔK for 31.75 mm. (1.25 in.) Defects

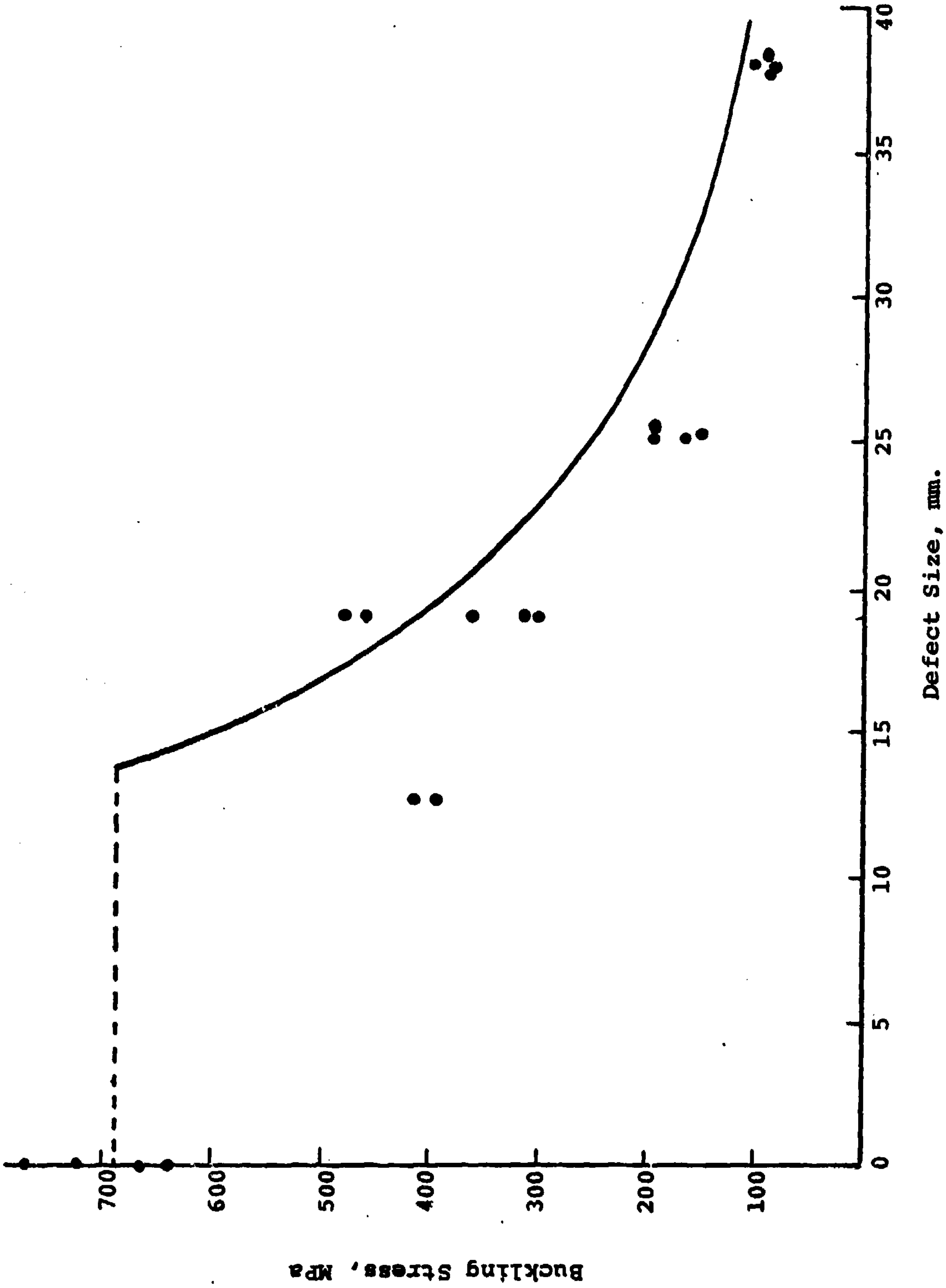

Figure 46. Data Correlation for Buckling Tests

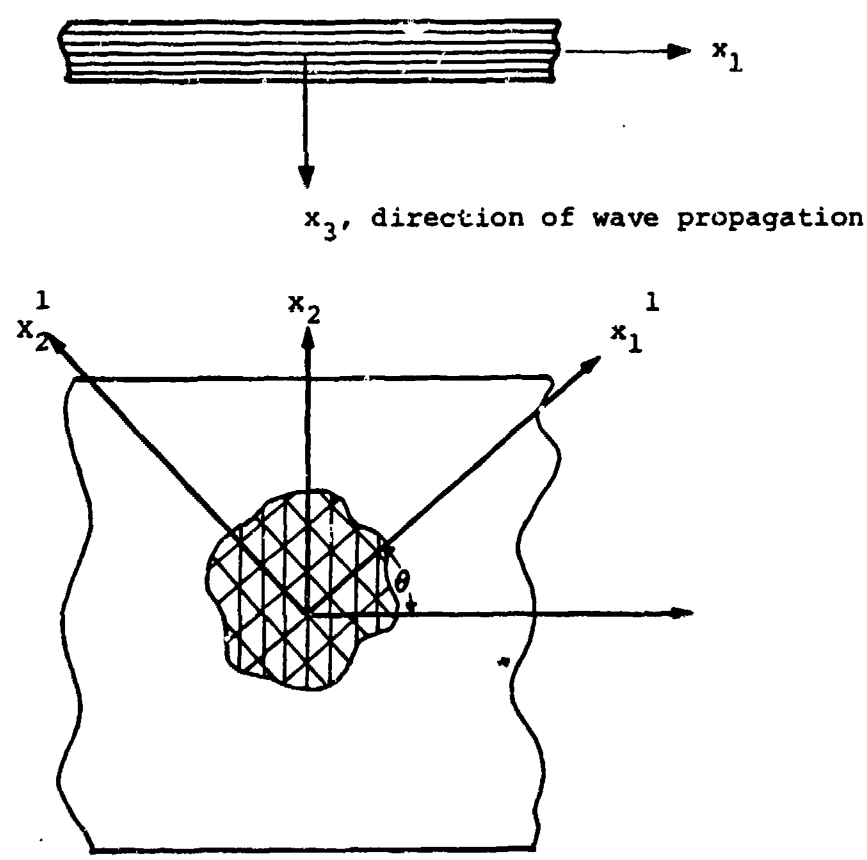

Figure 47. Lamina and Laminate Co-ordinate Systems

APPENDIX A-1. STRESS ANALYSIS OF DELAMINATED BEAM IN SHEAR

SERIES SOLUTION

Consider a laminated beam of span ℓ as shown in Figure 1 under a state of generalized plane stress or plane strain such that the displacements in all layers can be described by two components $U(=u\ell)$ and $W(=w\ell)$. The differential equation in terms of the nondimensionalized displacements u_i and w_i of layer i are as follows:

$$\left(C^i_{55} \frac{\partial^2}{\partial z^2} + \frac{\partial^2}{\partial x^2}\right) u_i + (C^i_{13} + C^i_{55}) \frac{\partial^2 w_i}{\partial x \partial z} = 0$$
$$(C^i_{13} + C^i_{55}) \frac{\partial^2 u_i}{\partial x \partial z} + \left(C^i_{33} \frac{\partial^2}{\partial z^2} + C^i_{55} \frac{\partial^2}{\partial x^2}\right) w_i = 0 \qquad \text{(A-1.1)}$$

where C^i_{jk} are the effective moduli of layer i in the case of plane stress.

Assume solutions of (A-1.1) in the form:

$$u_i = \sum_{m=1}^{\infty} u_{im}(z) \cos m\pi x$$
$$w_i = \sum_{m=1}^{\infty} w_{im}(z) \sin m\pi x \qquad \text{(A-1.2)}$$

Substituting (A-1.2) in (A-1.1) and solving for $u_{im}(z)$ and $w_{im}(z)$, one can express the stresses σ^{im}_{zz} and τ^{im}_{zx}, in layer i corresponding to the mth harmonic, i.e.,

$$\sigma_{zz} = \Sigma\, \sigma^m_{zz} \sin m\pi x$$
$$\tau_{zx} = \Sigma\, \tau^m_{zx} \cos m\pi x \qquad \text{(A-1.3)}$$

in terms the displacement components at interfaces i and i+1. In particular the boundary tractions at $z=\pm h^i/2\,\ell$ can be written as:

$$\frac{1}{m\pi}\begin{bmatrix}\sigma^{m+}\\ \tau^{m+}\\ -\sigma^{m-}\\ -\tau^{m-}\end{bmatrix} = \begin{bmatrix}[A_{11}^{m(i)}] & [A_{12}^{m(i)}]\\ [A_{21}^{m(i)}] & [A_{22}^{m(i)}]\end{bmatrix}\begin{bmatrix}w_{im}\\ u_{im}\\ w_{(i+1)m}\\ u_{i+1)m}\end{bmatrix} \qquad \text{(A-1.4)}$$

where + and - signs indicate values of σ_{zz}^{m} and τ_{zx}^{m} at $z=+h/2$ and $-h/2$, respectively. $A_{\alpha\beta}^{m}(\alpha,\beta=1,2)$ are 2x2 stiffness matrices, each element of which is a complicated function of the layer stiffnesses and its thickness. Detailed expressions for anisotropic layers are given in table A-1-1. Writing the displacement vector $[w_{im},u_{im}]^T$ as $\bar{u}_i^m$ and traction vector $\frac{1}{m\pi}[\sigma^m,\tau^m]^T$ as S^m, one obtains the following equations from boundary and interface conditions for the layered system in terms of the prescribed tractions S_1^m and S_n^m on top and bottom surfaces of the beam and the displacement discontinuity $\bar{u}^{*m}$ at the interface (i+1) containing the disbonds [see equation (A-1.13)]. Note that superscripts (+) and (-) indicate quantities on the top and bottom of interfaces (i+1) respectively.

$$A_{11}^{m(1)}\bar{u}_1 + A_{12}^{m(1)}\bar{u}_2^m = S_1^m \qquad \text{(A-1.5)}$$

$$A_{21}^{m(j-1)}\bar{u}_{j-1}^m + (A_{22}^{m(j-1)} + A_{11}^{m(j)})\bar{u}_j^m + A_{12}^{m(j)}\bar{u}_{j+1}^m = 0;$$

$$j = 2,3. \ . \ . \ .,i-1 \qquad \text{(A-1.6)}$$

$$A_{21}^{m(i-1)}\bar{u}_{i-1}^m + (A_{22}^{m(i-1)} + A_{11}^{m(i)})\bar{u}_i^m + A_{12}^{m(i)}\bar{u}_{i+1}^{m(+)} = 0 \qquad \text{(A-1.7)}$$

$$A_{21}^{m(i)}\bar{u}_i^m + A_{22}^{m(i)}\bar{u}_{i+1}^{m(+)} = S_{i+1}^{m(+)} \qquad \text{(A-1.8)}$$

$$A_{11}^{m(i+1)}\bar{u}_{i+1}^{m(-)} + A_{12}^{m(i+1)}\ \bar{u}_{i+2}^m = S_{i+1}^{m(-)} \qquad \text{(A-1.9)}$$

$$A_{21}^{m(i+1)}\bar{u}_{i+1}^{m(-)} + (A_{22}^{m(i+1)} + A_{11}^{m(i+2)})\bar{u}_{i+2}^{m} + A_{12}^{m(i+2)}\bar{u}_{i+3}^{m} = 0 \quad \text{(A-1.10)}$$

$$A_{21}^{m(k-1)}\bar{u}_{k-1}^{m} + (A_{22}^{m(k-1)} + A_{11}^{m(k)})\bar{u}_{k}^{m} + A_{12}^{m(k)}\bar{u}_{k+1}^{m} = 0;$$

$$k = i+3, \ \ldots, \ n-1 \quad \text{(A-1.11)}$$

$$A_{21}^{m(n-1)}\bar{u}_{n-1}^{m} + A_{22}^{m(n-1)}\bar{u}_{n}^{m} = S_{n}^{m} \quad \text{(A-1.12)}$$

Also,

$$\bar{u}_{i+1}^{m(+)} - \bar{u}_{i+1}^{m(-)} = \bar{u}^{*m} \quad \text{(A-1.13)}$$

and

$$S_{i+1}^{m(+)} + S_{i+1}^{m(-)} = 0 \quad \text{(A-1.14)}$$

Adding (A-1.8), (A-1.9) and (A-1.14) one has:

$$A_{21}^{m(i)}\bar{u}_{i}^{m} + A_{22}^{m(i)}\bar{u}_{i+1}^{m(+)} + A_{11}^{m(i+1)}\bar{u}_{i+1}^{m(-)} + A_{12}^{m(i+1)}\bar{u}_{i+2}^{m} = 0 \quad \text{(A-1.15)}$$

Let as

$$m \to \infty \qquad \begin{aligned} \bar{u}_{i+1}^{m(+)} &\to \bar{u}_{o}^{(+)m} \\ \bar{u}_{i+1}^{m(-)} &\to \bar{u}_{o}^{(-)m} \end{aligned} \quad \text{(A-1.16)}$$

The matrices $A_{\alpha\beta}^{m(i)}$ have the properties:

$$A_{22}^{m(i)} \rightarrow A_{22}^{(i)*} \qquad A_{11}^{m(i+1)} \rightarrow A_{11}^{(i+1)*}$$

$$A_{21}^{m(i)} \rightarrow [0] \qquad A_{12}^{m(i+1)} \rightarrow [0]$$

as m approaches ∞.

From (A-1.13), (A-1.15) and (A-1.16) one has:

$$A_{22}^{(i)*}\ \bar{u}_o^{(+)m} + A_{11}^{(i+1)*}\ \bar{u}_o^{(-)m} = 0$$

$$\bar{u}_o^{(+)m} - \bar{u}_o^{(-)m} = \bar{u}^{*m} \qquad \text{(A-1.17)}$$

The solution of (A-1.17) can be written as:

$$u_o^{(+)m} = [B_1]\bar{u}^{*m}$$

$$u_o^{(-)m} = [B_2]\bar{u}^{*m} \qquad \text{(A-1.18)}$$

Writing:

$$\bar{u}_{i+1}^{m(+)} = \bar{u}_{i+1}^{m} + B_1\bar{u}_m^{*}$$

$$\bar{u}_{i+1}^{m(-)} = \bar{u}_{i+1}^{m} + B_2\bar{u}_m^{*} \qquad \text{(A-1.19)}$$

which satisfy (A-1.13) and reduce the system (A-1.5-7), (A-1.15) and (A-1.10-12) to:

$$[K_m] \begin{bmatrix} \bar{u}_1^m \\ \cdot \\ \cdot \\ \cdot \\ \bar{u}_i^m \\ \bar{u}_{i+1}^m \\ \bar{u}_{i+2}^m \\ \cdot \\ \cdot \\ \cdot \\ \bar{u}_n^m \end{bmatrix} = \begin{bmatrix} S_1^m \\ 0 \\ -A_{12}^{m(i)} B_1 \bar{u}^{*m} \\ -(\bar{A}_{22}^{m(i)} B_1 + \bar{A}_{11}^{m(i+1)} B_2)\bar{u}^{*m} \\ -A_{21}^{m(i+1)} B_2 \bar{u}^{*m} \\ 0 \\ S_n^m \end{bmatrix} \qquad \text{(A-1.20)}$$

where $[K_m]$ is the global stiffness matrix for the laminate and:

$$\bar{A}_{\alpha\alpha}^{m(k)} = A_{\alpha\alpha}^{m(k)} - A_{\alpha\alpha}^{(k)*}; \ \alpha=1,2 \text{ and } k=i,\ i+1 \qquad \text{(A-1.21)}$$

One should note that $[\bar{A}_{\alpha\alpha}^{m(k)}]$ as well as $[A_{\alpha\beta}^{m(k)}]$ $(\alpha\neq\beta)$ approach [0] as m is increased.

REDUCTION TO A SET OF INTEGRAL EQUATIONS

Now we introduce two unknown functions such that the displacement discontinuities at interface (i+1) are given by:

$$u_{i+1}^{(+)}(x) - u_{i+1}^{(-)}(x) = 0 \qquad ; \; 0 \leq x \leq c, \; d \leq x \leq 1/2$$
$$= -\frac{1}{4}\int_c^x \theta_2(x)dx; \; c \leq x \leq d$$

$$w_{i+1}^{(+)}(x) - w_{i+1}^{(-)}(x) = 0 \qquad ; \; 0 \leq x \leq c, \; d \leq x \leq 1/2$$
$$= -\frac{1}{4}\int_c^x \theta_1(x)dx; \; c \leq x \leq d \qquad \text{(A-1.22a)}$$

such that:

$$\int_c^d \theta_i(x)dx = 0; \quad i=1,2 \qquad \text{(A-1.22b)}$$

and

$$u(1-x) = -u(x); \; 0 \leq x \leq 1/2$$
$$\text{and } w(1-x) = w(x) \qquad \text{(A-1.23)}$$

Equation (A-1.23) applies to a structure loaded symmetrically about the center line x=1/2. Using (A-1.23) and (A-1.22) $\bar{u}^{*m}$ in equation (A-1.13) can be expressed as:

$$\bar{u}^{*m} = \begin{bmatrix} w^{*m} \\ \\ u^{*m} \end{bmatrix} = \frac{1}{m\pi} \begin{bmatrix} \int_c^d \theta_1(y) \cos m\pi y \, dy \\ \\ \int_c^d \theta_2(y) \sin m\pi y \, dy \end{bmatrix} \qquad \text{(A-1.24)}$$

Solving for displacement components $\bar{u}_j^m$ (j=1,n), substituting their values as well as (A-1.19) and (A-1.24) in (A-1.8) and summing the resulting expressions for $S_{i+1}^{m(+)}$ from m=1,3..∞, one can express the stress free conditions on top surfaces of the disbond in terms of a set of coupled pair of integral equations.

$$\frac{1}{\pi}\int_c^d \frac{\theta_1(y)}{y-x}\,dy - \frac{H_{12}^o}{H_{11}^o}\,\theta_2(x) + \sum_{j=1}^{2}\int_c^d K_{1j}'(x,y)\,\theta_j(y)\,dy = P_1(x)$$

(A-1.25a)

$$\frac{1}{\pi}\int_c^d \frac{\theta_2(y)}{y-x}\,dy + \frac{H_{12}^o}{H_{22}^o}\,\theta_1(x) + \sum_{j=1}^{2}\int_c^d K_{2j}'(x,y)\,\theta_j(y)\,dy = P_2(x)$$

$$K_{11}' = -\frac{1}{\pi}\left[\frac{1}{x+y} + 2\int_o^\infty e^{-s/2}\,\mathrm{sech}\,s/2\,\cosh sy\,\sinh sx\,ds\right] - \frac{4}{H_{11}^o}\sum H_{11}^m \sin m\pi x\cos m\pi y$$

$$K_{12}' = -\frac{4}{H_{11}^o}\sum H_{12}^m \sin m\pi x\sin m\pi y$$

$$K_{21}' = \frac{4}{H_{22}^o}\sum H_{21}^m \cos m\pi x\cos m\pi y$$

$$K_{22}' = \frac{1}{\pi}\left[\frac{1}{x+y} + 2\int_o^\infty e^{-s/2}\,\mathrm{sech}\,s/2\,\sinh sy\,\cosh sx\,ds\right] + \frac{4}{H_{22}^o}\sum H_{22}^m \cos m\pi x\sin m\pi y \qquad \text{(A-1.25b)}$$

$$P_1 = \frac{4}{H_{11}^o}\sum P_{1m}\sin m\pi x\ ,\quad P_2 = \frac{4}{H_{22}^o}\sum P_{22}^m \cos m\pi x$$

The constants H_{11}^{o}, H_{22}^{o}, H_{12}^{o}, $H_{\alpha\beta}^{m}(\alpha,\beta=1,2)$ and P_{1m} and P_{2m} are known and the summation sign indicates sum over $m=1,3,\ldots\infty$. One should note that use has been made of some well known identities (ref. 18) to obtain Equations (A-1.25a,b). In (A-1.25) $K'_{ij}(x,y)$ are the regular kernels and Cauchy kernels appear in the first terms. These types of equations have been considered in reference 19. By the substitutions given below:

$$x = a_1 t + a_2$$

$$y = a_1 \tau + a_2$$

$$a_1 = (d-c)/2$$

$$a_2 = (d+c)/2$$

$$\theta_i(\tau) = \theta_i(y), \; P_i(t) = P_i(x)$$

Equations (A-1.25) can be reduced to:

$$\frac{1}{\pi}\int_{-1}^{1} \frac{\theta_1(\tau)}{\tau - t}\, d\tau - \frac{H_{12}^{o}}{H_{11}^{o}}\, \theta_2(\tau) + \sum_{j=1}^{2} \int_{-1}^{1} K'_{1j}(t,\tau)\theta_j(\tau)d\tau = P_1(t)$$

$$\frac{1}{\pi}\int_{-1}^{1} \frac{\theta_2(\tau)}{\tau - t}\, d\tau - \frac{H_{12}^{o}}{H_{22}^{o}}\, \theta_1(\tau) + \sum_{j=1}^{2} \int_{-1}^{1} K'_{2j}(t,\tau)\theta_j(\tau)d\tau = P_2(t) \quad \text{(A-1.26)}$$

Following methods given in reference 20, one can study the singular nature of functions θ_1 and θ_2 as $t \to \pm 1$. When the properties of layers i and (i+1) are identical $H_{12}^{o}=0$ and consideration of Cuchy kernels yields the well known square root type of singularity. When $H_{12}^{o} \neq 0$ the index of the singularity is of the type $-1/2 \pm i\varepsilon$, which is the characteristic stress singularity at the tip of a crack between two dissimilar materials.

The system of Equations (A-1.26) and (A-1.22b) must be solved numerically and the suitable methods of solution are different for the cases (i) $H_{12}^{o}=0$ and (ii) $H_{12}^{o}\neq 0$. In this study we will

consider $H^{o}_{12}=0$ and employ the colocation method outlined in reference 19 to reduce the equations to a system of algebraic equations for determining the functions $\phi_i(\tau)$, i=1,2 defined by:

$$\theta_i(\tau) = (1-\tau^2)^{-1/2}\ \phi_i(\tau). \quad i=1,2 \tag{A-1.27}$$

By solving the set of equations for $\phi_i(\tau)$ at points $\tau_k=\cos\frac{\pi(2k-1)}{2n}$; (k=1,2...n) can be evaluated. The number n denotes the number of collocation points used for discretizing the system. The stress intensity factors at x=c and d corresponding mode I and II are given by:

$$\begin{aligned}
K_{Id} &= -H^{o}_{11}\ \sqrt{d-c}\quad \phi_1\ (1)/4\sqrt{2}\\
K_{Ic} &= H^{o}_{11}\ \sqrt{d-c}\quad \phi_1\ (-1)/4\sqrt{2}\\
K_{IId} &= H^{o}_{22}\ \sqrt{d-c}\quad \phi_2\ (1)/4\sqrt{2}\\
K_{IIc} &= -H^{o}_{22}\ \sqrt{d-c}\quad \phi_2\ (-1)/4\sqrt{2}
\end{aligned} \tag{A-1.28}$$

and the strain energy release rate can be shown to be:

$$G = \frac{\pi}{2}\left[\frac{K^2_I}{H^{o}_{11}} + \frac{K^2_{II}}{H^{o}_{22}}\right] \tag{A-1.29}$$

TABLE A-1-1
STIFFNESS MATRIX FOR A LAYER

Let $A = C_{55}\ C_{33}$

$B = (C_{13} + C_{55})^2 - C_{11}\ C_{33} - C_{55}^2$

$C = C_{11}\ C_{55}$

$D = B^2 - 4AC$

For the type of anisotropic layers considered $B<0$ and $D>0$.

The stiffness matrix for harmonic m,

$$[K] = \begin{bmatrix} A_{11} & A_{12} \\ A_{21} & A_{22} \end{bmatrix}$$

is given by:

$$k_{11} = 2(b_1-b_2)(a_1 \coth p_m\alpha_1 h - a_2 \coth p_m\alpha_2 h)/\Delta_m^*$$

$$k_{12} = [2(d_1a_1+d_2a_2)-2(d_1a_2+d_2a_1)\bar{\Lambda}_m]/\Delta_m^*$$

$$k_{13} = 2(b_1-b_2)(-a_1 \operatorname{cosech} p_m\alpha_1 h+a_2 \operatorname{cosech} p_m\alpha_2 h)/\Delta_m^*$$

$$k_{14} = 2(d_2a_1-d_1a_2)\tfrac{1}{2}(\tanh p_m\alpha_1 h/2 \coth p_m\alpha_2 h/2 - \coth p_m\alpha_1 h/2 \tanh p_m\alpha_2 h/2)/\Delta_m^*$$

$$k_{22} = 2(d_2a_1-d_1a_2)(a_1 \coth p_m\alpha_2 h-a_2 \coth p_m\alpha_1 h)/\Delta_m^*$$

$$k_{24} = 2(d_2a_1-d_1a_2)(-a_1 \operatorname{cosech} p_m\alpha_2 h+a_2 \operatorname{cosech} p_m\alpha_1 h)/\Delta_m^*$$

$$k_{33} = k_{11}$$

$$k_{21} = k_{12}$$

TABLE A-1-1 (Continued)

$k_{34} = k_{43} = -k_{12}$

$k_{41} = k_{14}$

$k_{23} = k_{32} = -k_{14}$

$k_{31} = k_{13}$

$k_{42} = k_{24}$

$k_{44} = k_{22}$

Where $p_m = m\pi$

$$\bar{\Delta}_m = \frac{1}{2}\left[\tanh(p_m\alpha_1 h/_2)\ \coth\ (p_m\alpha_2 h/_2) + \mathrm{Coth}(p_m\alpha_1 h/_2)\tanh\ (p_m\alpha_2 h/_2)\right]$$

$$\Delta_m^* = 2(a_1^2 + a_2^2 - 2a_1 a_2 \bar{\Delta}_m)$$

$$\alpha_1 = \{(-B + \sqrt{D})/2A\}^{1/2}$$

$$\alpha_2 = \{(-B - \sqrt{D})/2A\}^{1/2}$$

$$a_i = (-C_{55}\alpha_i^2 + C_{11})/(C_{13} + C_{55})\alpha_i$$

$$b_i = C_{33}a_i\alpha_i - C_{13}$$

$$d_i = C_{55}(\alpha_i + a_i)$$

$$e_i = C_{13}a_i\alpha_i - C_{11}$$

If $D \leq 0$ different expressions for the elements k_{ij} hold.

APPENDIX A-2. FORMULATION OF THE BUCKLING PROBLEM

For the beams 1, 2 and 3 (i=1,2,3) define the following nondimensional quantities.

Coordinate $x^{(i)} = X^{(i)}/\ell$		
Thickness $H^{(i)} = h^{(i)}/2\ell$		
Midplane displacement in x-direction	$U^{(i)} = u_0^{(i)}/\ell$	
Beam deflection in z-direction	$W^{(i)} = w^{(i)}/\ell$	
Bending rotation	$\psi^{(i)}$	
Bending stiffness	$d^{(i)} = D_{11}^{(i)}/D_{11}^{(1)}$	
Axial extensional stiffness	$a^{(i)} = A_{11}^{(i)}\ell^2/D_{11}^{(1)}$	(A-2.1)
Coupling stiffness (extension-bending)	$b^{(i)} = B_{11}^{(i)}\ell/D_{11}^{(1)}$	
Shear stiffness (effective)	$k^{(i)} = k_{55}C_{55}^{*(i)}\ell^2/D_{11}^{(1)}$	
Foundation modulus in shear	$s^{(i)} = S^{(i)}\ell^4/D_{11}^{(1)}$	
Foundation modulus in extension	$t^{(i)} = T^{(i)}\ell^4/D_{11}^{(1)}$	
Axial Force	$\beta^{(i)}n^* = \beta^{(i)}N_x^{*(1)}\ell^2/D_{11}^{(1)}$	

$N_x^{*(1)}$ is the axial force in beam 1. For beam 1 foundation moduli are zero. Governing differential equations in nondimensional form for the laminated beams are obtained from laminated plate theory including effects of shear deformation, i.e.:

$$a^{(i)}U^{(i)}_{,xx} + b^{(i)}\psi^{(i)}_{,xx} - s^{(i)}(U^{(i)}-\psi^{(i)}H^{(i)}) = 0$$

$$b^{(i)}U^{(i)}_{,xx} + d^{(i)}\psi^{(i)}_{,xx} - k^{(i)}(\psi^{(i)} + W^{(i)}_{,x}) + s^{(i)}H^{(i)}(U^{(i)}-\psi^{(i)}H^{(i)}) = 0$$

$$k^{(i)}(\psi^{(i)}_{,x}+W^{(i)}_{,xx}) - t^{(i)}W^{(i)} - \beta^{(i)}n^*W_{,xx} = 0 \qquad \text{(A-2.2)}$$

Stiffness Matrix for Beam 1

For beam 1, $s^{(1)} = t^{(1)} = 0$ and the nonzero characteristic roots of (A-2.2) are given by:

$$\lambda = \pm i\lambda_0 \tag{A-2.3}$$

where $\lambda_0 = \sqrt{\dfrac{ak\beta n}{(ad-b^2)(k-\beta n^*)}}$

Superscript (1) has been omitted in equation (A-2.3) and such superscripts will be omitted except where necessary. Considering the deformation patterns which are symmetric about $x^{(1)} = x^{(1)} = 0$, the nondimensionalized stress resultants at $x^{(1)} = 1/2$ are related to the displacements at that point in terms of the stiffness matrix $[K^{(1)}]$, i.e.

$$\begin{bmatrix} n_x \\ m_x \\ q'_x \end{bmatrix}_{x=1/2} = [K^{(1)}] \begin{bmatrix} U \\ \psi \\ W \end{bmatrix}_{x=1/2} \tag{A-2.4}$$

where n_x, m_x are the axial force and bending moment, respectively, and $q'_x = q_x - \beta n^* \frac{dw}{dx}$, q_x being the shear force. $K^{(1)}$ is given by:

$$[K^{(1)}] = \begin{bmatrix} 2a & 0 & 0 \\ 2b & 2b^2/a + (d-b^2/a)\lambda_0 \cot \lambda_0/2 & 0 \\ 0 & 0 & 0 \end{bmatrix} \tag{A-2.5}$$

Characteristic Equations for Beams 2 and 3

Characteristic roots λ for equation (A-2.2) are the solutions of:

$$\lambda^6[(k-\beta n^*)(ad-b^2)]$$

$$+ \lambda^4[ak^2-t(ad-b^2) - (k-\beta n^*)\{a(k+sH^2) + sd + 2bsH\}] \quad \text{(A-2.6)}$$

$$+ \lambda^2[t\{a(k+sH^2) + sd + 2bsH\} - \beta n^* sk] - skt = 0$$

Once again the superscript i is omitted in equation (A-2.6) for beams with geometry and stiffnesses under consideration λ^2 has three solutions, i.e. :

(i) one real positive root, λ_1^2

(ii) two complex roots, one conjugate of the other,

$$\lambda_{2,3}^2 = (\alpha_1^2-\alpha_2^2) \pm 2i\,\alpha_1\alpha_2 \quad \text{(A-2.7)}$$

Stiffness Matrix for Beam 2

For beam 2 we consider deformation patterns symmetric about $x^{(2)}= 0$, and introducing three integration constants, E_1, E_2, E_3 $(=\bar{E})$, the displacements $[\bar{U}] = [U,\psi,W]_{x^{(2)} = 1/2}$ and stress resultants $[\bar{N}] = [n_x, m_x q_x^1]_{x^{(2)} = 1/2}$ are expressed as :

$$[\bar{U}] = [F][\bar{E}]$$
$$[\bar{N}] = [G][\bar{E}] \quad \text{(A-2.8)}$$

Matrices F and G are given by :

$$F = \begin{bmatrix} e_0 \sinh \lambda_1/2 & (e_1p_1-e_2p_2) & e_2p_1+e_1p_2 \\ \sinh \lambda_1/2 & p_1 & p_2 \\ f_0\lambda_1 \cosh \lambda_1/2 & (f_1\alpha_1r_1-f_2\alpha_2r_2) & (f_2\alpha_2r_1+f_1\alpha_1r_2) \end{bmatrix} \tag{A-2.9}$$

$$G = \begin{bmatrix} n_0 \cosh \lambda_1/2 & (n_1r_1-n_2r_2) & (n_2r_1+n_1r_2) \\ m_0 \cosh \lambda_1/2 & (m_1r_1-m_2r_2) & (m_2r_1+m_1r_2) \\ q_0 \sinh \lambda_1/2 & (q_1p_1-q_2p_2) & (q_2p_1+q_1p_2) \end{bmatrix} \tag{A-2.10}$$

where λ_1 is the positive root of λ_1^2 and α_1 and α_2 are positive.

Also, $e_0 = -(b\lambda_1^2+sH)/(a\lambda_1^2-s)$

$f_0 = -k/\{(k-\beta n^*)\lambda_1^2 - t\}$

$n_0 = (ae_0+b)\lambda_1$

$m_0 = (be_0+d)\lambda_1$

$q_0 = tf$

$e_1 = -[\{b(\alpha_1^2-\alpha_2^2) + sH\}\{a(\alpha_1^2-\alpha_2^2) - s\} + 4ab\ \alpha_1^2\alpha_2^2]/\Delta_1$

$e_2 = 2\alpha_1\alpha_2 s(b+aH)/\Delta_1$

$\Delta_1 = [a(\alpha_1^2-\alpha_2^2)- s]^2 + 4a^2\ \alpha_1^2\alpha_2^2$

$f_1 = -k[(k-\beta n^*)(\alpha_1^2+\alpha_2^2) - t]/\Delta_2$

$f_2 = k[(k-\beta n^*)(\alpha_1^2+\alpha_2^2) + t]/\Delta_2$

$\Delta_2 = [\{(k-\beta n^*)(\alpha_1^2-\alpha_2^2) - t\}^2 + 4(k-\beta n^*)^2\ \alpha_1^2\alpha_2^2]$

$$p_1 = \sinh \alpha_1/2 \cos \alpha_2/2$$

$$p_2 = \cosh \alpha_1/2 \sin \alpha_2/2$$

$$r_1 = \cosh \alpha_1/2 \cos \alpha_2/2$$

$$r_2 = \sinh \alpha_1/2 \sin \alpha_2/2$$

$$n_1 = a(e_1\alpha_1 - e_2\alpha_2) + b\alpha_1$$

$$n_2 = a(e_2\alpha_1 + e_1\alpha_2) + b\alpha_2 \qquad \text{(A-2.11)}$$

$$m_1 = b(e_1\alpha_1 - e_2\alpha_2) + d\alpha_1$$

$$m_2 = b(e_2\alpha_1 + e_1\alpha_2) + d\alpha_2$$

$$q_1 = tk[(k-\beta n^*)(\alpha_2^2 - \alpha_1^2) + t]/\Delta_2$$

$$q_2 = 2(k-\beta n^*)\,\alpha_1\alpha_2\, tk/\Delta_2$$

The stiffness matrix for beam 2 relating stress resultants and displacements at $x_2 = 1/2$, i.e.:

$$[\bar{N}] = [K^{(2)}][\bar{J}] \qquad \text{(A-2.12)}$$

is therefore given by:

$$[K^{(2)}] = [G][F]^{-1} \qquad \text{(A-2.13)}$$

<u>Stiffness Matrix for Beam 3</u>

Reversing the signs of stress resultants at $x_3 = 0$ (to conform to the sign convention at right hand end of beams 1 and 2) and introducing three unknown constants, the displacements and stresses are given by (A-2.8) where:

$$F = \begin{bmatrix} e_0 & e_1 & e_2 \\ 1 & 1 & 0 \\ f_0\lambda_1 & f_1\alpha_1 & f_2\alpha_2 \end{bmatrix} \qquad \text{(A-2.14)}$$

$$G = -\begin{bmatrix} n_0 & n_1 & n_2 \\ m_0 & m_1 & m_2 \\ q_0 & q_1 & q_2 \end{bmatrix} \qquad \text{(A-2.15)}$$

Where λ_1 is the negative root of λ_1^2, α_2 is positive and α_1 is negative. e_0, f_0, n_0, m_0 and q_0, e_1, e_2, f_1, f_2, n_1, n_2, m_1, m_2 are the same as in (A-2.11).

The stiffness matrix is given by:

$$[K^{(3)}] = [G][F]^{-1} \qquad \text{(A-2.16)}$$

Using the compatibility conditions :

$$\begin{aligned} U^{(1)} &= U^{(3)} + (H^{(3)}-H^{(1)})\ \psi^{(3)} \\ U^{(2)} &= U^{(3)} - (H^{(3)}-H^{(2)})\ \psi^{(3)} \\ \psi^{(1)} &= \psi^{(2)} = \psi^{(3)} \\ W^{(1)} &= W^{(2)} = W^{(3)} \end{aligned} \qquad \text{(A-2.17)}$$

and the equilibrium equations:

$$n_x^{(1)} + n_x^{(2)} + n_x^{(3)} = 0$$

$$m_x^{(1)} + m_x^{(2)} + m_x^{(3)} + n_x^{(1)}(H^{(3)}-H^{(1)}) \quad + n_x^{(2)}(H^{(2)}-H^{(3)}) \quad = 0$$

$$q_x^{'(1)} + q_x^{'(2)} + q_x^{'(3)} = 0 \qquad \text{(A-2.18)}$$

one can obtain:

$$[\bar{K}][U^{(3)}] = 0$$

where $\bar{K}$ is the global stiffness matrix. Critical values of n^* (or $N_x^{(1)}$) are determined by equating the global stiffness-matrix to zero.

APPENDIX A-3. ELASTIC WAVE PROPAGATION IN A LAMINATE

A typical laminate is shown in fig. 47. The laminate is referred to a fixed coordinate system x_1, x_2, x_3 while a typical lamina with fiber reinforcement angle θ is referred to x_1', x_2', x_3'.

Consider a transverse wave in x_3 direction characterized by the displacements:

$$u_1 = u_1(x_3, t)$$
$$u_2 = u_2(x_3, t) \qquad \text{(A-3.1)}$$
$$u_3 = u_3(x_3, t)$$

It follows that the nonvanishing strains are:

$$2\varepsilon_{13} = u_{1,3}$$
$$2\varepsilon_{23} = u_{2,3} \qquad \text{(A-3.2)}$$
$$\varepsilon_{33} = u_{3,3}$$

In order to establish the equations of motion associated with (A-3.1) it is necessary first to find the stresses associated with (A-3.2). For this purpose the stress-strain relation of a lamina is first written in its material system x_1', x_2', x_3'. Thus:

$$\sigma_{11}' = C_{1111}' \varepsilon_{11}' + C_{1122}' \varepsilon_{22}' + C_{1122}' \varepsilon_{33}'$$

$$\sigma_{22}' = C_{1122}' \varepsilon_{11}' + C_{2222}' \varepsilon_{22}' + C_{2233}' \varepsilon_{33}'$$

$$\sigma_{33}' = C_{11222}' \varepsilon_{11}' + C_{2233}' \varepsilon_{22}' + C_{3333}' \varepsilon_{33}'$$

$$\sigma'_{12} = 2C'_{1212}\,\varepsilon'_{12}$$

$$\sigma'_{23} = 2C'_{2323}\,\varepsilon'_{23} = (C'_{2222}-C'_{2233})\varepsilon'_{23} \qquad \text{(A-3.3)}$$

$$\sigma'_{13} = 2C'_{1212}\,\varepsilon'_{13}$$

The strains ε_{ij} in (A-3.2) and the strains ε'_{ij} in (A-3.3) are related by tensor transformation as defined by the relation between the x'_1, x'_2 and x_1, x_2 axes. It follows that:

$$\varepsilon'_{11} = \varepsilon'_{22} = \varepsilon'_{12} = 0$$

$$\varepsilon'_{33} = \varepsilon_{33}$$

$$\varepsilon'_{13} = \varepsilon_{13}\cos\theta - \varepsilon_{23}\sin\theta \qquad \text{(A-3.4)}$$

$$\varepsilon'_{23} = \varepsilon_{13}\sin\theta + \varepsilon_{23}\cos\theta$$

The surviving elastic moduli in (A-3.3) are thus :

$$C'_{1122} = \ell$$

$$C'_{2233} = k - G_T$$

$$C'_{3333} = k + G_T \qquad \text{(A-3.5)}$$

$$C'_{2323} = G_T$$

$$C'_{1212} = G_A$$

where k is transverse bulk modulus and G_T and G_A are transverse and axial shear moduli, respectively.

Further tensor transformation on stress yield relations of the θ rotated lamina with respect to the x_1, x_2 axes :

$$\sigma_{13} = 2C_{1313}\,\varepsilon_{13} + 2C_{1323}\,\varepsilon_{23}$$

$$\sigma_{23} = 2C_{1323}\,\varepsilon_{13} + 2C_{2323}\,\varepsilon_{23} \qquad \text{(A-3.6)}$$

$$\sigma_{33} = C_{3333}\,\varepsilon_{33}$$

where

$$C_{1313} = G_A \cos^2\theta + G_T \sin^2\theta$$

$$C_{2323} = G_A \sin^2\theta + G_T \cos^2\theta$$

$$C_{1323} = (G_A - G_T) \cos\theta \sin\theta \qquad \text{(A-3.7)}$$

$$C_{3333} = k + G_T$$

The only surviving parts of the equations of motion are :

$$\sigma_{13,3} = \rho\ddot{u}_1$$

$$\sigma_{23,3} = \rho\ddot{u}_2 \qquad \text{(A-3.8)}$$

$$\sigma_{33,3} = \rho\ddot{u}_3$$

where ρ is the density and a dot denotes time derivative.

Insertion of (A-3.2) into (A-3.6) and the resulting expressions into (A-3.8) yields the following wave equations:

$$C_{1313}\, u_{1,33} + C_{1323}\, u_{2,33} = \rho \ddot{u}_1 \qquad \text{(a)}$$

$$C_{1323}\, u_{1,33} + C_{2323}\, u_{2,33} = \rho \ddot{u}_2 \qquad \text{(b)} \qquad \text{(A-3.9)}$$

$$C_{3333}\, u_{3,33} = \rho \ddot{u}_3 \qquad \text{(c)}$$

In addition to these, displacements and tractions must be continuous at lamina interfaces. It is seen that the displacements (A-3.1) satisfy continuity. The traction components at an interface are σ_{13}, σ_{23} and σ_{33} and are given by (A-3.6).

In view of (A-3.7) it is seen that σ_{33} associated with the present solution is always continuous while σ_{13} and σ_{23} are not continuous for adjacent laminae with different θ. It is also seen that the discontinuity is entirely due to difference between the values of G_A and G_T. If this difference is small as is frequently found in practice, then the discontinuity may not seriously detract from the present simple treatment.

It is also seen that the discontinuity only concerns the shear wave equations (A-3.9;a,b). It may be argued that if a transverse pulse is transmitted through a small area of a laminate then u_2 and u_1 in the laminate plane may be disregarded, since the wave speed in transverse x_3 direction is so much larger, thus the shear waves having insufficient time to develop by the time the transverse pulse has been reflected in opposite direction.

As a consequence of all this, equation (A-3.9) is reliable. The wave speed associated with it is:

$$\rho c = \sqrt{\frac{C_{3333}}{\rho}} = \sqrt{\frac{k + G_T}{\rho}} \qquad \text{(A-3.10)}$$

DISTRIBUTION LIST

(1 copy)
Mr. D. Nesterok (Code 92713)
Naval Air Engineering Center
Lakehurst, NJ 08723

(1 Copy)
Mr. R. Deitrich (Code 92713)
Naval Air Engineering Center
Lakehurst, NJ 08723

(1 Copy)
Dr. W. J. Renton
Manager - Advanced Composites
Vought Corporation
Post Office Box 6144
Dallas, TX 75222

(1 Copy)
Dr. C. Sandy (Code 6370)
Naval Research Laboratory
Washington,DC 20375

(1 Copy)
Dr. R. Weimer (Code 6370)
Naval Research Laboratory
Washington, DC 20375

(12 Copies)
Administrator
Defense Documentation Center for Scientific and Technical Information (DDC)
Bldg. #5, Cameron Station
Alexandria, VA 22314

(1 Copy)
Mr. J. M. Warren
Naval Surface Weapons Center
White Oak
Silver Spring, MD 20910

(1 Copy)
Dr. Satish V. Kulkarni (Code L502)
Lawrence Livermore Laboratories
P. O. Box 808
Livermore, CA 94550

(3 Copies)
Dr. William R. Scott (Code 6063)
Naval Air Development Center
Warminster, PA 18974

(1 Copy)
Mr. Joseph Heyman
NASA/Langley MS499
Hampton, VA 23665

(1 Copy)
Dr. Michael J. Buckley (DARPA/MSO)
1400 Wilson Blvd.
Arlington, VA 22209

(1 Copy)
Mr. John Conroy (DRDAV-QP)
Army Aviation R&D Command
St. Louis, MO 63166

DISTRIBUTION LIST

(2 Copies)
Commander
Naval Air Systems Command (AIR-954)
Department of the Navy
Washington, DC 20361

(1 Copy)
Commander
Naval Air Systems Command (AIR-320)
Department of the Navy
Washington, DC 20361

(1 Copy)
Commander
Naval Air Systems Command (AIR-320A)
Department of the Navy
Washington, DC 20361

(1 Copy)
Commander
Naval Air Systems Command (AIR-340E)
Department of the Navy
Washington, DC 20361

(1 Copy)
Commander
Naval Air Systems Command (AIR-4114C)
Department of the Navy
Washington, DC 20361

(1 Copy)
Commander
Naval Air Systems Command (AIR-5163)
Department of the Navy
Washington, DC 20361

(1 Copy)
Commander
Naval Air Systems Command (AIR-5163B)
Department of the Navy
Washington, DC 20361

(1 Copy)
Commander
Naval Air Systems Command (AIR-5163D3)
Department of the Navy
Washington, DC 20361

(1 Copy)
Dr. Robert Crane (AFML/LLP)
Wright-Patterson Air Force Base
Air Force Materials Laboratory
Dayton, OH 45433

(1 Copy)
Mr. N. Tideswell (Code 2823)
David W. Taylor Naval Ship R&D Center
Annapolis, MD 21402

(1 Copy)
Mr. D. Polansky
Naval Surface Weapons Center
White Oak
Silver Spring, MD 20910

(1 Copy)
Mr. J. R. Gleim
Naval Ship Engineering Center
Washington, DC 20362

(1 Copy)
Mr. J. F. Goff
Naval Surface Weapons Center
White Oak
Silver Spring, MD 20910

(1 Copy)
Mr. G. V. Blessing
Naval Surface Weapons Center
White Oak
Silver Spring, MD 20910

(1 Copy)
Dr. M. I. Jacobson
Lockheed Missiles & Space Company, Inc.
Sunnyvale, CA 94088

(1 Copy)
Mr. S. D. Hart (Code 8435)
Naval Research Laboratory
Washington, DC 20375

(1 Copy)
Mr. I. Wolock (Code 8433)
Naval Research Laboratory
Washington, DC 20375

(1 Copy)
Mr. C. Anderson
Naval Surface Weapons Center
Dahlgren, VA 22448